

Reliability of Solder Interconnects under High Current Loading Conditions

Von der Fakultät Konstruktions-, Produktions- and Fahrzeugtechnik der Universität Stuttgart
zur Erlangung der Würde eines Doktors der Ingenieurwissenschaften (Dr.-Ing.)
genehmigte Abhandlung

Vorgelegt von

M.Sc. (hons) Jie Mei

aus Hubei, China

Hauptberichter:

Prof. Dr.-Ing. André Zimmermann

Mitberichter:

Prof. Dr. rer. nat. Dr. h. c. Siegfried Schmauder

Tag der mündlichen Prüfung:

23.07.2021

Institut für Mikrointegration der Universität Stuttgart

2021

Acknowledgements

This work is conducted under the cooperation of Robert Bosch GmbH in Schwieberdingen and the Institute for Micro Integration at University of Stuttgart. I would like to express my deepest gratitude to Prof. Dr. André Zimmermann, my dissertation advisor, for his persistent support and guidance on my work. I would also like to thank my supervisor at Bosch, Dr. Ralf Haug for his innumerable time and inspiring remarks on my work. Their immense knowledge and patience kept motivating me to overcome all the challenges and to fulfill the goal of the work. I would also like to extend my sincere thanks to Prof. Dr. Siegfried Schmauder for serving on my dissertation committee and sharing valuable remarks on the work.

Furthermore, I would like to thank many colleagues of Robert Bosch GmbH, Institute for Micro Integration and Hahn-Schickard. Without their support and all the valuable exchanges, the goal of the work would not have been reached. I would like to pay my special regards to Dr. Tobias Grözinger, Dr. Stefan Hinderberger and Dr. Olivier Lanier for their insightful inputs to my work and their contributions to the publications. I would also like to thank my head of department Dr. Marc Nikolussi, group leader Dr. Daniel Meyer, Dr. Harald Feufel and team leader Dr. Lauriane Lagarde for their support through each stage of my work.

I wish to express my sincere appreciation to the laboratory specialists and the colleagues in the department of AE/EAI for their kindness and assistance over the years. My PhD fellows have offered many technical discussions and exciting exchanges. For this, I am extremely grateful.

Last but not least, I am indebted to my family and friends for their support and encouragement through the ups and downs during the work.

Table of Contents

List of abbreviations.....	3
Glossary.....	5
Abstract	9
Zusammenfassung.....	11
1 Introduction	13
1.1 Problem statement.....	13
1.2 Backgrounds.....	14
1.2.1 Electronic assembly and surface mounting technology (SMT) process	14
1.2.2 Reliability issues regarding solder joints	15
1.3 Objective and scope of the work	21
2 Theoretical background.....	23
2.1 Solder material and material model	23
2.2 IMC layer	25
2.3 Failure mechanisms due to thermal load.....	28
2.4 Failure mechanisms due to current loads	31
2.5 Statistics	35
2.6 Lifetime model	36
3 Materials and experiments	41
3.1 Test components.....	41
3.1.1. Shunts.....	41
3.1.2. Components specification	42
3.2 Power cycling test	45
3.2.1 Test layout.....	45
3.2.2 Cable soldering.....	46
3.2.3 Test setup.....	46
3.2.4 Loading conditions.....	48
3.3 Self-heating of the shunts	50
3.3.1 Infrared (IR) thermography	50
3.3.2 Peltier effect	53
4 Failure analysis.....	54
4.1 Failure mode of shunt A (5 m Ω).....	55
4.1.1 Light microscope analysis	55
4.1.2 SEM analysis.....	57
4.2 Failure mode of shunt A (3 m Ω).....	59
4.2.1 Light microscope analysis	59
4.2.2 SEM analysis.....	61

4.2.3 CT analysis	62
4.3 Failure mode of shunt A* (3 mΩ)	66
4.3.1 Light microscope and SEM/ EDS analysis	66
4.3.2 Interfacial reaction.....	68
4.3.3 EBSD analysis.....	76
4.4 Failure mode of shunt B	81
4.5 Failure mode of shunt C	83
5 Simulation	87
5.1 Modeling and boundary conditions.....	87
5.1.1 Geometry modeling.....	87
5.1.2 Material assignment	91
5.1.3 Boundary conditions	92
5.2 Validation of the model.....	93
5.2.1 Mesh investigation	93
5.2.2 Validation with measurements	95
5.3 Evaluation of simulation results	99
5.3.1 Simulation of shunt A (5 mΩ).....	100
5.3.2 Simulation of shunt A (3 mΩ) and shunt A*	104
5.3.3 Simulation of shunt B and shunt C.....	110
6 Lifetime model	114
6.1 Lifetime data evaluation.....	114
6.2 Failure mode and damage parameter	117
6.3 Derivation of lifetime model	121
7 Summary and outlook	125
8 References	127
Appendix	137

List of abbreviations

3D	Three-dimensional
AF	Acceleration factor
AOI	Automatic optical inspection
APDL	Ansys parametric design language
AXI	Automatic X-ray inspection
BGA	Ball grid array
CDF	Cumulative distribution function
CT	Computer tomography
CTE	Coefficient of thermal expansion
DMA	Dynamic material analysis
EBSDB	Electron backscatter diffraction
ECU	Electronic control unit
EDS	Energy-dispersive X-ray spectroscopy
EM	Electromigration
FEM	Finite element method
GBS	Gain boundary sliding
HCF	High cycle fatigue
IDSA	Incremental damage superposition approach
IMC	Intermetallic compound
IPF	Inverse pole figure
LAGB	Large angel grain boundary
LCF	Low cycle fatigue
LDSA	Linear damage superposition approach
ML	Maximum likelihood
MR	Median rank
MTTF	Mean time to failure
OSP	Organic solderability preservative
PC	Power cycling
PCB	Printed circuit board

PCBA	Printed circuit board assembly
PSD	Power spectral density
QFN	Quad flat no leads package
ROI	Region of interest
RR	Rank regression
SAC	SnAgCu
SEM	Scanning electron microscopy
SM	Stressmigration
SMD	Surface mounted device
SMT	Surface mounting technology
S-N	Stress versus failure
SRCL	Synchrotron X-ray laminography
TC	Temperature cycling
TIM	Thermal interface material
TM	Thermomigration
TMA	Thermal mechanical analysis
TMF	Thermomechanical fatigue
UBM	Under bump metallization

Glossary

b	Basquin's exponent	-
c	Fatigue ductility exponent	-
	Constant for Engelmaier model	-
C_s	Solubility of Cu in solder	[atoms/m ³]
C_{Cu}	Cu concentration	[atoms/m ³]
C_{Cu/Cu_6Sn_5}	Cu concentration in IMC layer	[atoms/m ³]
$C_{Cu/Sn}$	Cu concentration in solder	[atoms/m ³]
C_i	Chaboche material parameters	[MPa]
D	Diffusion coefficient	[m ² /s]
D_0	Diffusion coefficient at infinite temperature	[m ² /s]
D_a	Diffusion coefficient along a-axis of β -Sn	[m ² /s]
D_c	Diffusion coefficient along c-axis of β -Sn	[m ² /s]
D_{Cu/Cu_6Sn_5}	Diffusion coefficient of Cu in IMC	[m ² /s]
$D_{Cu/Sn}$	Diffusion coefficient of Cu in solder	[m ² /s]
$\text{div}(\vec{J}_A)$	Divergence of material flux density of electromigration	[atoms/m ³ s]
$\text{div}(\vec{J}_S)$	Divergence of material flux density of stressmigration	[atoms/m ³ s]
$\text{div}(\vec{J}_{Th})$	Divergence of material flux density of thermomigration	[atoms/m ³ s]
$\text{div}(\vec{J}_{total})$	Total divergence of material flux density	[atoms/m ³ s]
E	Elastic modulus	[MPa]
e	Electron charge	-
E_a	Activation energy	[eV]
h_{IMC}	Thickness of IMC layer	[μ m]
Δh_{IMC}	Thickness growth of IMC layer	[μ m]
I	Current	[A]
\vec{j}	Current density	[A/cm ²]
\vec{J}_A	Material flux density of electromigration	[atoms/m ³]
\vec{J}_S	Material flux density of stressmigration	[atoms/m ³]
k	IMC growth rate constant	-
k_B	Boltzmann constant	[eV/K]

n	Time exponent for IMC growth	-
N	Atomic density	[atoms/m ³]
N_c	Number of cycles to failure due to creep	-
N_f	Number of cycles to failure	-
N_p	Number of cycles to failure due to plastic strain fatigue	-
P	Power	[W]
Q^*	Heat of transport	[eV]
$Q(t)$	Cumulative distribution function of the Weibull distribution	-
R	Gas constant	[J/mol·K]
	Resistance	[Ω]
	Evolved yield limit	[MPa]
t	Time	[s]
T	Local temperature	[K]
Z^*	Effective charge number	-
α	Back stress tensor	[MPa]
	Temperature coefficient of resistivity	[1/K]
α_1	Coefficient of thermal expansion	[1/K]
α_i	ith component of back stress tensor	[MPa]
$\dot{\alpha}_i$	Rate of back stress tensor	[MPa/s]
β	Shape parameter	-
γ	Location parameter	-
γ_i	Chaboche material parameters	-
ε	Total shear strain	[mm/mm]
ε_c	Creep strain	[mm/mm]
ε_e	Elastic strain	[mm/mm]
ε_p	Plastic strain	[mm/mm]
ε'_f	fatigue ductility coefficient	-
$\dot{\varepsilon}^{pl}$	Plastic strain rate	[MPa/s]
ε^{pl}	Plastic strain in the uniaxial direction	[MPa]
$\varepsilon_{acc_VWA}^{pl}$	Volume-averaged accumulated plastic strain	[MPa]

$\varepsilon_{\text{eqv}}^{\text{pl}}$	Accumulated equivalent plastic strain	[MPa]
$\varepsilon_{\text{L}}^{\text{pl}}$	Strain limit of the hysteresis loop	[MPa]
η	Scale parameter	-
θ	Angle between the current direction and c-axis of β -Sn	[deg]
ν	Poisson ratio	-
ρ	Resistivity at local temperature	[Ω/m]
ρ_0	Resistivity at reference temperature	[Ω/m]
σ	Stress tensor	[MPa]
$\sigma_{\text{I}}, \sigma_{\text{II}}, \sigma_{\text{III}}$	Principal stress	[MPa]
σ'_{f}	fatigue strength coefficient	-
σ_{H}	Hydrostatic stress	[MPa]
σ_0	Initial yield stress	[MPa]
σ_{x}	Uniaxial yield stress	[MPa]
σ^{dev}	Deviatoric stress	[MPa]
Ω	Atomic volume	[m^3/mol]

Abstract

Highly integrated electronic devices are required to enable the trend of personalization, automation, connection and electrification in the automotive industry. The increasing demands for higher performance, lower cost and smaller size of the automotive packages have brought the reliability issues to the forefront.

This work aims to investigate the reliability of electronic components subjected to high current loads via experimental and numerical analysis. The study is focusing on the failure analysis of interconnection technology, since it has become one of the weakest links in the assembly with the trend of miniaturization. Power cycling tests with various loading conditions have been performed on the assemblies of shunt components. The resistance is electrically monitored during the test and failure is reported when 50% resistance increment is detected. Lifetime data are collected and further evaluated statistically with 3-parameter Weibull distribution. The self-heating behavior of the components is studied with thermography measurements. The failure mechanism of the SnAgCu (SAC) solder joints under active power cycling load is investigated via light microscopy, scanning electron microscopy (SEM), energy-dispersive X-ray spectroscopy (EDS), computer tomography (CT) and electron backscatter diffraction (EBSD) techniques. The microstructural evolution of the solder material under current stressing is analyzed via the mentioned material characterization techniques. Failure mechanisms such as thermo-mechanical fatigue (TMF) and electromigration (EM) are discussed in details based on the experimental findings. To assess the response of the assembly subjected to current stressing, finite element method (FEM) simulations are performed to evaluate the multiphysics thermal-electrical-mechanical fields in the package. The accumulated plastic strain and divergence of material flux density are calculated. The simulative damage parameters are utilized to characterize the failure modes observed from the tests.

A lifetime model is derived on the basis of lifetime data obtained from tests and numerical results. This provides a physics-of-failure based understanding of the performance of solder interconnects under field-like active loads and serves to assess the reliability of the package design under use condition.

Zusammenfassung

Hochintegrierte elektronische Geräte sind erforderlich, um den Trend der Personalisierung, Automatisierung, Vernetzung and Elektrifizierung in der Automobilindustrie zu ermöglichen. Die steigenden Anforderungen an höhere Leistung, niedrigere Kosten and geringere Baugröße der Automobilgehäuse haben die Themen in Bezug auf die Zuverlässigkeit in den Vordergrund gerückt.

Ziel dieser Arbeit ist es, die Zuverlässigkeit von elektronischen Bauteilen, die hohen Strombelastungen ausgesetzt sind, durch experimentelle and numerische Analysen zu untersuchen. Die Arbeit konzentriert sich auf die Fehleranalyse der Verbindungstechnik, da diese mit dem Trend zur Miniaturisierung zu einem der schwächsten Elemente geworden ist. An verschiedenen Shunt-Komponenten wurden Power-Cycling-Tests mit unterschiedlichen Belastungsbedingungen durchgeführt. Der Widerstand der Bauelemente wird während des Tests elektrisch gemessen, and der Ausfall wird registriert, wenn eine Widerstandserhöhung von 50% festgestellt wird. Die Lebensdauerdaten werden gesammelt and mit der 3-Parameter-Weibull-Verteilung weiter statistisch ausgewertet. Das Eigenerwärmungsverhalten der Komponenten wird durch Thermografiemessung untersucht. Der Fehlermechanismus der SnAgCu-Lötstelle unter aktiver Belastung durch Leistungszyklen wird mit Hilfe von Lichtmikroskopie, Rasterelektronenmikroskopie, energiedispersiver Röntgenspektroskopie, Computertomographie and Elektronenrückstreubeugung untersucht. Der mikrostrukturelle Alterungsvorgang des Lots unter Strombeanspruchung wird mit den genannten Materialcharakterisierungstechniken analysiert. Fehlermechanismen wie thermomechanische Ermüdung and Elektromigration werden basierend auf den experimentellen Ergebnissen detailliert diskutiert. Um die Reaktion der Bauelemente unter Strombeanspruchung zu bewerten, werden Finite-Elemente-Methode-Simulationen durchgeführt, um die thermisch-elektrisch-mechanischen Multiphysik-Belastungen im Packaging zu bewerten. Die akkumulierte plastische Dehnung and die Divergenz der Materialflussdichte werden berechnet. Die simulierten Schädigungsparameter werden eingesetzt, um die beobachteten Ausfallmodi aus den Versuchen zu charakterisieren.

Das Lebensdauermodell wird auf der Grundlage der experimentellen Lebensdauerdaten and der numerischen Ergebnisse abgeleitet. Dies ermöglicht ein auf der Fehlerphysik basierendes Verständnis der Performance des Lotes unter aktiver Last and dient einer Zuverlässigkeitsbewertung des Produkts unter Betriebsbedingungen.

1 Introduction

This chapter gives an introduction into interconnection technology and reviews the common reliability issues regarding interconnect technology in automotive use conditions. The goal of this work is defined and clarified in this chapter.

1.1 Problem statement

The automotive industry is experiencing a magnificent transformation towards personalization, automation, connection and electrification. This requires highly integrated electronic devices, which serve to sense, compute and actuate certain functions to assure the safety and improve the driving experience for drivers and passengers. Fig. 1.1 [1] gives a glimpse of overall applications of automotive electronics. The functions of the automotive electronics have evolved from fundamental controlling of the engine to providing new features, enabling excellent driving experience for people.

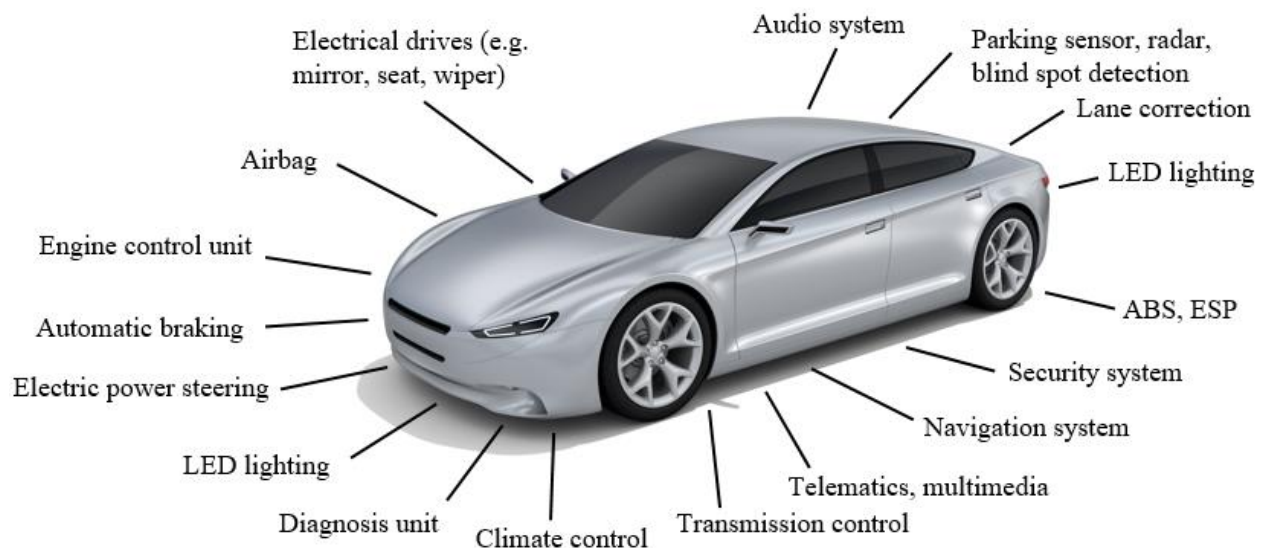


Fig. 1.1: Overview of the automotive electronics [1]

The transformation also gives rise to new challenges, especially the reliability risks accompanying the trend of miniaturization and cost reduction. Electronic systems often operate under harsh use conditions such as high temperature, large temperature fluctuation, various humidity levels and different mechanical loads. Thermal, electrical and mechanical loads are exerted on the electronic devices individually or mostly in combination. Electronic devices should withstand the severe loading conditions and fulfill their functions during the expected lifetime. To achieve that, it is of great significance to understand the failure mechanisms of the electronic systems, to assess the reliability of the product and to mitigate the degradation in order to meet the reliability

requirements. Solder interconnects, which serve as mechanical and electrical connections between the package elements, have become one of the weakest links with the reduction of package size.

1.2 Backgrounds

1.2.1 Electronic assembly and surface mounting technology (SMT) process

Fig. 1.2 presents a typical configuration of automotive electronic control units (ECU), which mainly consists of printed circuit boards (PCBs), electronic components, heat sink, thermal interface material (TIM) and housing. The electronic components are assembled on the PCB which is known as printed circuit board assembly (PCBA). PCBs can be single-sided with one copper layer on the rigid insulating layer, doubled-sided with copper layers on both sides of the rigid insulating layer or multi-layer. The multi-layer PCB is laminated with outer-layer copper foil, inner-layer copper tracks and non-conductive substrate layers in between. The conductive pathways of PCBs serve to connect the electronic components electrically.



Fig. 1.2: Schematic configuration of electric power steering unit [2]

The main interconnect technologies implemented for PCB-based ECU production are SMT process, selective soldering and press-fit technology. The SMT process includes solder paste printing, solder paste inspection, pick and place, reflow soldering and automatic inspection. Fig. 1.3 illuminates concisely the main steps of solder paste printing. A stencil with openings is adjusted to match the copper pad on the PCB. The solder paste is deposited on the stencil and is squeezed

into the openings of the stencil by the force of a squeegee. The openings of the stencil are filled with solder paste and the stencil is afterwards removed, leaving the solder paste on the copper pad. In this work, SnAgCu (SAC) series alloys are investigated. The solder paste consists essentially of SAC alloy powder, resin, activators, solvents, thixotropic agents and some special additives.

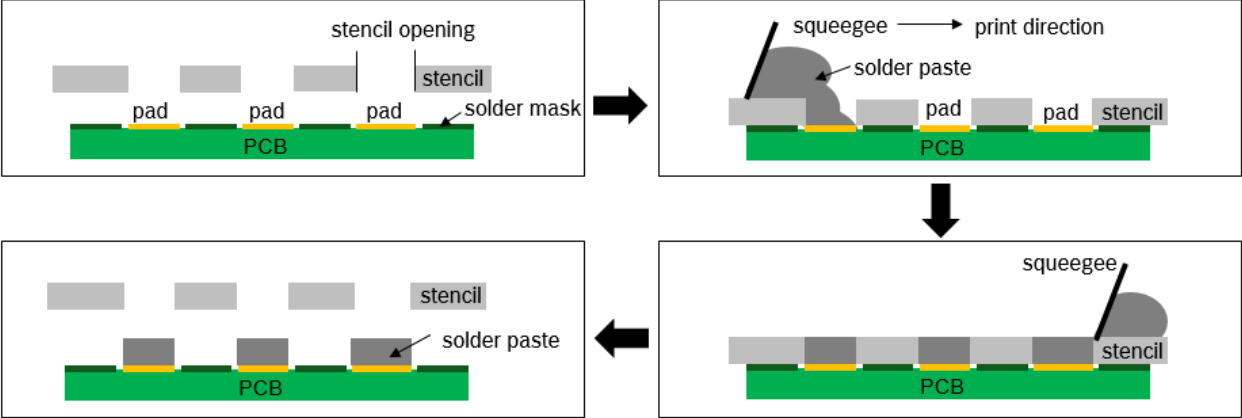


Fig. 1.3: Schematic diagram of solder paste printing

After the solder paste printing, the components are picked and placed on the solder paste and the assembly is transported into a reflow oven, where the solder paste melts under the reflow temperature and the fugitive constituents of the solder flux vaporize. After solidification, the solder joint is formed connecting the component and PCB and the quality is further examined with automatic optical inspection (AOI) or automatic X-ray inspection (AXI).

1.2.2 Reliability issues regarding solder joints

The defects occurring during the assembly process are considered as quality issues. After the manufacturing and meeting the quality expectations, the durability of the product to perform its required function under stated use conditions during the expected operating life is defined as the reliability of the product, which can be described by the "bathtub curve" in Fig. 1.4 [3]. The region of "infant mortality" characterizes the early failures mainly owing to quality issues. Random failures take place during the period of "normal life", which shows low and constant failure rate. The "wear-out" period starts eventually with increasing failure rate. The failure of an individual product can occur at each period. To evaluate the variation of the performance of the individual, statistical analysis is required, which will be further discussed in the next chapter. This section further reviews the loading conditions, which degrade the reliability of automotive electronics and cause the failure in the "wear-out" period.

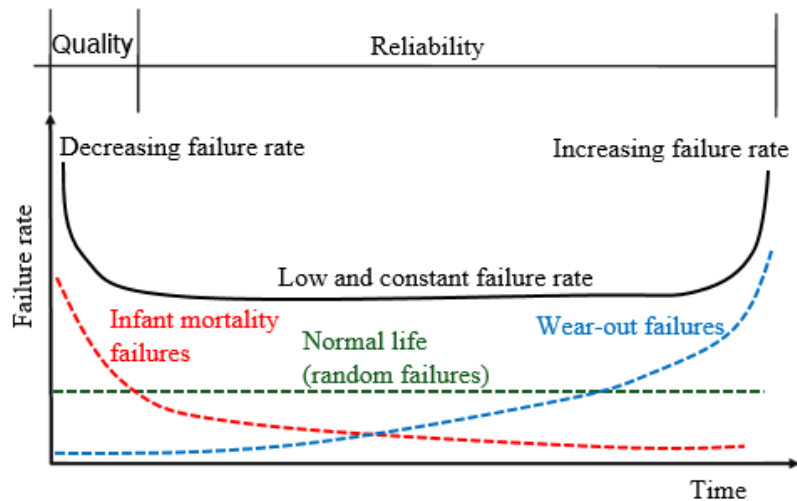


Fig. 1.4: Bathtub curve (lifetime of a product) [3]

1) External temperature fluctuation

During service conditions, the automotive electronic systems are subjected to external temperature fluctuation, which mainly results from the climatic weather change or power on-off cycles of the neighboring components. Fig. 1.5 illustrates the simplified schematic of the relative shrinkage and expansion of the assembly under thermal fluctuation. When the assembly is subjected to temperature cycling, the solder interconnect undergoes cyclic thermo-mechanical stress due to the mismatch of the coefficient of thermal expansion (CTE) of the joint elements, which degrades the solder joints during service. The failure mechanism induced by the cyclic loading is fatigue.

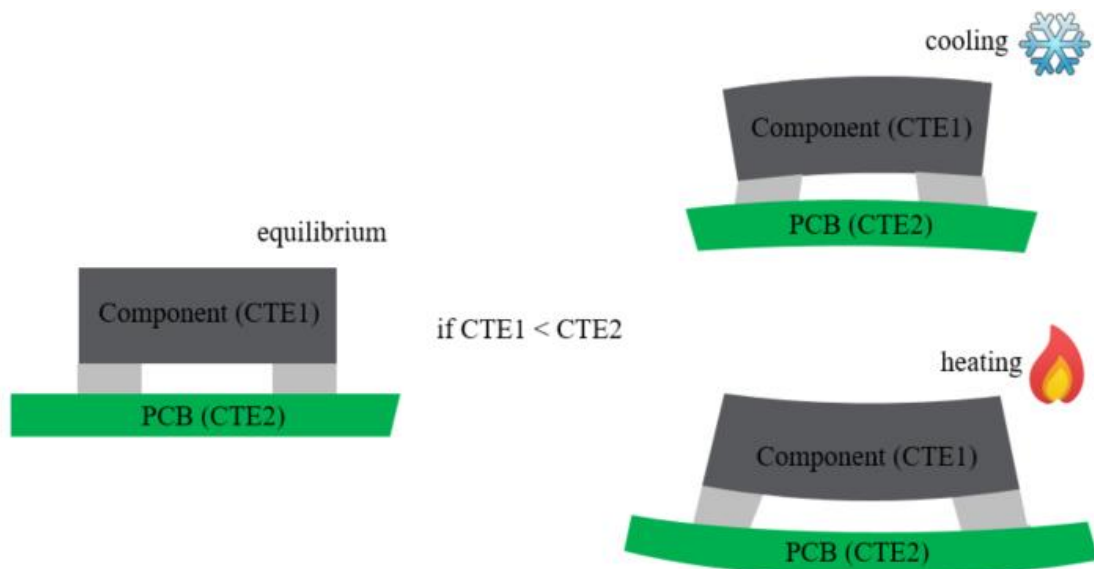


Fig. 1.5: Simplified schematic of the assembly at different temperatures

The thermomechanical fatigue (TMF) behavior of lead-free solder joints has been widely investigated [4-12]. During the temperature cycling (TC) test, the as-solidified Sn-rich phase in

the solder joint transforms into smaller grains with equiaxed structures by recrystallization. The newly formed grain boundaries enable grain boundary sliding (BGS) and diffusion under thermomechanical loadings, which provides favorable paths for fatigue cracks to initiate and propagate, eventually resulting in intergranular fracture [13-17].

In addition to the fatigue failure in bulk solder joints, brittle fracture is also observed at the interface between the solder joint and intermetallic compound (IMC) [18-20]. After the soldering process, the IMC layer is formed between the interface of the solder with component and with PCB, serving as bonding material. The thickness of IMC layers increases during TC loading and the thick and brittle IMC layers reduce the fatigue life [21-22]. Fig. 1.6 [23] describes the hypothesis of the correlation of failure modes and the applied strain rate. When the electronic assembly is subjected to loading conditions with high strain rate, the strength of IMC is weaker than that of the solder. Hence, IMC cracks incline to occur. The shift of failure mode in a quad flat no leads package (QFN) is displayed in Fig. 1.6.

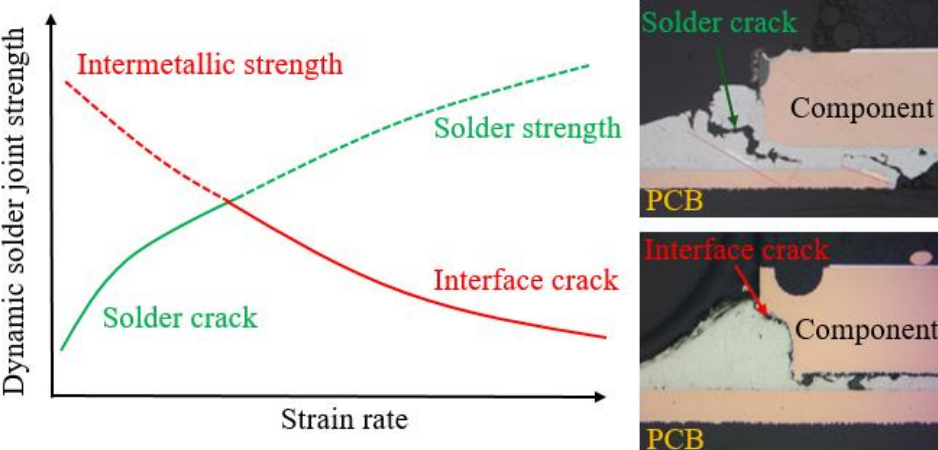


Fig. 1.6: Correlation between strain rate and failure modes [23]

2) Mechanical load

Mechanical loads like drop, vibration and bending also degrade the electronic systems, which mainly occur due to mishandling, mounting of the assembly or service conditions. The large and heavy components like electrolytic capacitors are often susceptible to drop and vibration loads. The sensitiveness of components regarding bending loads normally increases with larger area size of the components.

The drop impact loading exerts high strain rate on the solder interconnects. The strain-rate hardening increases the stress locally above the fracture strength of IMC and provokes cracking at the interface of solder/IMC or between the solder joint and PCB [24-28]. The elasto-plastic behavior of SAC solder subjected to high strain-rate loading conditions has been characterized in

some studies and models are used to describe the drop performance of SAC solder joints [29-31]. The SAC solder alloys exhibit poorer performance in drop tests than SnPb alloys as a result of their higher compliance and longer stress relaxation time after deformation [32]. Some doping elements have been studied to improve the drop test performance of SAC solder alloys [33-34]. Darbandi [32] investigated the effect of cooling rate on the shock performance of SAC solder and concluded that rapidly cooled samples absorb the energy better under shock conditions owing to stress relaxation during the recrystallization process.

Vibration loads could occur during manufacturing process, transportation or operation. The vibration-induced failure in SAC solder joints is attributed to high cycle fatigue (HCF) and the failure modes vary with different vibration excitations levels. With the increase of vibration intensity, the failure modes convert from ductile fracture to brittle fracture. The failure location in ball grid array (BGA) packages changes from the solder bump at the PCB side to the solder ball neck. Liu [35] detected IMC cracking in BGA packages when the acceleration power spectral density (PSD) amplitudes are increased to $160(\text{m/s}^2)^2/\text{Hz}$, which is comparable to drop impact loading. Yu [36] and Chen [37] have conducted vibration tests and simulation on BGA packages under different vibration excitation conditions. The stress induced by the vibration load is calculated by simulation and stress versus failure cycles (S–N) is derived for lifetime prediction. The same methodology is applied to derive the S–N curve for surface mounted device (SMD) capacitors under vibration loads [38].

Electronic assemblies are often encapsulated in a metal housing via fixation of screws to avoid contamination and moisture from the environment, as shown in Fig. 1.2. This process might introduce warpage in the PCBs, which highly deteriorates the reliability of the PCBAs during their service life. Three-point (3P) [39-40] and four-point (4P) [41-43] cyclic bending tests in combination with TC tests are normally performed to evaluate the electronic package's endurance against the bending load. 3P bending tests provide various displacement loads during the test, while 4P bending tests offer statistical lifetime data under certain bending load. Fig. 1.7 portrays the bending moment exerted on the assembly in a 3P and in a 4P bending test. Inelastic energy dissipation [41-42, 44] and equivalent plastic strain [45] are often selected as damage parameters to assess the fatigue lifetime of solder joints under cyclic bending loads.

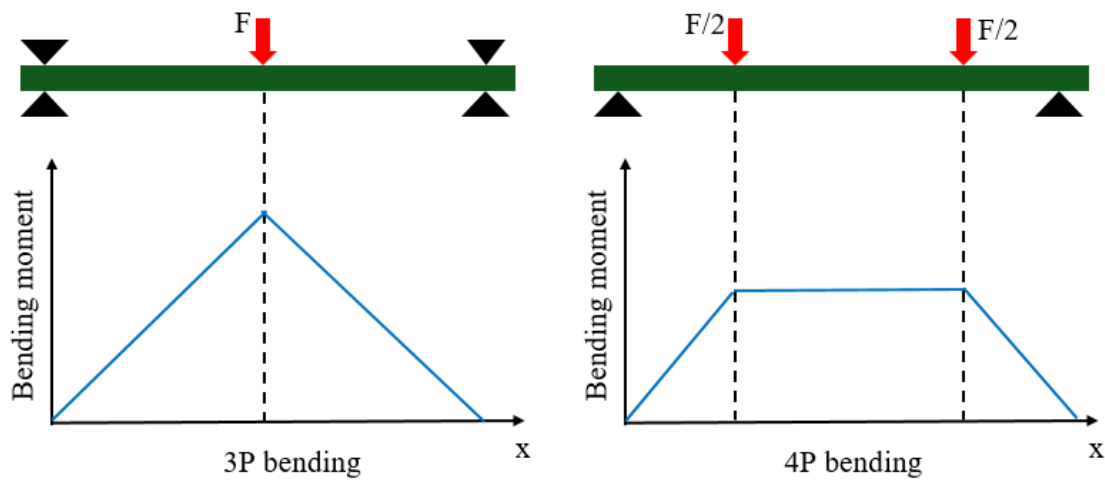


Fig. 1.7: Bending moment diagrams in a 3P- and in a 4P-bending test [46]

3) Current loads

Current loads introduce internal thermal fluctuation into the assembly due to the Joule heating of the component. Therefore, the solder interconnect undergoes thermo-mechanical stress which is similar to passive temperature cycling. Apart from the CTE mismatch of the joint components and PCBs, the self-heating of the components leads to thermal gradients in the assembly, while the temperature is distributed uniformly under passive TC test. When the CTE of the component is smaller than that of the PCB, the assembly exhibits concave warpage under elevated temperature, as displayed in Fig. 1.5. When active current load is applied to the assembly, the component is exposed to a higher temperature than the PCB due to local self-heating, which could compensate its smaller CTE compared to the PCB. Consequently, solder joints might encounter smaller thermo-mechanical stress and exhibit higher reliability under active power cycling (PC) tests than passive TC tests, when the temperature range of both tests are similar. Nowotnick [47] conducted PC tests on chip resistors and detected a slight decrease in the shear forces of solder joints after 4000 cycles, while large degradation in solder joints is detected for TC tests. This can be explained by the non-uniform temperature distribution under active load and the expansions of components and PCBs are almost repeating. Therefore, passive TC tests provide a conservative evaluation of the capability of solder joints exposed to thermo-mechanical loads.

The following question comes to the forefront: is the knowledge of the behavior of solder joints under passive TC tests sufficient to interpret the behavior of solder materials under active loading? The failure modes in both TC and PC tests are induced by recrystallization-assisted crack nucleation and propagation [27], only considering the thermal fluctuation. However, when the electronic assembly is exposed to high current density, electromigration could take place and result in early degradation of the solder joints. The main failure modes induced by electromigration are

i) void formation and ii) consumption of the under bump metallization (UBM). Electromigration also enhances the IMC growth at anode side and impedes the IMC growth at cathode side, which might weaken the capability of solder joints under thermo-mechanical load. Consequently, the knowledge of the behavior of solder joints under TC loads needs to be extended to understand the performance of the electronic devices under active current loads.

4) Combined loading

In the field conditions, the electronic devices often operate under complex loading conditions where the above loads are combined. An electronic assembly which exhibits high TC reliability might fail relatively early in vibration loads. Therefore, it is essential to understand the degradation mechanism of each single load and how they interact, which can ultimately enlighten companies to improve the desired performance of their products.

Shnawah [25] summarized the reliability of SAC solder joints with different Ag contents regarding the TC reliability and drop performance. It is noted that low Ag content and more primary Sn phases can improve the drop impact performance of the solder. However, high Ag content gives rise to more Ag_3Sn and single crystal-like microstructures, which enhances the TC reliability. The IMC layer grows when the assembly is exposed to TC load, defects such as Kirkendall voids can take place as a result of interdiffusion, which highly weakens the bonding between solder and PCB board and significantly decreases the drop lifetimes [48].

Concurrent vibration load and temperature cycling often arises in automotive applications. The reliability of SAC solder subjected to combined vibration and TC loads has been investigated and some superposition approaches have been proposed to evaluate the impact from vibration damage and from TC damage. The linear damage superposition approach (LDSA) assumes negligible interaction between the vibration and TC loads and the damage introduced by each load is determined individually [49-50], while the incremental damage superposition approach (IDSA) considers the temperature imposed load state on vibration damage [51-52]. Qi [53] observes that the LDSA over-predicts the lifetime of plastic ball grid array (PBGA) assemblies and the IDSA approach represents better the test data. Eckert [54] detected that the crack path in combined loading is partly transgranular and partly intergranular, which differs from the crack path observed in pure TC tests.

In the field, electronic devices often work under user-controlled on and off cycles and environmental temperature change. This results in complex temperature fluctuation in the package, which cannot be depicted by TC tests with simple temperature profiles. Many studies only consider the thermo-mechanical load induced by the external and internal thermal fluctuation when the

assembly is subjected to concurrent TC and PC load. Chai [55-56] proposed to segment the complex thermal fluctuation into multiple simple temperature cycles and superpose the damage by applying Miner's rule. A nonlinear accumulation rule is introduced to determine the solder joint life under combined load, based on the fatigue crack propagation theory and the solder joint crack growth model [57]. The coupled loading highly reduces the fatigue lifetime of solder interconnects compared to pure TC tests [58]. However, electromigration cannot be neglected when the assembly is exposed to high current density. EM-induced void formation, consumption of UBM and polarity effect of the IMC growth highly degrade the TMF behavior of the solder joint and significantly reduce the lifetime. The studies [59-63] provide a basis to understand the coupling effect of the failure mechanisms of electromigration and thermo-mechanical fatigue. However, there is a lack of quantitative analysis of the contributions of both mechanisms and the investigations are mainly limited to lab test samples or lab test conditions.

1.3 Objective and scope of the work

This work is focusing on the field-relevant failure modes of solder interconnects subjected to active current load. With the rising market for hybrid or electric vehicles, the reliability issues regarding high-density currents are of great significance. When the vehicle undergoes user-controlled on and off cycles, the electronic systems also experience power switching cycles. Fig. 1.8 presents an exemplary current profile for the automotive electronic systems in the field. The representative electronic assembly works under high current pulses. The pulse duration varies from few milliseconds to seconds. Apart from the internal self-heating of the electronics, the assembly is also exposed to high environmental temperature depending on the mounting location and the influence of neighboring components. Therefore, high current pulses and high environmental temperature are chosen to be test conditions in this work.

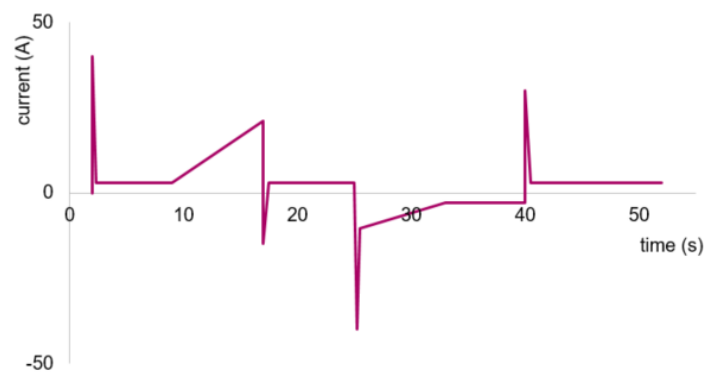


Fig. 1.8: Exemplary load profile for automotive electronic systems

Shunt components are selected for the investigation. Shunts exhibit relatively high reliability among all the components and no failure has been reported under pure TC tests. This is due to the small CTE mismatch of the joint elements, where the CTE of shunts and of the PCBs are 16.5 ppm/K and 15 ppm/K respectively. However, failure in solder joints has been detected when shunts operate under active PC testing [64]. Therefore, the knowledge transfer from TC tests to active load is not sufficient and further study is required to understand and assess the failure mechanism of solder joints subjected to current stressing conditions. Besides, the available studies regarding active load are mainly restrained to specimens designed for lab tests or individual failure mechanisms. This work aims to investigate the component in ECU products under field-like test conditions and to describe the complex failure mechanisms, where electrical and thermal loads are both contributing to the failure of solder joints.

In summary, the targets of the work are:

- 1) develop a methodology to investigate the reliability of solder joints under active load
- 2) design and perform PC tests on shunts and reproduce field-relevant failure modes
- 3) understand the failure mechanism of solder joints subjected to field-like current load
- 4) simulate the multi-physics field of the assembly and describe the failure mode
- 5) derive a lifetime model on the basis of the experimental and numerical results
- 6) propose a procedure for reliability assessment in the future design

2 Theoretical background

This chapter discusses the properties of SAC solder materials and the failure mechanisms related to active current loads. The statistical theory is concisely interpreted and the published lifetime models are reviewed.

2.1 Solder material and material model

Lead-based solder materials are prohibited due to their harm for health and environment. The SAC solder alloys are the most popular alternatives, which have been widely used in automotive industry. The most popular SAC solder series alloys are shown in Figure. 2.1 [25], which consist of 3.0–4.0% of Ag and 0.5–1.0% of Cu. The solder material investigated in this work is SAC 405, which falls into this category. The melting point of the near eutectic SAC solder is 217°C, which leads to high homologous temperature even at room temperature. Homologous temperature equals to the ratio of temperature of the material and its melting point temperature in Kelvin. When the homologous temperature is greater than 0.4, solder materials are also prone to creep [64] and microstructural coarsening [23, 65-66].

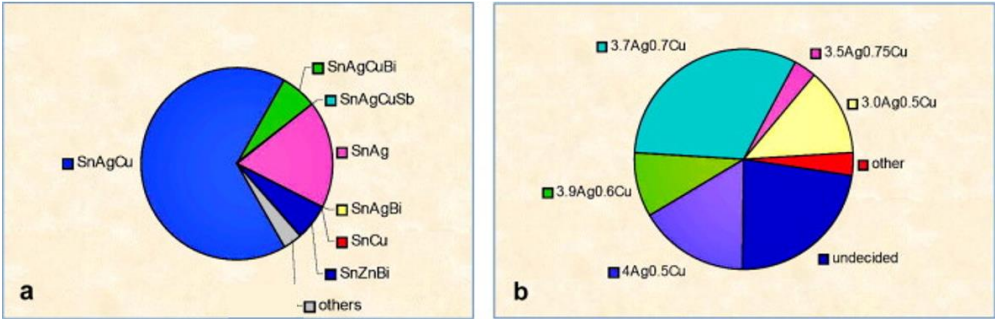


Figure 2.1: Different types of solder alloys [25]

Solder joints deform under cyclic thermo-mechanical loads and plastic deformation occurs when material deforms up to yield. The cyclic plasticity of materials can be described by the hardening models illustrated in Fig. 2.2.

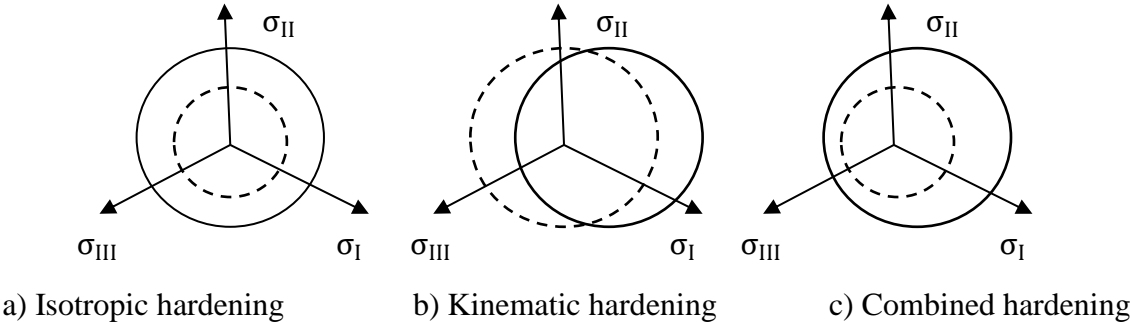


Fig. 2.2: Yield surfaces evolution according to hardening rules [67]

The yield surface is expressed by the three-dimensional principal stress σ_I , σ_{II} , σ_{III} . The dotted line represents the initial yield surface and the solid line describes the evolved yield surface. Isotropic hardening models depicts that the yield strength in tension and compression develops equally with increasing plastic strain [68]. In kinematic hardening model, yield surface shifts as a rigid body. The evolved center of kinetic hardening yield surface is defined with back stress tensor, which describes Bauschinger effect. The combined hardening model merges the characteristic of both isotropic and kinetic hardening models. The general expression of yield surface is defined as:

$$f(\sigma - \alpha) - R=0 \quad (2.1)$$

Where σ is the stress tensor, α is the back stress tensor and R is the evolved yield limit. When von Mises' yield criterion is utilized, the yield surface can be expressed as:

$$\sqrt{\left(\frac{3}{2}(\sigma^{\text{dev}} - \alpha):(\sigma^{\text{dev}} - \alpha)\right)} - R = 0 \quad (2.2)$$

where σ^{dev} represents deviatoric stress.

In the hardening models mentioned above, the back stress tensor develops linearly with plastic strain, which cannot capture the cyclic plasticity of material thoroughly. A fading memory term for back stress tensor calculation is introduced by Armstrong and Frederick [69]. Later Chaboche [70-71] proposed the nonlinear kinematic hardening model by superimposition of back stress terms in form of the Armstrong-Frederick rule, which is expressed as Equation (2.3)-(2.4) [72].

$$\alpha = \sum_{i=1}^n \alpha_i \quad (2.3)$$

$$\dot{\alpha}_i = \frac{2}{3} C_i \dot{\varepsilon}^{\text{pl}} - \gamma_i \varepsilon_{\text{eqv}}^{\text{pl}} \alpha_i \quad (2.4)$$

where n is the number of back stress components, α_i is the i th component of back stress tensor, $\dot{\alpha}_i$ is the rate of the back stress tensor, $\dot{\varepsilon}^{\text{pl}}$ the is plastic strain rate, $\varepsilon_{\text{eqv}}^{\text{pl}}$ is the accumulated equivalent plastic strain, C_i and γ_i are material parameters. At least three components are required to model ratcheting accurately. A third-order Chaboche model is given in (2.5) [72].

$$\frac{C_1}{\gamma_1} + \frac{C_2}{\gamma_2} + \sigma_0 = \sigma_x - \frac{C_3}{2} \left[\varepsilon_x^{\text{pl}} - \left(-\varepsilon_L^{\text{pl}} \right) \right] \quad (2.5)$$

where $\varepsilon_x^{\text{pl}}$ is plastic strain in the uniaxial direction, $\varepsilon_L^{\text{pl}}$ is strain limit of the hysteresis loop, σ_x is uniaxial yield stress, σ_0 is initial yield stress. C_1 , C_2 , C_3 , γ_1 , γ_2 , γ_3 are material parameters. Métais and his colleagues [74-77] conducted tension-compression tests on SAC solder specimens at different strain rates and under different temperatures. Based on his results, the parameters for the

third-order Chaboche model are derived and calibrated to characterize the cyclic plasticity of SAC solder.

2.2 IMC layer

Intermetallic compounds are formed by interfacial reaction between the component metallization and Sn-based solder, which is desirable to achieve a good metallurgical bond [19, 78]. The binary phase diagrams in Fig. 2.3 [25, 79] provide hints on the formation of possible intermetallic compounds in SAC alloys, which are Ag_3Sn , Cu_6Sn_5 , Cu_3Sn . When the plating of a component consists of Ni, Ni diffuses into solder and replaces the Cu site in Cu_6Sn_5 , forming IMC of $(\text{Cu}, \text{Ni})_6\text{Sn}_5$ and hindering the formation of Cu_3Sn . Fig. 2.4 [80] represents the morphology of Cu_6Sn_5 and $(\text{Cu}, \text{Ni})_6\text{Sn}_5$ after 1-time and 4-time reflows. The IMC of Cu_6Sn_5 yields scallop-shaped morphology [81], while the $(\text{Cu}, \text{Ni})_6\text{Sn}_5$ IMC exhibits a planarized interface with smoother surface than Cu_6Sn_5 . The roughness of the IMC layer increases with more reflow times, which highly affects the strength of the solder joints [80, 82-83].

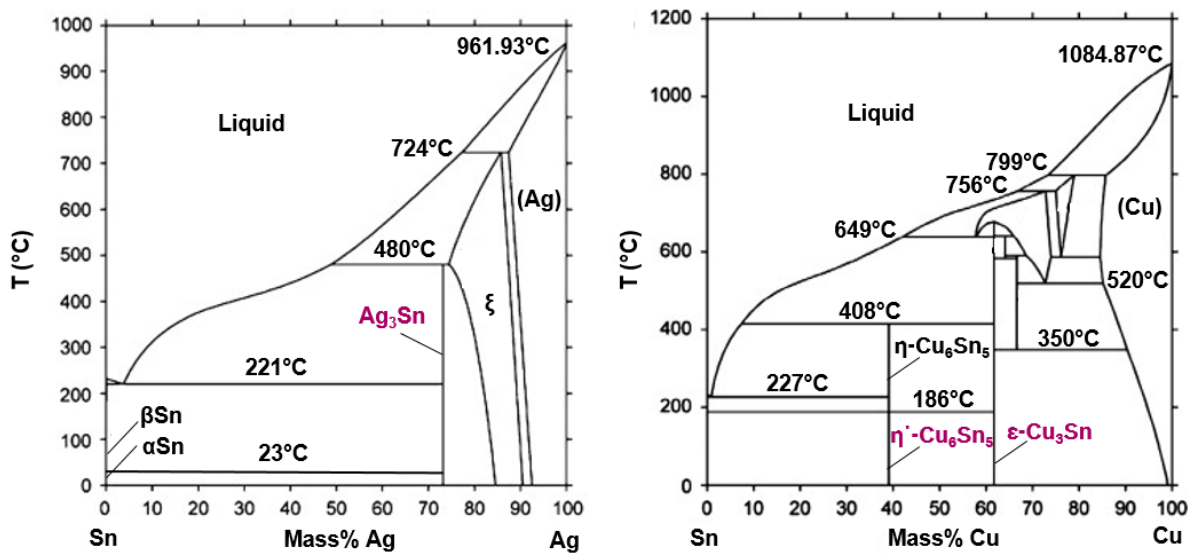


Fig. 2.3: Binary phase diagram of Sn–Ag and of Sn–Cu [25]

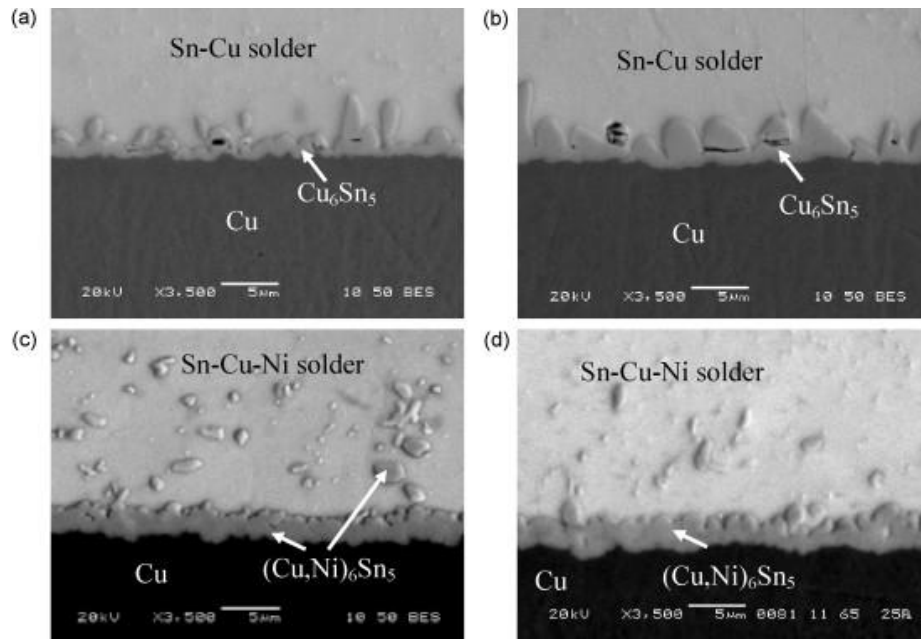


Fig. 2.4: IMC layer subjected to 1 and 4-time reflowed BGA samples [80]

(a) Cu_6Sn_5 in a 1-reflowed sample, (b) Cu_6Sn_5 in a 4-reflowed sample, (c) $(\text{Cu},\text{Ni})_6\text{Sn}_5$ in a 1-reflowed sample, and (d) $(\text{Cu},\text{Ni})_6\text{Sn}_5$ in a 4-reflowed sample

Tsukamoto [80] has performed nanoindentation tests on the IMC layer with and without Ni addition and the mechanical properties are summarized in Table 2.1. The hardness of $(\text{Cu}, \text{Ni})_6\text{Sn}_5$ shows scattering data which are grouped into higher and lower categories, which could be resulted from the crystallographic characteristics of the IMCs. The Young's modulus of $(\text{Cu}, \text{Ni})_6\text{Sn}_5$ is higher than that of Cu_6Sn_5 for all the reflowed samples. And both elastic modulus and hardness of the IMCs show little change with respect to reflow times [80].

Table 2.1: Average values of elastic modulus and hardness of IMC layer [80]

	1 Reflow		2 Reflow		4 Reflow	
	Cu_6Sn_5	$(\text{Cu},\text{Ni})_6\text{Sn}_5$	Cu_6Sn_5	$(\text{Cu},\text{Ni})_6\text{Sn}_5$	Cu_6Sn_5	$(\text{Cu},\text{Ni})_6\text{Sn}_5$
Elastic modulus (GPa)	124.16	133.80	126.87	134.40	129.38	131.58
Hardness (GPa)	7.31	8.21 5.61	6.99	7.93 4.95	6.84	7.77 4.67

The growth of IMC layer under specific aging temperature is found to follow a parabolic law.

$$\Delta h_{IMC} = kt^n \quad (2.6)$$

Where Δh_{IMC} is the growth of IMC thickness h_{IMC} , k is the growth rate constant, t is the stressing time and n is the time constant. The time constant n is around 0.5 when the IMC growth is diffusion controlled [22, 84-85]. Thus, the growth rate k is correlated to the diffusion coefficient D and the equation can be modified to:

$$\Delta h_{IMC} = \sqrt{Dt} \quad (2.7)$$

Yoon [84] measured the IMC growth of Pb-free solder on organic solderability preservative (OSP)-treated PCB under isothermal aging. The total IMC thickness and the fitting constant are represented in Fig. 2.5 and Table 2.2.

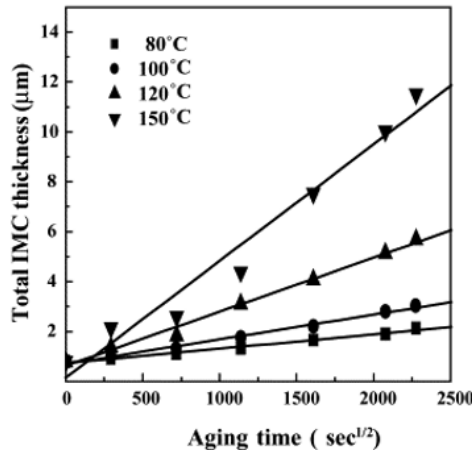


Fig. 2.5: Total IMC growth with respect to aing time [84]

Table 2.2: Constant of the IMC growth [84]

Temperature (°C)	k^2 ($\times 10^{-19}$ m ² /s)	Time exponent (n)
80	3.27	0.54
100	9.8	0.52
120	46.66	0.54
150	218.08	0.48

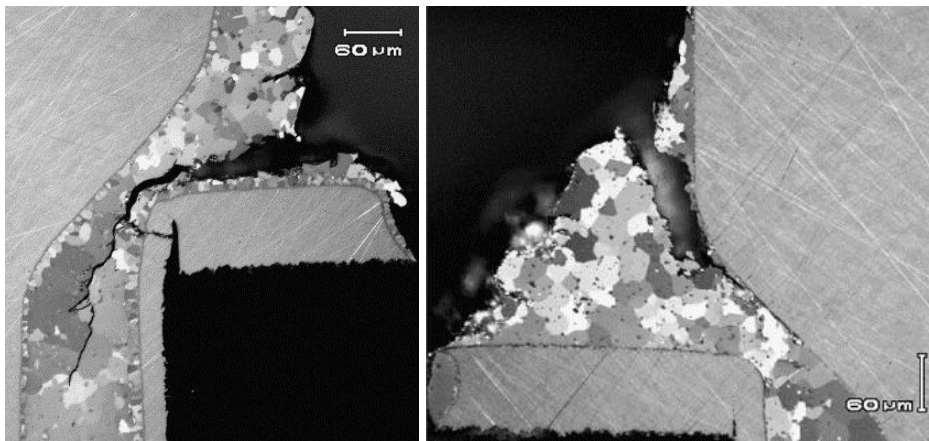
It is noted that the growth constant k is highly activated by temperature, since the diffusion coefficient D can be described by (2.8).

$$D = D_0 \exp\left(-\frac{E_a}{RT}\right) \quad (2.8)$$

Where D_0 is the diffusion coefficient at reference temperature and E_a is the activation energy. Yoon [84] derived the Arrhenius plot for total IMC growth and obtained the activation energy to be 76.17 kJ/mol.

2.3 Failure mechanisms due to thermal load

As mentioned in chapter 1, recrystallization takes place during thermal fluctuation. The recrystallized region provides favorable sites for fatigue cracks to initiate and propagate under cyclic thermo-mechanical stress. Laurila [63] compared the failure mechanisms of solder joints subjected to PC and TC loading conditions. As exhibited in Fig. 2.6, both failures are found to be the same, which is recrystallization-assisted crack nucleation and propagation. The difference is that PC is detected to facilitate recrystallization and enhance the IMC growth.



(a) PC

(b) TC

Fig. 2.6: Optical micrograph from cross-section of the interconnection taken with polarized light after 3000 cycles [63]

Libot [86] has investigated the microstructural evolution of solder joints subjected to thermo-mechanical load and the process is illustrated in Fig. 2.7. The global recrystallization and coarsening of Ag_3Sn occurs as a result of the thermal load and is followed by dislocation motion and rearrangement. At the region with high strain, $\beta\text{-Sn}$ sub-grains are created and they rotate under cyclic strain, which leads to higher grain disorientation and formation of high angle grain boundaries. The crack propagates intergranularly by grain boundary sliding (GBS) resulting in crack formation along the high angle grain boundaries, as displayed in Fig. 2.8.

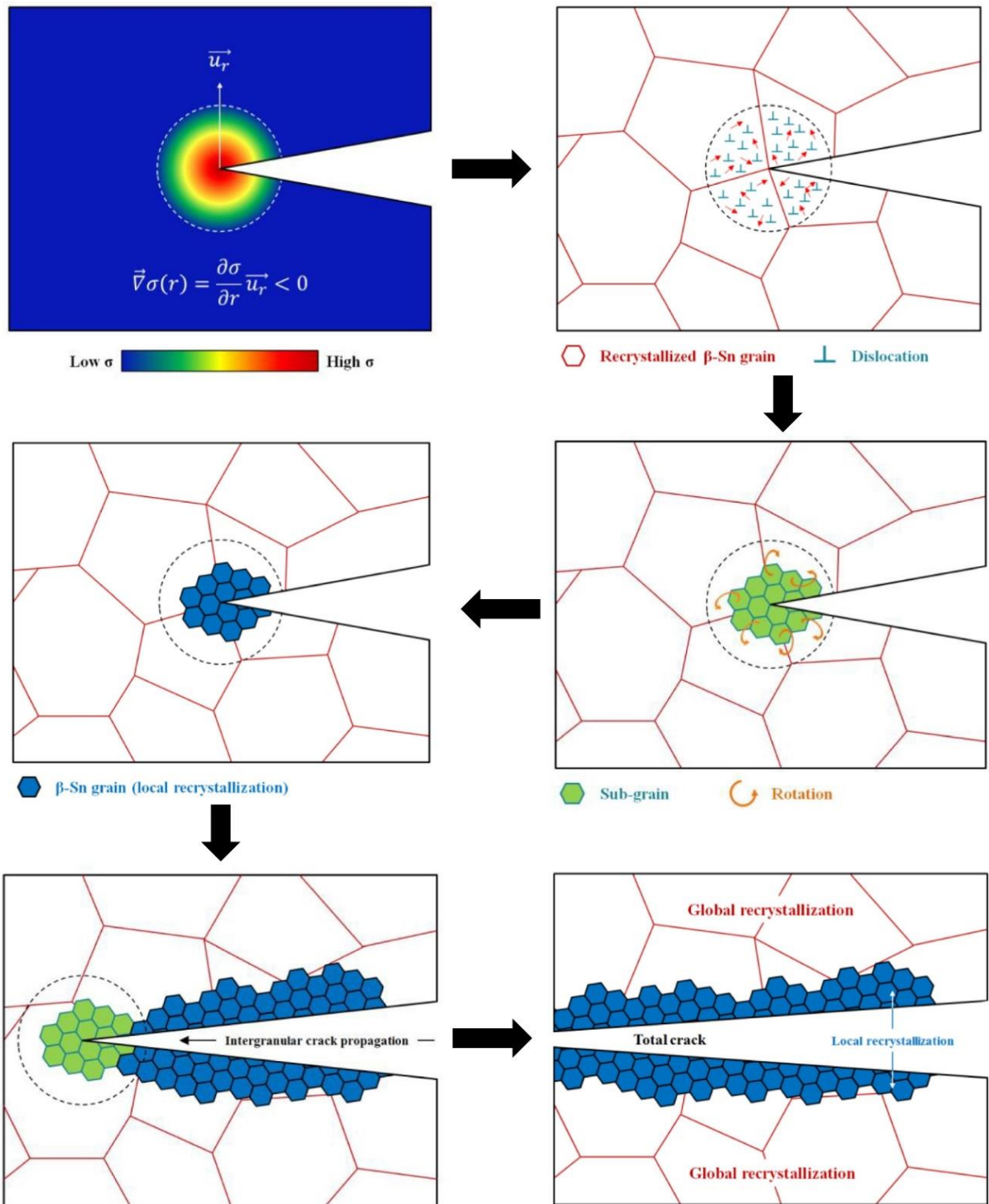


Fig. 2.7: Microstructural evolution of solder subjected to thermal-mechanical load [86]

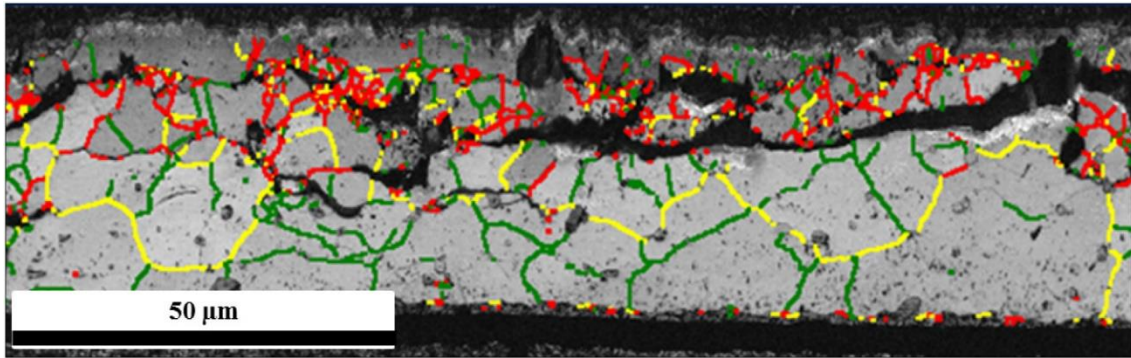


Fig. 2.8: Disorientation of the grain boundaries [86]

(green: 0° – 15° , yellow: 15 – 45° , red: $>45^{\circ}$)

The coarsening of Ag_3Sn happens due to the diffusion of Ag through the β -Sn matrix [87] and the precipitates are distributed in the Sn matrix with larger spacing, which decreases the resistance of the solder to dislocation motion. The large IMC precipitates also provide good nucleation sites and therefore facilitate recrystallization [86]. The study of Yin [17] shows that, the recrystallization is essentially complete after 25% to 50% of the characteristic life and fatigue cracks propagate through the recrystallized region until final failure. The stiffness of the recrystallized region of the solder joint is reduced [88] and grain boundary is weakened, which promotes creep rupture in the solder joint [89].

β -Sn exhibits a body-centered tetragonal structure with highly anisotropic properties, where the CTE and stiffness characteristics significantly depends on the crystal orientation [6, 90-92], as shown in Fig. 2.9. The ratio of the lattice constant c/a is 0.5456. The CTE and stiffness for the β -Sn unit cell is greatest along the c -axis, which results in complex stress evolution in the solder joint subjected to TC or PC load. The random orientation of Sn crystals could explain the scattering data from the test [8].

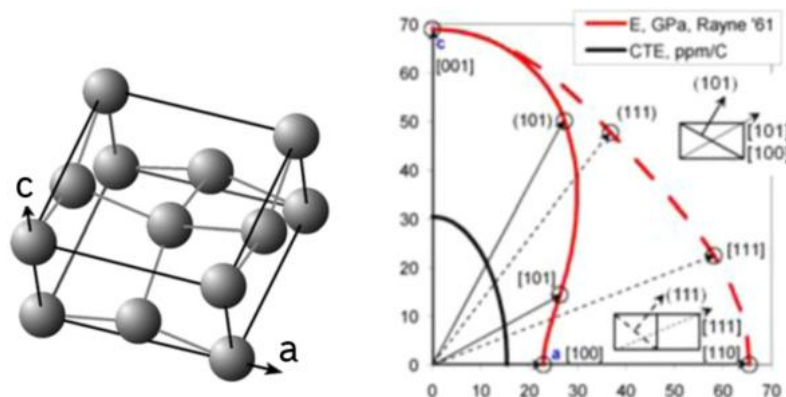


Fig. 2.9: Schematic of unit cell of β -Sn and the CTE and elastic modulus of Sn on different planes [92]

2.4 Failure mechanisms due to current loads

Apart from the thermo-mechanical fatigue induced from the self-heating of components, EM-induced degradation and failure under current loads are becoming more and more critical with the trend of miniaturization of electronic systems. EM is a diffusion-controlled process. Electrons migrate in response to the applied electric field, collide with the metal ions and exchange momentum, which is also called electron wind force. Usually, there is no net movement of the ion because it returns to its equilibrium position in the lattice [93]. The applied current provides work to move the ion forward and lowers effective barrier height in the direction of the current flow, as shown in Fig. 2.10 [94]. The activated metal ions are displaced and transported along the electron flow direction, which can result in hillock formation at the anode. Vacancies are generated at the cathode and lead to degradation and early failure of solder joints [95-96].

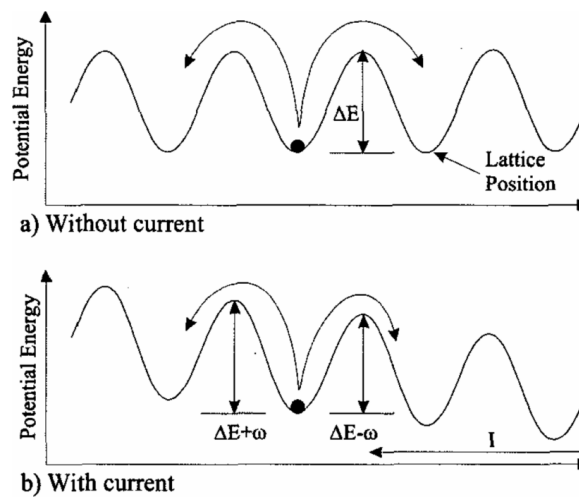


Fig. 2.10: Potential energy fields without and with current flow [94]

It has been reported that EM becomes a reliability problem in flip chip solder bumps, when the current density is around or higher than $1 \times 10^4 \text{ A/cm}^2$ [97-98]. The EM-induced damage modes can be classified into two categories [99]: i) void formation; ii) Rapid dissolution of UBM and IMC. Chang [100-101] performed in-situ three-dimensional (3D) synchrotron X-ray laminography (SRCL) analysis on flip-chip solder joints subjected to a current of $7.5 \times 10^3 \text{ A/cm}^2$. The images from SRCL analysis are reconstructed and plotted in Fig. 2.11 with respect to stressing hours. The voids are generated at the top of the solder ball, where the current crowding occurs. More voids are created and voids accumulate with longer stressing time.

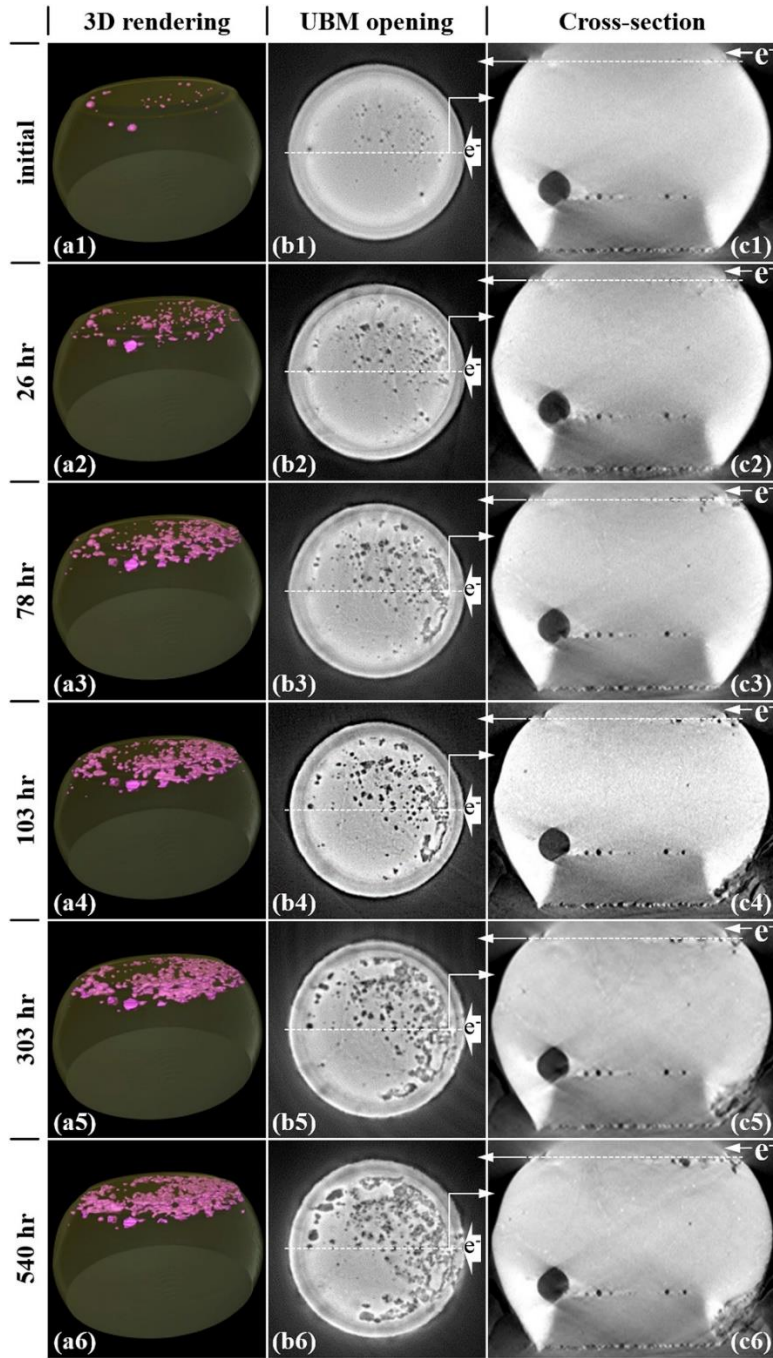


Fig. 2.11: Void formation at different stages of EM test [100]

The self-heating of the component results in thermal gradients in the assembly. The thermal gradients and consequent thermally induced stress might lead to thermomigration (TM) and stressmigration (SM), which could also contribute to the failure [102]. Dalleau [102-103] proposed an algorithm to simulate the migration phenomenon owing to the current, thermal and mechanical load in the assembly.

$$\vec{J}_A = \frac{N}{k_B T} e Z^* \vec{j} \rho D_0 \exp\left(-\frac{E_a}{k_B T}\right) \quad (2.9)$$

$$\vec{J}_{\text{Th}} = -\frac{NQ^*D_0}{k_B T^2} \exp\left(-\frac{E_a}{k_B T}\right) \text{grad } T \quad (2.10)$$

$$\vec{J}_S = -\frac{N\Omega D_0}{k_B T} \exp\left(-\frac{E_a}{k_B T}\right) \text{grad } \sigma_H \quad (2.11)$$

$$\text{div}(\vec{J}_A) = \left(\frac{E_a}{k_B T^2} - \frac{1}{T} + \alpha \frac{\rho_0}{\rho}\right) \vec{J}_A \text{grad } T \quad (2.12)$$

$$\text{div}(\vec{J}_{\text{Th}}) = \left(\frac{E_a}{k_B T^2} - \frac{3}{T} + \alpha \frac{\rho_0}{\rho}\right) \vec{J}_{\text{Th}} \text{grad } T \quad (2.13)$$

$$\begin{aligned} \text{div}(\vec{J}_S) &= \left(\frac{E_a}{k_B T^2} - \frac{1}{T}\right) \vec{J}_S \text{grad } T \\ &+ \frac{NQ^*D_0}{3k_B^3 T^3} \vec{j}^2 \rho^2 e^2 \exp\left(-\frac{E_a}{k_B T}\right) \end{aligned} \quad (2.14)$$

$$\begin{aligned} &+ \frac{2EN\Omega D_0 \alpha_1}{3(1-\nu)k_B T} \exp\left(-\frac{E_a}{k_B T}\right) \left(\frac{1}{T} - \alpha \frac{\rho_0}{\rho}\right) \text{grad}^2 T \\ &+ \frac{2EN\Omega D_0 \alpha_1}{3(1-\nu)k_B T} \exp\left(-\frac{E_a}{k_B T}\right) \frac{\vec{j}^2 \rho^2 e^2}{3k_B T^2} \end{aligned}$$

Where $\vec{J}_A, \vec{J}_{\text{Th}}, \vec{J}_S$ represent the material flux resulting from electromigration, thermomigration and stressmigration respectively. $\text{div}(\vec{J}_A), \text{div}(\vec{J}_{\text{Th}})$ and $\text{div}(\vec{J}_S)$ are the corresponding divergence of material flux due to the three migration mechanisms. The meaning of the parameters is listed in Table 2.3. The time dependent atomic concentration density N can be calculated via adding up all the divergence of material flux [103].

$$\text{div}(\vec{J}_A + \vec{J}_{\text{Th}} + \vec{J}_S) + \frac{\partial N}{\partial t} = 0 \quad (2.15)$$

Table 2.3: Main parameters for migration mechanisms

D_0	Diffusion coefficient at infinite temperature
E	Young's modulus
e	Electron charge
E_a	Activation energy
\vec{j}	Current density
k_B	Boltzmann constant
N	Atomic density
Q^*	Heat of transport
T	Local temperature
Z^*	Effective charge number
ρ	Resistivity at local temperature
ρ_0	Resistivity at reference temperature
α	Temperature coefficient of resistivity
α_1	Coefficient of thermal expansion
ν	Poisson ratio
σ_H	Hydrostatic stress
Ω	Atomic volume

Apart from the void formation, migration of material also results in a polarity effect in IMC growth. The IMC growth is accelerated at anode side and hindered at cathode side. It can be concluded from many studies [104-107] that the IMC growth at anode side gradually transforms from the parabola-like curve from aging into linear-like relationship due to EM, which weakens the resistance of solder joint against TMF.

The Sn grain orientation also plays a profound role in the EM-induced failure mechanism. The damage mode i) void formation results from dominant Sn self-diffusion. The damage mode ii) rapid dissolution of UBM and IMC is owing to fast interstitial diffusion of Cu and Ni through Sn. When the c-axis of Sn is perpendicular to current direction, damage mode i) is likely to occur,

as displayed in the solder bump Nr. 2 in Fig. 2.12. Damage model ii) is dominating when the c-axis of Sn is parallel to the current direction [108-109], as shown in the solder bump Nr. 1 in Fig. 2.12. Chen [110] modified the above equations of atomic flux calculation and took the angle θ between the current direction and c-axis of β -Sn into account.

$$\vec{J}_A = \frac{N}{k_B T} e Z^* \vec{j} \rho (D_a + D_c \cos^2 \theta) \quad (2.16)$$

D_a and D_c represent the diffusivity along a-axis of β -Sn and diffusivity along c-axis of β -Sn.

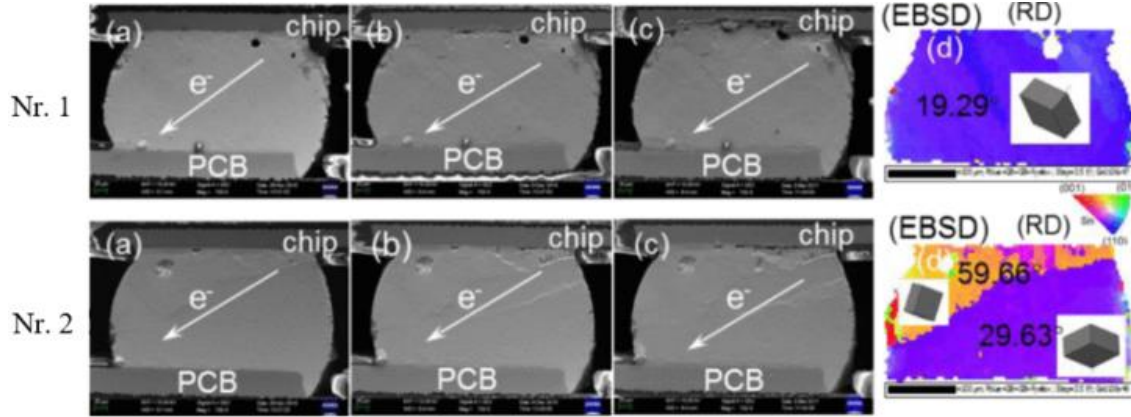


Fig. 2.12: In situ observation of the cross-sectional microstructure of solder bumps after EM for (a) 100 h, (b) 250 h, (c) 500 h and (d) EBSD map [109]

2.5 Statistics

The reliability is evaluated by fitting the lifetime data gathered from representative samples to a statistical lifetime distribution. The Weibull distribution is commonly used for assessment of product reliability and analysis of lifetime data. It provides reasonably accurate prediction of life time with small amount of samples. The cumulative distribution function (CDF) $Q(t)$ of the Weibull distribution describes the probability that the failure takes place earlier to or equal to time t , which is also known as unreliability. The $Q(t)$ of a three-parameter Weibull is described with respect to failure time t :

$$Q(t) = 1 - e^{-\left(\frac{t-\gamma}{\eta}\right)^\beta} \quad (2.17)$$

where β is the shape parameter, η is the scale parameter and also known as characteristic lifetime, γ is the location parameter and also known as failure-free time. When γ equals to 0, the two-parameter Weibull distribution is obtained. The parameters of the Weibull distribution are of significance physically. For example, the failure mode is characterized by the shape parameter β . The scale parameter η is related to the case when 63.2% of components have failed. Other parameters are also utilized to assess the reliability of the product, such as mean time to failure

(MTTF) and the CAP value. The CAP value is defined as the lifetime when 6.7% of components have failed, which indicates the early failures of the components.

$$MTTF = \gamma + \eta \Gamma\left(\frac{1}{\beta} + 1\right) \quad (2.18)$$

$$CAP = \gamma + \eta(-\log [1 - fr])^{\frac{1}{\beta}} \quad (2.19)$$

The gamma function is defined as,

$$\Gamma(n) = \int_0^{\infty} e^{-x} x^{n-1} dx \quad (2.20)$$

The parameters of the Weibull distribution are derived via curve-fitting of the test data set. The commonly used fitting methods are rank regression (RR) and maximum likelihood (ML) estimation. There are different types of data that can be obtained via tests. When the exact lifetime data are known, the data are defined as "complete data". When the unit is not failed until the end of the test and will continue to operate successfully for an additional time, these data are known as "suspended" or "right censored" data. When the exact lifetime is unknown, but the failure occurs during a known time range, these data are "interval" or "left censored" data. The lifetime data and their corresponding censoring are analyzed to obtain the Weibull lifetime fit.

Sudden-death Weibull testing is implemented in this work to reduce the test time and cost. Identical test units are divided into r groups with n units in each group. The test is stopped once the first failure occurs. The weakest unit that fails first provides the complete data while the remaining units of the group are "right censored" data. It requires longer testing time and more cost if all the units are tested to final failure. The precision of the statistical analysis is also lowered with reducing the amount of testing units. Therefore, the sudden-death method is utilized. A sudden-death line is obtained via data-fitting, which represents the unreliability of median rank (MR)% of the units instead of the entire population. The Weibull distribution line of the total population is derived by shifting the sudden-death line.

$$MR = \frac{i-0.3}{n+0.4} \times 100 \quad (2.21)$$

where i is the failure order number.

2.6 Lifetime model

The solder joint fatigue models can be categorized into mainly five groups [111]: stress-based, strain-based, energy-based, damage-based and empirical models. Stress-based fatigue models typically apply to components subjected to vibrational or mechanical loads. Table 2.4 summarizes the fatigue models in the other four categories.

Table 2.4: Fatigue models and classification [111]

Fatigue model	Plastic strain	Creep strain	Energy	Damage	Other (empirical)
Coffin-Manson	X				
Total strain	X				
Soloman	X				
Engelmaier	X				
Miner	X	X			
Knecht and Fox		X			
Syed		X	X		
Akay			X		
Liang			X		
Henrich			X		
Pan			X		
Darveaux			X	X	
Stolkarts				X	
Norris and Landzberg					X

For a rapid lifetime prediction, empirical models like Norris-Landzberg's model can be implemented, where the correlation of test conditions and use conditions can be interpreted by temperature excursion range and frequency conditions. The acceleration factors (AF) from the empirical models can be calculated as,

$$AF = \left(\frac{\Delta T_t}{\Delta T_u}\right)^2 \left(\frac{f_u}{f_t}\right)^{1/3} \left(\frac{\Phi_u}{\Phi_t}\right) \quad (2.22)$$

where ΔT , f and Φ are the temperature range, frequency and isothermal fatigue lifetime under test conditions (t-subscript) and under use conditions (u-subscript). To investigate the reliability of solder interconnects on the basis of damage mechanisms, the stress and strain in the solder joint induced by the loads should be obtained. The stress-strain data are normally evaluated by FEM simulation since strain gauges are not applicable anymore due to the shrinking size of the electronic packages.

The strain-based models are derived on the basis of the constitutive equation which is described as

$$\varepsilon = \varepsilon_e + \varepsilon_p + \varepsilon_c \quad (2.23)$$

where ε , ε_e , ε_p , ε_c represent the total shear strain, elastic strain, plastic strain and creep strain. The widely-used Coffin-Manson model is proposed to correlate the number of cycles to failure N_f and plastic strain amplitude $\Delta\varepsilon_p$.

$$\frac{\Delta\varepsilon_p}{2} = \varepsilon_f' (2N_f)^c \quad (2.24)$$

ε_f' is the fatigue ductility coefficient and c is the fatigue ductility exponent. The elastic deformation is taken into account by adding Basquin's equation to the Coffin-Manson model.

$$\frac{\Delta\varepsilon}{2} = \frac{\sigma_f'}{E} (2N_f)^b + \varepsilon_f' (2N_f)^c \quad (2.25)$$

$\Delta\varepsilon$ is the total strain, σ_f' is the fatigue strength coefficient and E is the elastic modulus, b is the Basquin's exponent.

The Engelmaier fatigue model is derived considering total shear strain $\Delta\varepsilon$.

$$N_f = \frac{1}{2} \left[\frac{\Delta\varepsilon}{2\varepsilon_f'} \right]^{1/c} \quad (2.26)$$

Where c is a function of frequency f and temperature T . $c = -0.442 - 6 \times 10^{-4}T + 1.74 \times 10^{-2} \ln(1 + f)$.

The deformation is primarily elastic in high cycle fatigue (HCF), while the failure is mainly governed by plastic strain in low cycle fatigue (LCF). The creep strain can be taken into account by implementation of Miner's rule. N_f can be calculated from the number of cycles to failure due to plastic strain fatigue (N_p) and due to creep fatigue (N_c).

$$\frac{1}{N_f} = \frac{1}{N_p} + \frac{1}{N_c} \quad (2.27)$$

The application of the discussed fatigue models mainly depends on the test conditions, such as temperature range, ramp rate and dwell time in TC. In this work, the thermal fluctuation in the assembly is generated by Joule heating. The solder interconnect is exposed to high thermo-mechanical strain within short pulse duration. Therefore, a plastic strain-based lifetime model is likely to be applicable in this work, only considering TMF.

To assess the lifetime of solder joints owing to EM-induced failure, Black's equation [112] is well-known.

$$MTTF = A_j^{-n} \exp\left(\frac{E_a}{k_B T}\right) \quad (2.28)$$

where A is constant, \bar{j} is current density, n is exponent constant for current density, E_a is activation energy, k_B is Boltzmann constant and T is the average temperature. Black's equation is derived by studying Aluminum lines where the current is evenly distributed. It is concluded that Black's equation can be applied to assess the solder lifetime [113], although the current is normally nonuniformly distributed in solder joints. Many studies have fitted the test data to quantify the activation energy E_a and exponent constant n , as illustrated in Fig. 2.13 (a). Fig. 2.13 (b) shows the data fitting for SAC 405 and the activation energy is derived to be 0.8 eV [114]. Table 2.5 lists the parameters for Black's equation in some literature sources. The prediction of Black's equation might overestimate the lifetime [97]. This is caused by the current crowding effect and local enhanced Joule heating. Large n value may be associated to severe Joule heating within the solder and depend on the failure criterion chosen [115]. Nicholls [116] and his colleagues have investigated the impact of different base surface finishes on the Sn/Ag bump electromigration.

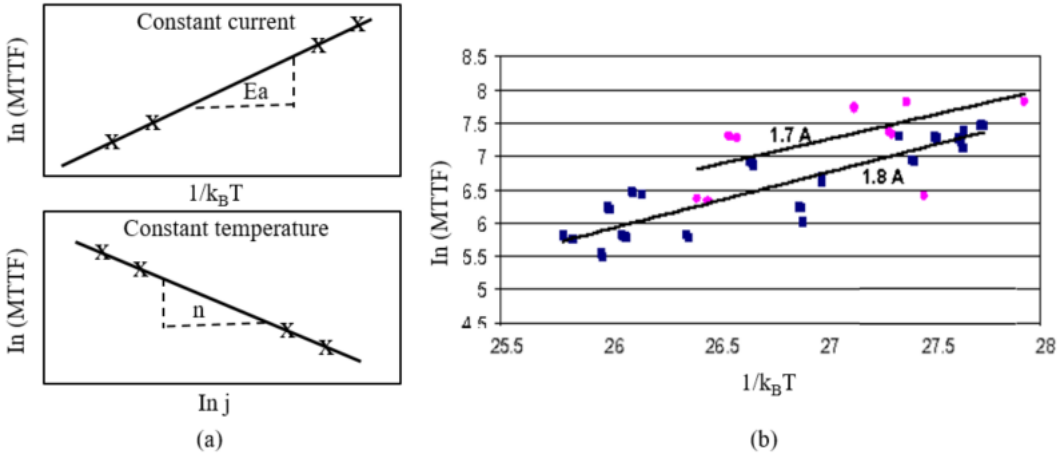


Fig. 2.13: Fitting of current density exponent and activation energy (a) calculation of current density exponent and activation energy (b) determination of activation energy of SAC 405 [114]

Table 2.5: Parameters for Black's equation

Solder	n	E_a [eV]	Reference
SAC solder series	1-2	0.64~0.72 for Cu UBM 1.03~1.11 for Ni UBM	[97, 115, 117-118]
	3.32	0.78	[115]
	4.6	1.63	[116, 119]

It has been concluded that the implementation of Black's equation highly depends on the solder shape, local heat generation and chosen failure criterion [115]. Most of the studies [115-119] of

EM failure are focusing on flip chip solder bumps due to the UBM structure and the resultant current crowding effect. Hence no effective parameters can be directly utilized for solder joints of shunt components.

Besides, the reviewed lifetime models only consider failure mechanisms of TMF or EM individually. When the electronic assembly is subjected to high current pulses and high environmental temperature, both TMF and EM can contribute to the failure. The coupling of the two failure mechanisms cannot be captured by actual lifetime models. Therefore, modification of the available lifetime models or proposal of new lifetime models are required to describe the complex failure modes under power cycling test conditions, when neither TMF nor EM can be neglected. These open points are challenging yet very interesting to be investigated in this work.

3 Materials and experiments

This chapter illustrates the specification of shunt components and analyzes the self-heating behavior of the components. The setup of the power cycling tests is clarified and various loading conditions with different current range, pulse duration and ambient temperature are applied to the test units to collect lifetime data.

3.1 Test components

3.1.1. Shunts

Shunt resistors are primarily utilized for current sensing beyond the measuring devices range. Shunt components yield relatively high reliability under passive TC tests. This can be attributed to the small CTE mismatch between the shunts (≈ 16.5 ppm/K) and PCBs (≈ 15 ppm/K). Apart from the external thermal fluctuation from the environment, shunt components are often experiencing switching cycles in automotive applications. The active load will introduce thermal gradients in the electronic assembly and additional thermal mismatch. Therefore, it is of great significance to investigate and understand the performance of shunts under active load.

Fig. 3.1 displays the shunt components which are investigated in this work. The components mainly consist of two terminals, protective coating and resistive element. The resistive element is marked with dashed line in the configuration and is capsulated with the dark coating material. The main dimensions of the components are listed in Table 3.1.

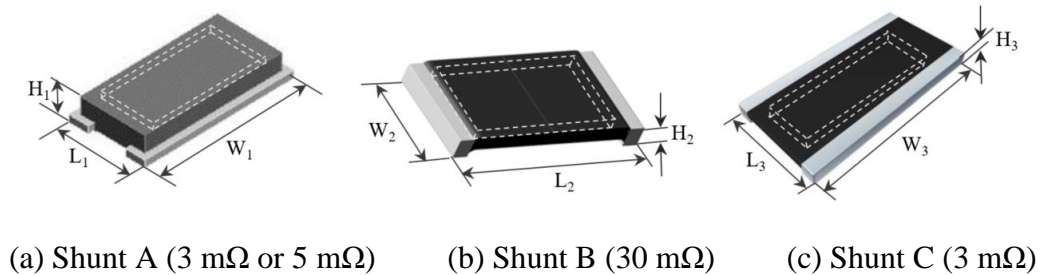


Fig. 3.1: Configuration of the shunt components

Table 3.1: Main dimensions of the shunts

	L_1	W_1	H_1
Dimension [mm]	2.55 ± 0.25	5.00 ± 0.25	1.00 ± 0.15
	L_2	W_2	H_2
Dimension [mm]	5.08 ± 0.25	2.54 ± 0.25	0.635 ± 0.15
	L_3	W_3	H_3
Dimension [mm]	2.54 ± 0.254	5.08 ± 0.254	0.508 ± 0.178

The terminals of shunt A are normally coated with few micrometers of inner plating (Ni) and outer plating (Sn), as shown in Fig. 3.2. Ni serves as diffusion barrier to restrain the fast consumption of Cu [120]. The Sn plating as outer plating is utilized to improve the solderability of the shunt. Apart from the original shunt A with Ni/Sn plating, shunt A* with only outer plating (Sn) is also investigated to study the interfacial reaction and its influence on the reliability.

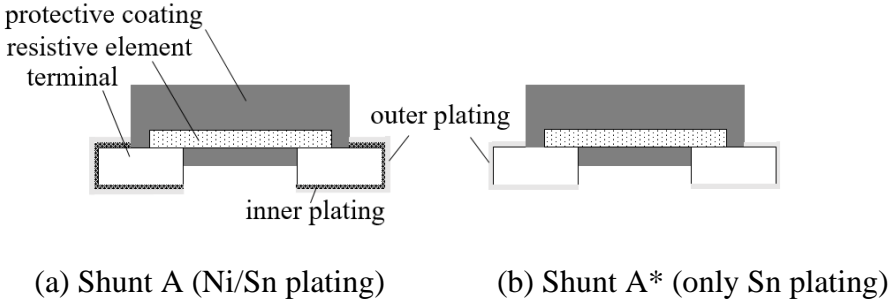


Fig. 3.2: Terminal plating of the shunts

3.1.2. Components specification

a) Shunt A

The product information of shunt A specifies that the maximum power dissipation of the shunt is a function of the duration of a single pulse. The correlation of the maximum energy and pulse duration is displayed in Fig. 3.3.

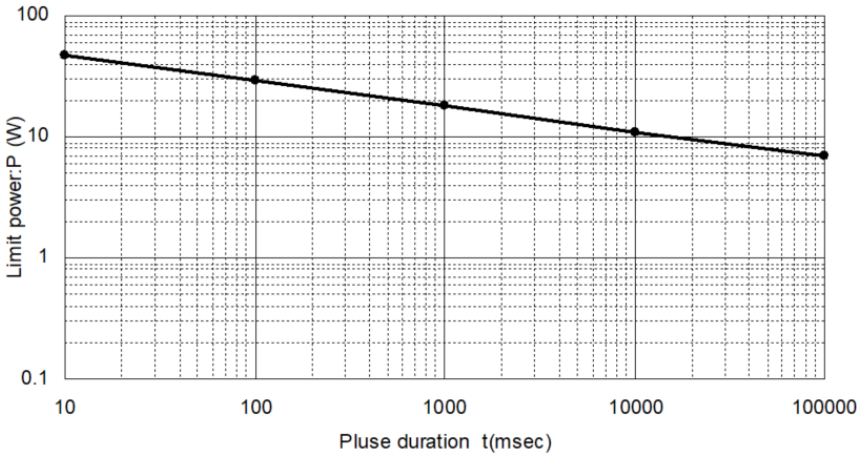


Fig. 3.3: Maximum energy of shunt A

The maximum current I within the specification the shunt can be calculated by,

$$I = \sqrt{\frac{P}{R}} \tag{3.1}$$

where P is the power limit and R is the resistance. Table 3.2 lists the limiting loading conditions of shunt A with different pulse durations.

Table 3.2: Maximum current of shunt A

Shunt A	Pulse duration (s)	Power limit (W)	Current limit (A)
3 mΩ	0.1	30	100
	2	19	79.58
	3	18	77.46
	4	17	75.27
5 mΩ	0.1	30	77.45
	2	19	61.64
	3	18	60
	4	17	58.31

b) Shunt B

The correlation of the maximum energy or pulse dissipation of shunt B and the pulse duration is described in Fig. 3.4. The resistance of shunt B is 30 mΩ. Due to its higher resistance, short current pulses with duration of 1s have been investigated in this work. Based on Eqn (3.1), the maximum current allowed for shunt B is evaluated to be 14 A, as documented in Table 3.3.

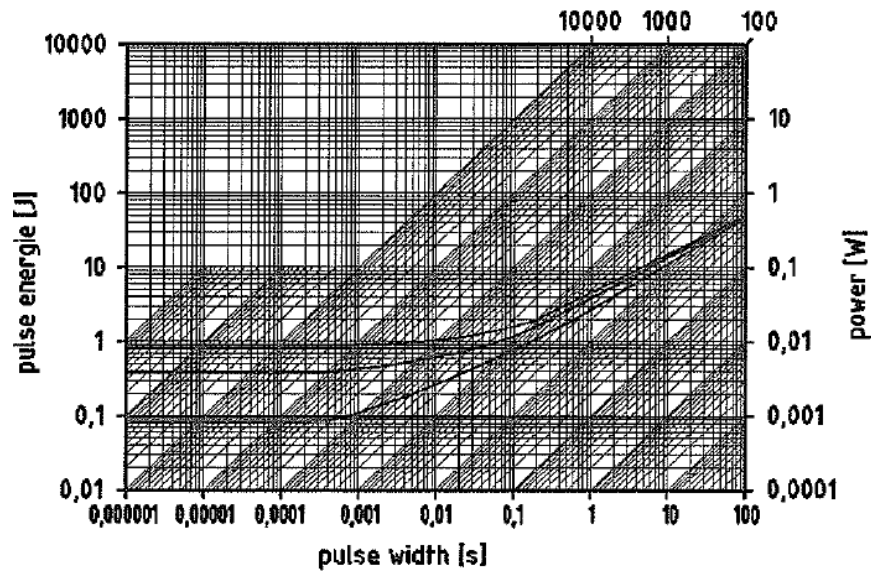


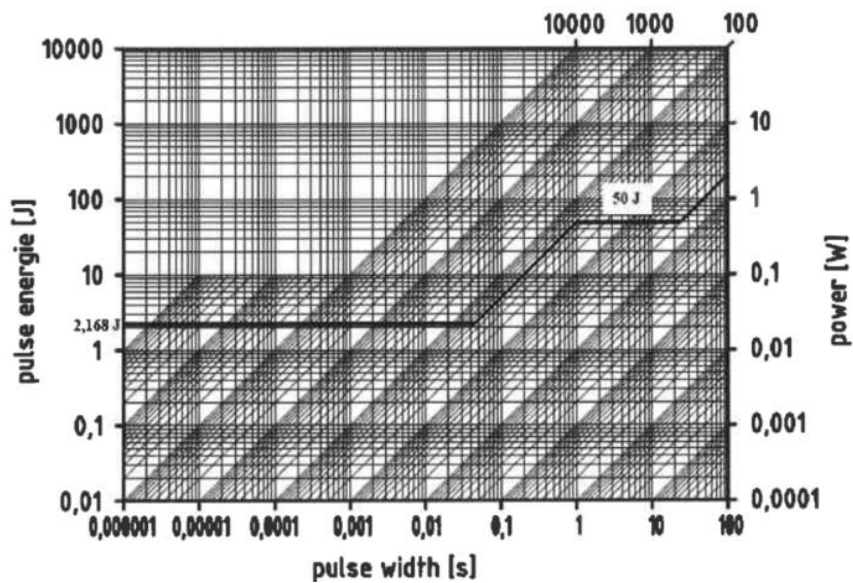
Fig. 3.4: Maximum energy of shunt B

Table 3.3: Maximum current of shunt B

Shunt B	Pulse duration (s)	Power limit (W)	Current limit (A)
30 mΩ	1	6	14

c) Shunt C

Fig. 3.5 illustrates the correlation of the maximum energy of shunt C and the pulse length of the current. Table 3.4 presents the evaluation of the allowed maximum current for shunt C.

**Fig. 3.5:** Maximum energy of shunt C**Table 3.4:** Maximum current of shunt C

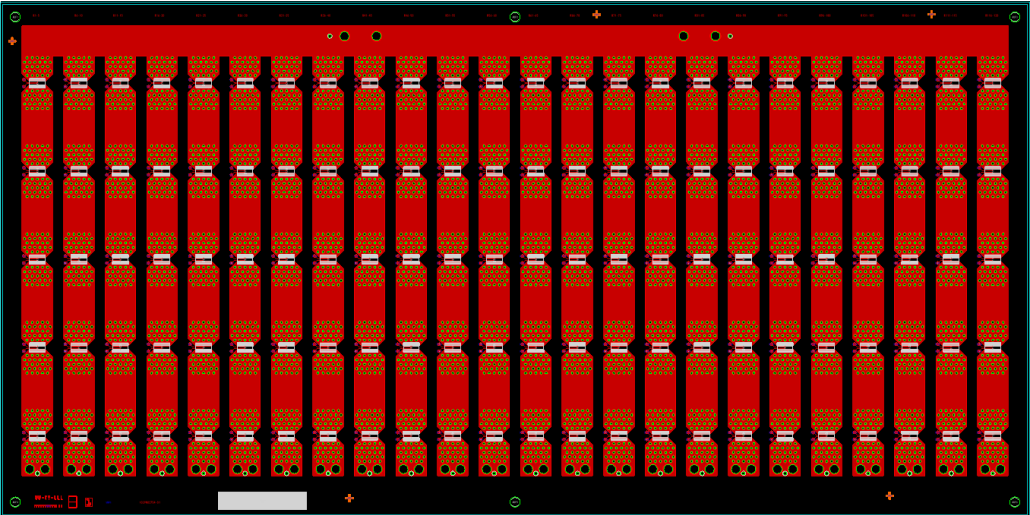
Shunt C	Pulse duration (s)	Power limit (W)	Current limit (A)
3 mΩ	2	25	91.29
	3	16.67	74.53
	4	12.5	64.55

The testing conditions of this work are defined within the above component specifications to avoid that early failure occurs in the components.

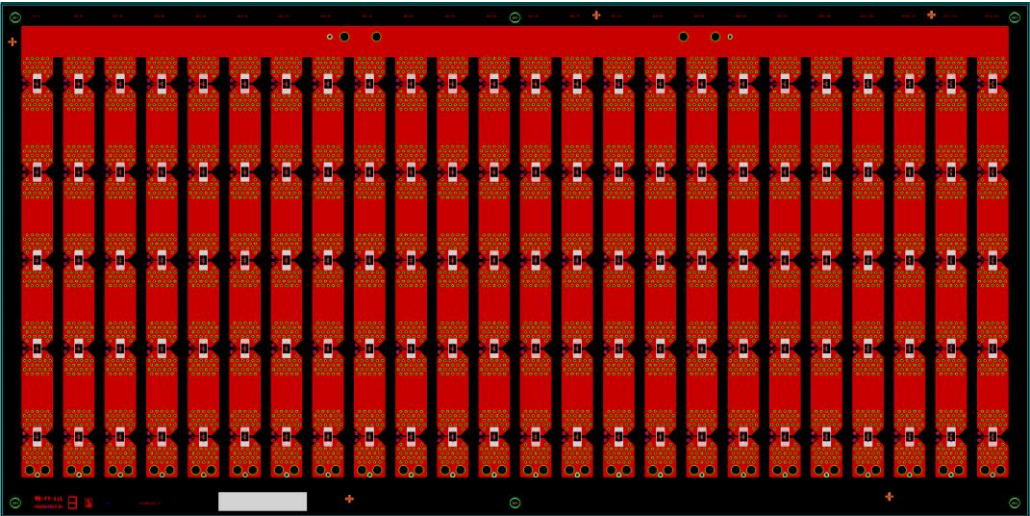
3.2 Power cycling test

3.2.1 Test layout

The shunt A (A*) and shunt C share the same footprint and test layout, while the test layout of shunt B is slightly modified due to the different dimensions of the footprint. The test layouts are displayed in Fig. 3.6. 24 rows of components can be mounted on the PCB with 5 components in a row. The shunt rows are connected to separate power input and to the same ground. The through holes are placed in the PCBs so that the cooling behavior of the assembly after current stressing can be improved. The layout designs are delivered to PCB suppliers for production. The shunt components are further assembled on the PCBs via SMT process with SAC 405 solder paste. In this work, the thickness of the stencil is 150 μm .



(a) Test layout for shunt A (A*) and shunt C



(b) Test layout for shunts B

Fig. 3.6: Test layouts for shunt components

3.2.2 Cable soldering

Fig. 3.7 presents the cable soldering for the power cycling test. The thick copper cables are soldered at the front and at the end of the shunt row, which are connected to the input and ground of the power supply. The black and red cables are soldered to the shunt row for resistance measurement. The thermocouples are attached on the top of the shunt components via an UV glue to monitor the temperature fluctuation during the test. Due to the testing capacity, 15 shunt rows per PCB are electrically connected to the power supply and are further tested.

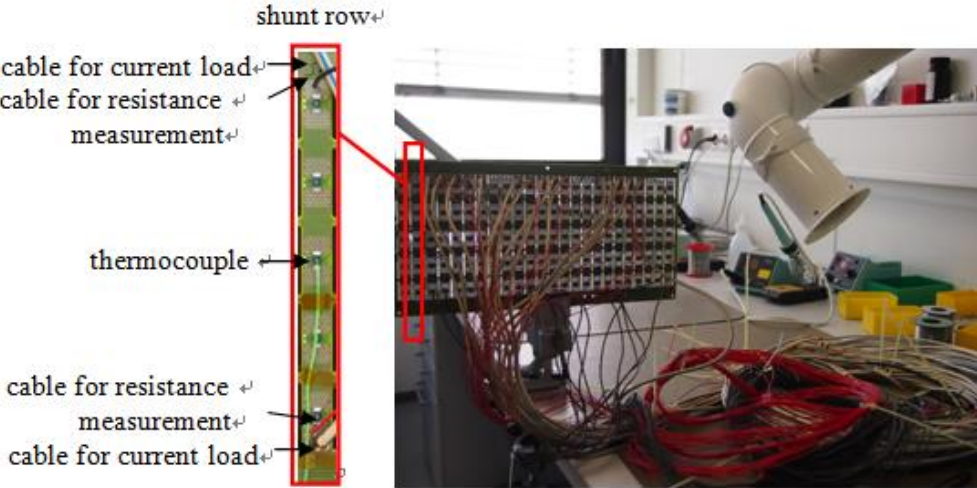
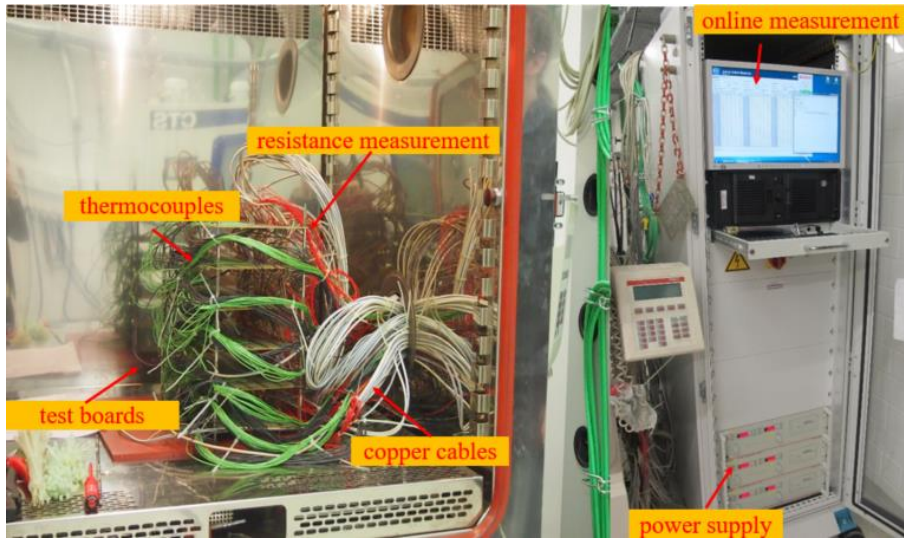


Fig. 3.7: Cable soldering for the power cycling test

3.2.3 Test setup

Six PCBs are placed in the climate chamber, as well as the soldered cables and thermocouples, as displayed in Fig. 3.8. The schematic diagram of the power supply is illustrated in Fig. 3.9. There are three power supplies in total. Each power supply is connected to 30 relays and 30 shunt rows. The power supply switches on each relay sequentially and provides the same current input to the connected shunt row. Therefore, every two PCBs are connected to one power supply and undergo the same loading conditions.



(a) Temperature chamber

(b) Test system

Fig. 3.8: Configuration of test vehicle

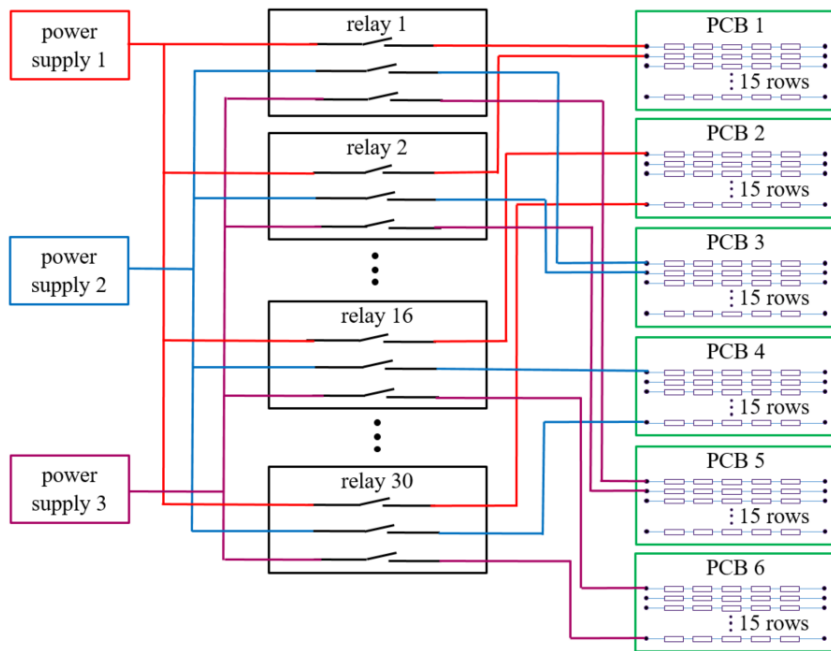


Fig. 3.9: Schematic diagram of the power supply

Online measurement is implemented to monitor the resistance and temperature of the assembly during the test. As shown in Fig. 3.10, failure warning is reported when the measured resistance exceeds 150% of the original value and an infinite value of resistance is displayed in the online measurement system. After ten repeated measurements of the failure warning, the shunt row is determined to meet the failure criterion and the corresponding number of power cycles will be documented as lifetime data. This failure criterion is defined to avoid the pseudo failure due to

interference of the measurement signals. The current input of the failed shunt row is automatically switched off after reporting the failure.

PCB1						PCB2						PCB3								
Nr.	Active	Cycle	R(@t2)	T(@t1)	T(@t2)	Status	Nr.	Active	Cycle	R(@t2)	T(@t1)	T(@t2)	Status	Nr.	Active	Cycle	R(@t2)	T(@t1)	T(@t2)	Status
1	true	2988	1,888 Ω	106,7°C	90,7°C	ok	1	true	8174	2,035 Ω	105,2°C	90°C	ok	1	true	8174	1,959 Ω	99,7°C	88,7°C	ok
2	true	8174	9,9E+37 Ω	9,9E+37°C	9,9E+37°C	Fail	2	true	8174	2,256 Ω	96,9°C	90,2°C	ok	2	true	8174	2,087 Ω	95,1°C	88,7°C	ok
3	true	8174	9,9E+37 Ω	9,9E+37°C	9,9E+37°C	Fail	3	true	8174	1,67 Ω	92°C	90,1°C	ok	3	true	8174	2,161 Ω	96,9°C	88,8°C	ok
4	true	8174	9,9E+37 Ω	9,9E+37°C	9,9E+37°C	Fail	4	true	8174	1,982 Ω	91,2°C	91,2°C	ok	4	true	8174	1,972 Ω	97,7°C	88,7°C	ok
5	true	8174	9,9E+37 Ω	9,9E+37°C	9,9E+37°C	Fail	5	true	8174	1,608 Ω	90,9°C	91°C	ok	5	true	8174	1,776 Ω	94,5°C	88,8°C	ok
6	true	8174	9,9E+37 Ω	9,9E+37°C	9,9E+37°C	Fail	6	true	8174	2,011 Ω	92,6°C	90,6°C	ok	6	true	8174	1,995 Ω	100,1°C	89°C	ok
7	true	8174	9,9E+37 Ω	9,9E+37°C	9,9E+37°C	Fail	7	true	8174	1,624 Ω	91°C	91°C	ok	7	true	8174	1,568 Ω	94,8°C	89,4°C	ok
8	true	8174	9,9E+37 Ω	9,9E+37°C	9,9E+37°C	Fail	8	true	8174	1,993 Ω	103,3°C	91,5°C	ok	8	true	8174	1,743 Ω	101,9°C	89,2°C	ok
9	true	8174	9,9E+37 Ω	9,9E+37°C	9,9E+37°C	Fail	9	true	8174	2,106 Ω	108,1°C	91,4°C	ok	9	true	8174	1,712 Ω	100,4°C	89,3°C	ok
10	true	8174	9,9E+37 Ω	9,9E+37°C	9,9E+37°C	Fail	10	true	8174	1,923 Ω	103,1°C	91,4°C	ok	10	true	8174	1,821 Ω	98,9°C	89,4°C	ok
11	true	8174	9,9E+37 Ω	9,9E+37°C	586,5°C	Fail	11	true	8174	2,235 Ω	141,4°C	91,6°C	ok	11	true	8174	1,784 Ω	95,5°C	89,4°C	ok
12	true	8174	9,9E+37 Ω	9,9E+37°C	9,9E+37°C	Fail	12	true	8174	9,9E+37 Ω	90,8°C	90,7°C	Fail	12	true	8174	1,846 Ω	98,8°C	89,3°C	ok
13	true	8174	9,9E+37 Ω	9,9E+37°C	9,9E+37°C	Fail	13	true	8174	9,9E+37 Ω	90,6°C	90,6°C	Fail	13	true	8174	1,889 Ω	99,8°C	89,4°C	ok
14	true	8174	9,9E+37 Ω	9,9E+37°C	9,9E+37°C	Fail	14	true	8174	1,986 Ω	118,7°C	90,9°C	ok	14	true	8174	1,876 Ω	100,3°C	89,2°C	ok
15	true	8174	9,9E+37 Ω	9,9E+37°C	9,9E+37°C	Fail	15	true	8174	1,955 Ω	132°C	90,7°C	ok	15	true	8174	2,009 Ω	98,5°C	88,8°C	ok
16	true	8174	1,75 Ω	101,7°C	89,8°C	ok	16	true	8174	2,02 Ω	91,4°C	89,8°C	ok	16	true	8174	1,903 Ω	95,3°C	88,2°C	ok
17	true	8174	1,8 Ω	103°C	90,1°C	ok	17	true	8174	2,566 Ω	104,2°C	90,5°C	ok	17	true	8174	1,729 Ω	91,4°C	88,5°C	ok
18	true	8174	2,018 Ω	100,6°C	90,2°C	ok	18	true	8174	2,24 Ω	95,2°C	90,5°C	ok	18	true	8174	1,976 Ω	98,8°C	88,4°C	ok
19	true	8174	1,692 Ω	103°C	90,2°C	ok	19	true	8174	1,941 Ω	93,8°C	90,6°C	ok	19	true	8174	1,688 Ω	96,6°C	88,6°C	ok
20	true	8174	1,757 Ω	91,9°C	90,2°C	ok	20	true	8174	2,06 Ω	90,6°C	90,4°C	ok	20	true	8174	1,573 Ω	103,4°C	88,6°C	ok
21	true	8174	2,229 Ω	90,9°C	90°C	ok	21	true	8174	2,062 Ω	101,3°C	91°C	ok	21	true	8174	1,873 Ω	93,3°C	88,5°C	ok
22	true	8174	1,604 Ω	98,6°C	90,1°C	ok	22	true	8174	2,06 Ω	103,4°C	91,1°C	ok	22	true	8174	1,593 Ω	98,8°C	88,7°C	ok
23	true	8174	1,703 Ω	97,5°C	90,5°C	ok	23	true	8174	1,962 Ω	102,4°C	91°C	ok	23	true	8174	1,852 Ω	98,7°C	88,8°C	ok
24	true	8174	1,724 Ω	99,3°C	90,6°C	ok	24	true	8174	2,146 Ω	98,1°C	90,9°C	ok	24	true	8174	1,447 Ω	98,9°C	88,5°C	ok
25	true	8174	1,652 Ω	108,1°C	91°C	ok	25	true	8174	2,08 Ω	104,5°C	91,3°C	ok	25	true	8174	1,746 Ω	88,1°C	88,1°C	ok
26	true	8174	2,016 Ω	101,3°C	90,8°C	ok	26	true	8174	2,139 Ω	151,6°C	91,7°C	ok	26	true	8174	1,632 Ω	95°C	88,4°C	ok
27	true	8174	1,63 Ω	109,3°C	91,2°C	ok	27	true	8174	2,039 Ω	113,1°C	91,5°C	ok	27	true	8174	1,827 Ω	88,5°C	88,4°C	ok
28	true	8174	1,659 Ω	102,3°C	91,2°C	ok	28	true	8174	2,461 Ω	110,4°C	91,3°C	ok	28	true	8174	1,868 Ω	90,4°C	89°C	ok
29	true	8174	1,558 Ω	95,3°C	91,2°C	ok	29	true	8174	2,5 Ω	100,3°C	91,3°C	ok	29	true	8174	9,9E+37 Ω	88,4°C	88,3°C	Fail
30	true	8174	2,026 Ω	99,7°C	90,7°C	ok	30	true	8174	2,14 Ω	107,7°C	91,3°C	ok	30	true	8174	1,799 Ω	94°C	88,6°C	ok

Fig. 3.10: Online measurement system

3.2.4 Loading conditions

Field-like current pulses with short duration time as shown in Fig. 3.11 are applied to the assembly. The parameters of the test profiles are specified in Table. 3.5. Power cycling tests have been performed on particular shunt components, at different ambient temperatures, with diverse pulse lengths and with various current ranges. All the cases are marked with an individual test number and the loading conditions are briefly described by the notation, which will be used in the following section to illustrate the test result. The test conditions of the shunts are selected within the specification of the components and the temperature of the PCBs is maintained below 150 °C during the test. This aims to avoid the overheating of the assembly and the occurrence of early failure in the components or in PCBs.

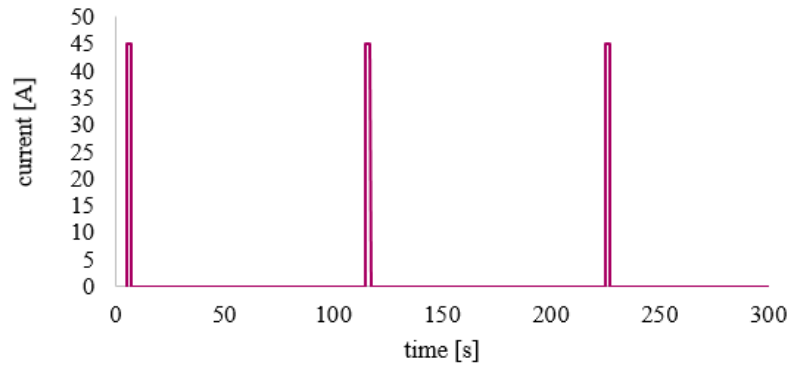


Fig. 3.11: Schematic of current profile

Table 3.5: Loading conditions for the shunts

Test	Shunt	Resistance (mΩ)	Ambient temperature (°C)	Pulse length (s)	Current range (A)	Notation	
1	A	5	90	0.1	70	70A@0.1s, 90°C	
2					60	60A@0.1s, 90°C	
3					42	42A@4s, 80°C	
4			80		4	35	35A@4s, 80°C
5						28	28A@4s, 80°C
6						34	34A@3s, 100°C
7			100		3	26	26A@3s, 100°C
8						18	18A@3s, 100°C
9						45	45A@2s, 90°C
10	A*	3	90	2	38	38A@2s, 90°C	
11					45	45A@2s, 90°C	
12					38	38A@2s, 90°C	
13	B	30	90	1	10	10A@1s, 90°C	
14					8	8A@1s, 90°C	
15					6	6A@1s, 90°C	
16	C	3	80	4	42	42A@4s, 80°C	
17					35	35A@4s, 80°C	
18			28		28A@4s, 80°C		
19	C	3	90	2	45	45A@2s, 90°C	

3.3 Self-heating of the shunts

3.3.1 Infrared (IR) thermography

An IR camera is implemented to investigate the self-heating of the shunt components. As displayed in Fig. 3.12, the PCB surface is sprayed with black camera vanish for the emissivity correction. The IR camera is fixed on a camera stand and is connected to a laptop where FLIR tools are installed. When the power supply applies current load on the assembly, the IR camera will record the temperature contour during the current stressing. The thermography measurements have been performed on shunts A (A*), B and C. Different behaviors of self-heating are observed and are discussed in this section.

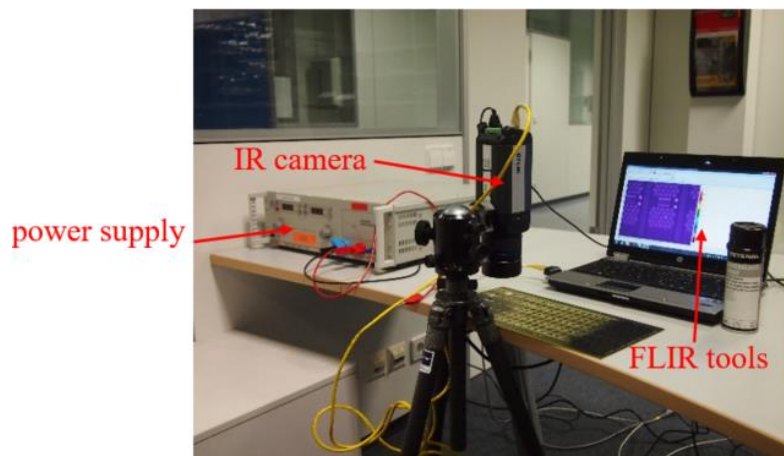


Fig. 3.12: Setup of the thermography measurement

(1) Self-heating of shunt A and A*

The self-heating of shunt A and A* is found to be asymmetric. The terminal of the shunt which is connected to the anode of the power supply, will undergo higher temperature than the cathode side. As displayed in Fig. 3.13, the anode side of the shunt A is exposed to around 20 °C higher than the other side. This observation is reversed if the current direction is switched.

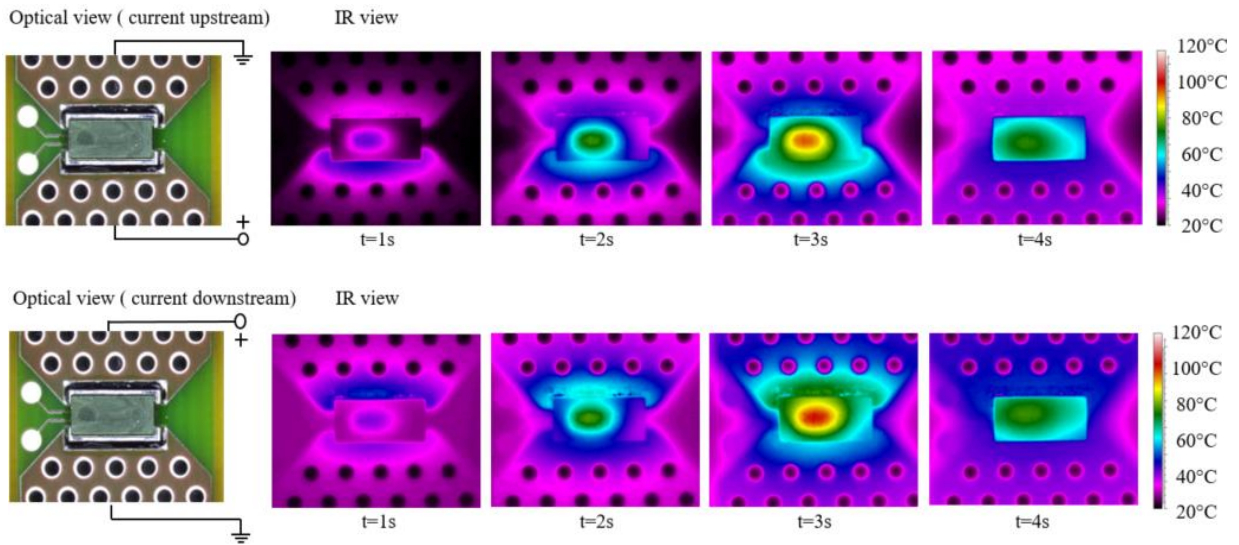


Fig. 3.13: Top view of the shunt A ($5\text{m}\Omega$) in optical and IR domains
(current 34A , pulse length 3s , RT)

Fig. 3.14 shows the thermography measurement of shunt A ($3\text{m}\Omega$) under another representative loading condition. Three probes P1, P2 and P3 are marked in the optical view. The temperature profiles of the three probes during the current load are plotted in Fig. 3.15. The same probes are also selected for shunt A* during the thermography measurement of the same loading condition. The recorded temperature profiles of shunt A* are plotted in dashed line in Fig. 3.15. No obvious difference is observed in the self-heating of the shunts with different plating material. Probe 3 exhibits the highest temperature in both current directions. Probe 1 and probe 2 show large thermal gradient despite of their symmetric location at the shunt. This observation agrees with the asymmetric self-heating detected in shunt A ($5\text{m}\Omega$).

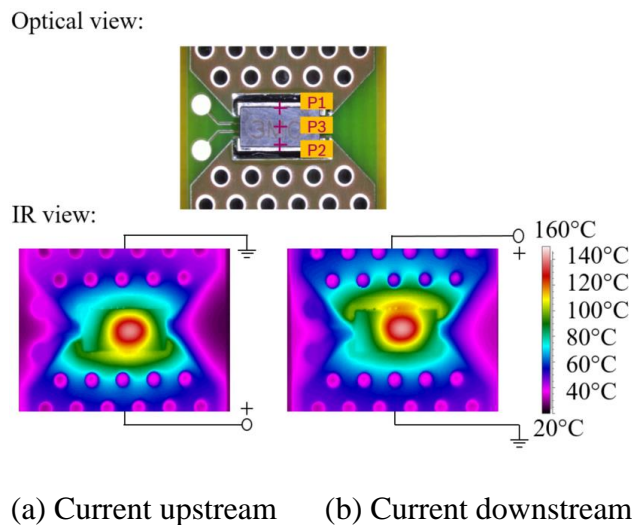


Fig. 3.14: Top view of the shunt A ($3\text{m}\Omega$, Ni/Sn plating) in optical and IR domains
(current 42A , pulse length 4s , ambient $25\text{ }^\circ\text{C}$)

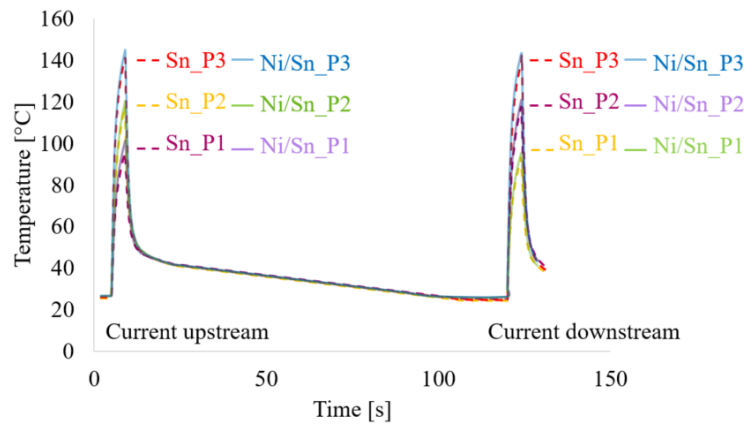


Fig. 3.15: Temperature profiles of three probes for both shunt A and shunt A*
 (current 42 A, pulse length 4 s, cooling time 110 s, ambient 25 °C)

(2) Self-heating of shunt B and C

On the other hand, shunt B yields symmetric self-heating under current load, as shown in Fig. 3.16. The highest temperature is located at the center of the shunt. The temperature is distributed symmetric at the two terminals and the thermal distribution remains the same when the current direction is reversed.

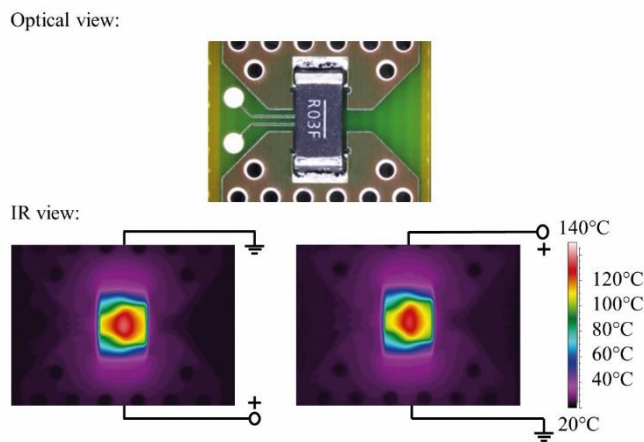


Fig. 3.16: Top view of the shunt B in optical and IR domains
 (current 6 A, pulse length 1 s, ambient 25 °C)

Shunt C exhibits the same self-heating behavior as shunt B, where the temperature is distributed symmetrically. The hotspot is located at the center of the resistive element, regardless of the current direction, as exhibited in Fig. 3.17.

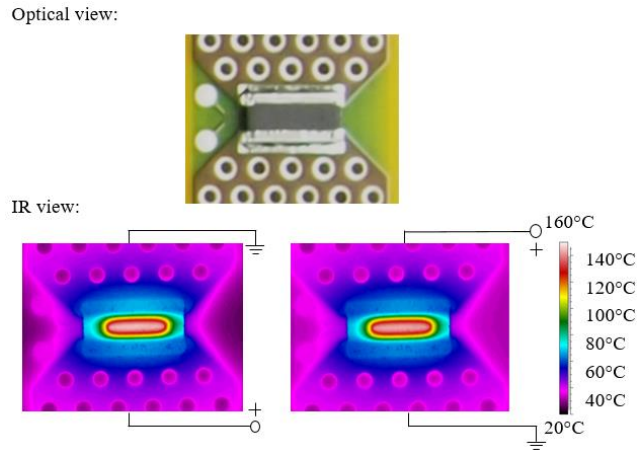


Fig. 3.17: Top view of the shunt C in optical and IR domains
(current 35 A, pulse length 4 s, ambient 25 °C)

3.3.2 Peltier effect

The explanation for the different self-heating modes could be the thermoelectric effect. As displayed in the cross-sectional pictures in Fig. 3.18, a clear interface is detected between the resistive element of shunt A and the copper terminals. Heat generation and loss occur when the current is flowing through the junction as a result of the Peltier effect [64]. Chukwu [121] has experimentally studied the thermoelectric effect and the Seebeck coefficient of Cu-CuNi thermocouples. This could explain the reversible asymmetric self-heating mode of the shunt A and A*. On the other hand, the resistive elements of shunt B and shunt C are connected to their terminals via a fused zone. Therefore, no extra heat generation or loss is detected when the current flows and symmetric self-heating mode is observed.

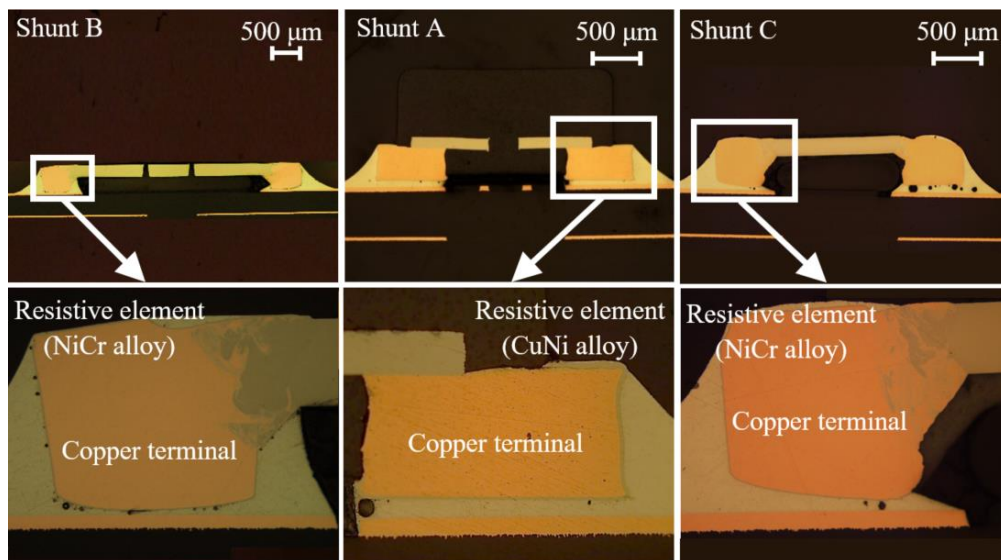


Fig. 3.18: Cross-sections of the shunts (without current stressing)

4 Failure analysis

The failure mode of the SAC solder joints subjected to high current pulses is investigated by performing light microscope, SEM/EDS, CT and EBSD analysis. The specimens are prepared for cross-sectioning after certain cycles of current stressing. The specimens are embedded in a mold with mixture of resin and hardener. The sample is later placed into a vacuum vessel to remove the bubbles in the mixing liquid. The liquid solidifies after one day and the embedded specimen can be taken out from the mold for grinding. The self-heating of the shunt results in a temperature gradient in the assembly. Therefore, the specimens have been grinded to different transverse planes for the investigation, as shown in Fig. 4.1. The cross-sectional direction is fixed so that the left side of the solder joint is connected to the anode side of the power supply. The specimens are grinded with sand papers from 800 grit size to 1200 and 2400 grit size, and are afterwards polished with a polishing disk from 9 μm via 3 μm to 1 μm . The polished samples are primarily investigated via light microscope.

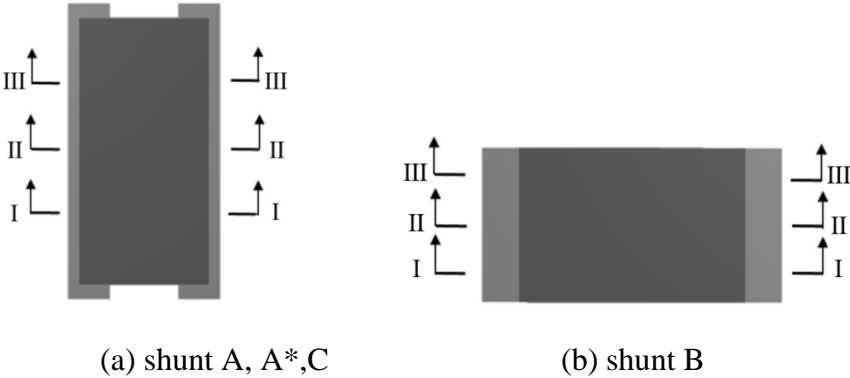


Fig. 4.1: Transverse planes for cross-sectioning of shunts

Apart from the analysis via light microscope, SEM analysis is carried out to study the microstructural evolution of the solder joint under current stressing. The samples have been processed with ion-etching to reduce the roughness of the sample surface, which enables to observe the grain structures. A layer of 35 μm gold is sputtered on the sample surface and high vacuum working mode is implemented so that high-quality SEM pictures can be obtained. This chapter discusses the failure modes of each tested shunt component via various material characterization techniques.

4.1 Failure mode of shunt A (5 mΩ)

4.1.1 Light microscope analysis

Fig. 4.2 displays the shunt A after the reflow process. Solder standoff and solder meniscus are formed to connect the shunt and the PCB. Some voids are detected in the solder joints due to the incomplete removal of the liquid and gaseous flux residues from the inside of the solder joint [122].

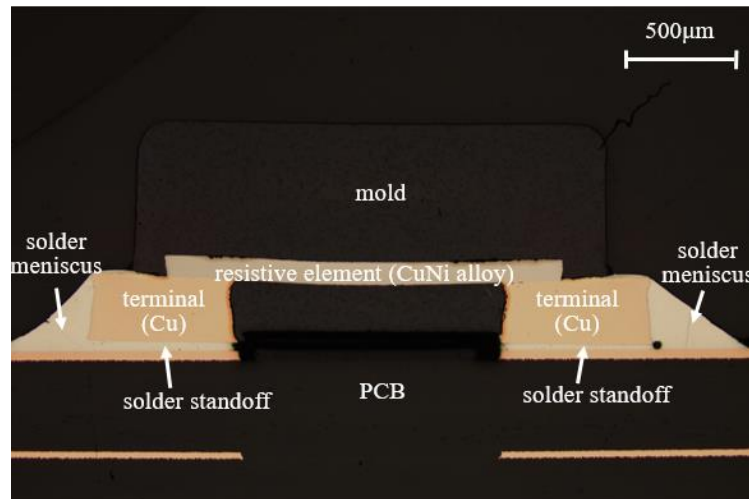


Fig. 4.2: Cross-section of shunt A after reflow (5 mΩ, II - II cutting plane)

After the power cycling test Nr. 7 which is defined in Table 3.5, the cross-sectional pictures of shunt A at different cutting planes are shown in Fig. 4.3. The main observations can be summarized as:

- (1) A crack is detected at the left side (anode side) of the solder joint.
- (2) The largest crack is observed to occur at the middle cutting plane (II - II).
- (3) There are two locations where the crack initiates and propagates, which are the edge of the solder standoff and the corner of solder meniscus.

Fig. 4.4 exhibits the cross-sectioning of shunt A under a higher loading condition (test Nr. 6). The above observations (1) and (2) are also detected in Fig. 4.4. At the plane II - II, the large crack has propagated completely through the left solder joint, leading to malfunction of the component.

The polarity effect of the failure mode of shunt A could be explained by its asymmetric self-heating behavior, which is specified in section 3.3. The left terminal of the shunt A undergoes higher thermal load since it is connected to the anode side of the power supply. Extra heat generation occurs at the junction of the Cu terminal and resistive element owing to the Peltier effect. The

accurate temperature distribution in the assembly under current loads will be characterized by thermography measurement and with the help of simulation.

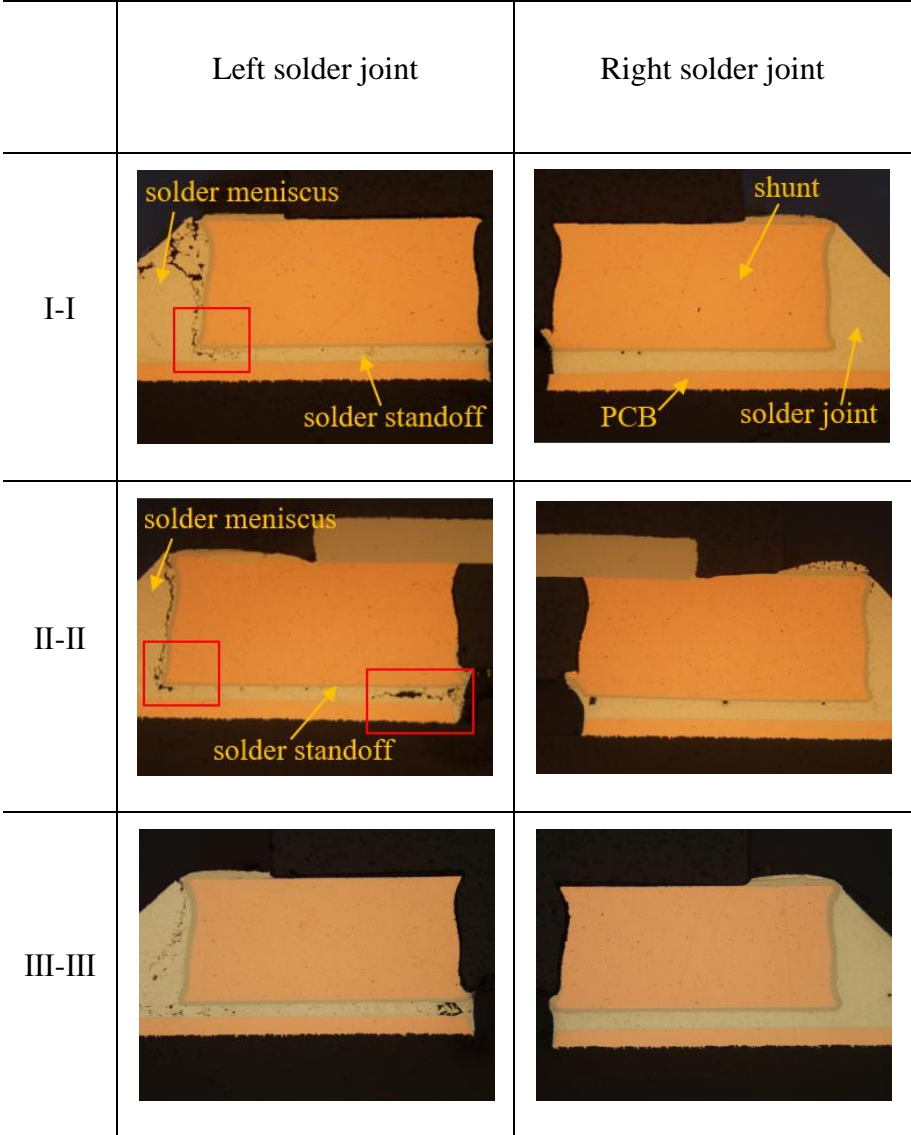


Fig. 4.3: Cross-section of shunt A (test Nr. 7: 5 mΩ, 26 A @3 s, 100 °C, 10000 PCs)

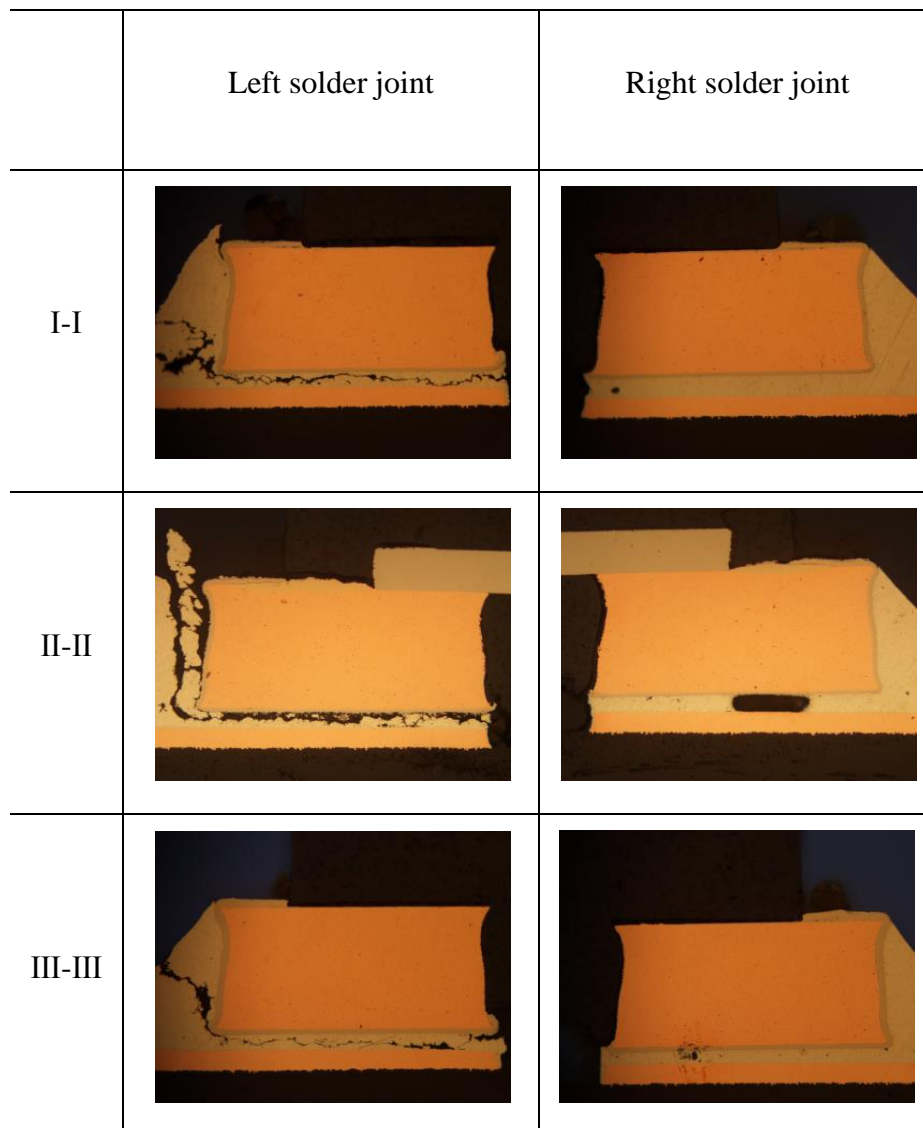


Fig. 4.4: Cross-section of shunt A (test Nr. 6: 5 m Ω , 34 A @3 s, 100 °C, 10000 PCs)

4.1.2 SEM analysis

The microstructural evolution of solder joints during the power cycling test is of great significance for the investigation since it exhibits the damage accumulation in the solder joint. Fig. 4.5 presents the same cutting plane I - I of shunt A at various power cycles. Micro-cracks are formed at the edge of the solder standoff and the corner of the solder meniscus, later propagate and join into macro-cracks. The regions of interest (ROI) are marked in Fig. 4.5 and are displayed in Fig. 4.6 with a higher magnification. It is observed that Ag₃Sn intermetallic precipitates are distributed among the globular Sn-rich phases after reflow. After 6000 cycles of current stressing, coarsening of the Ag₃Sn particles occurs in both sides of the solder joint, especially in larger extent and more widely spaced in the anode side, which decreases the resistance to dislocation motion [64].

Recrystallization is observed in the anode side of the solder and new grain boundaries are detected. Random large angle grain boundaries (LAGB) will be formed with cyclic thermo-mechanical stress, which can easily slide [3]. The coarsened Ag_3Sn particles tend to move towards the grain boundaries and the migration weakens the grain boundaries [86]. No obvious indication of recrystallization is observed in the cathode side of the solder joint after 9000 cycles, as a result of the lower temperature distribution.

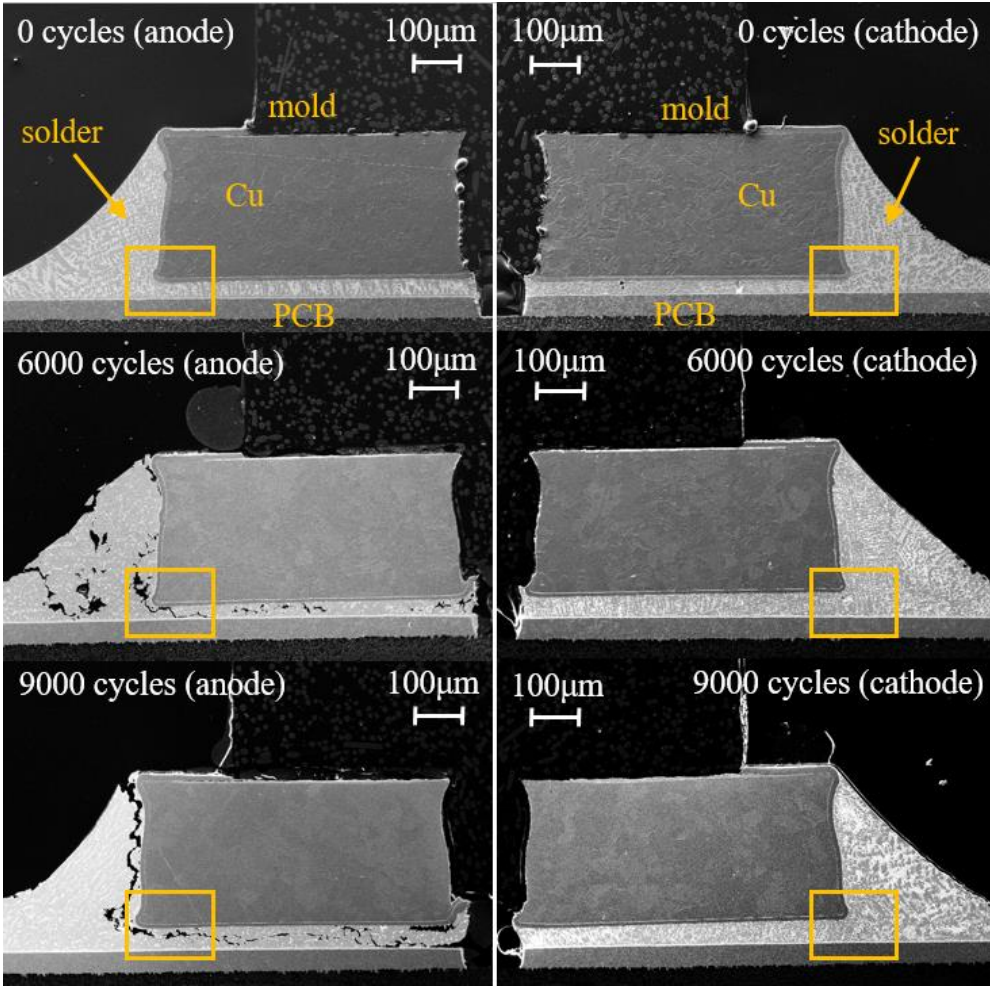


Fig. 4.5: SEM analysis of shunt A at different number of cycles
 (test Nr. 6: 5 mΩ, 34 A @3 s, 100° C, Mag= 50×)

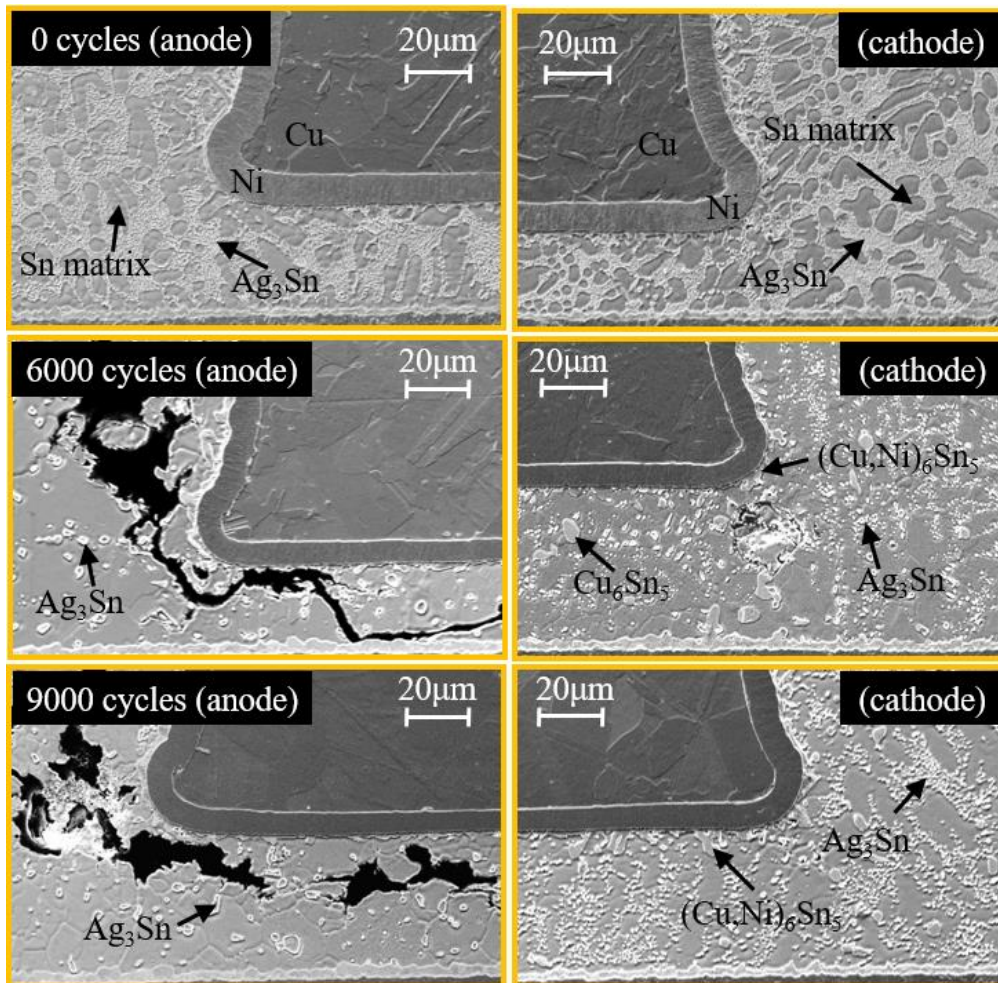


Fig. 4.6: Microstructural evolution of solder of shunt A (5 mΩ) at different stages of current stressing (Mag= 350×)

4.2 Failure mode of shunt A (3 mΩ)

4.2.1 Light microscope analysis

Similar studies have been conducted on other shunt components. As displayed in Fig. 4.7, the shunt A with 3 mΩ shows similar geometry as the shunt A with 5 mΩ. The dimensions of resistive element and of laser cut lead to the difference in their resistance. After 15000 power cycles (PCs), the failure mode of shunt A (3 mΩ) is analyzed and it is detected to be asymmetric as presented in Fig. 4.8. The damage takes place at the anode side of the solder joint and the largest crack is observed in middle cutting plane II - II. The cracks initiate from the solder standoff and the solder meniscus, which is agreement with the observations from shunt A of 5 mΩ.

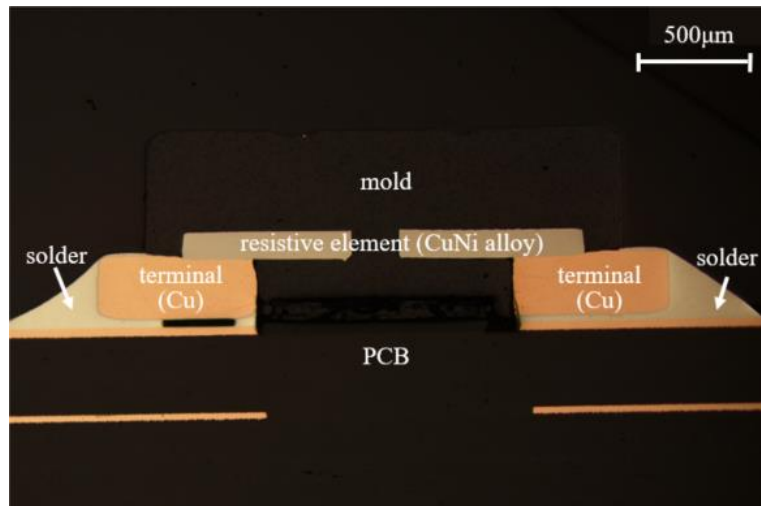


Fig. 4.7: Cross-section of shunt A after reflow (3 mΩ, II - II cutting plane)

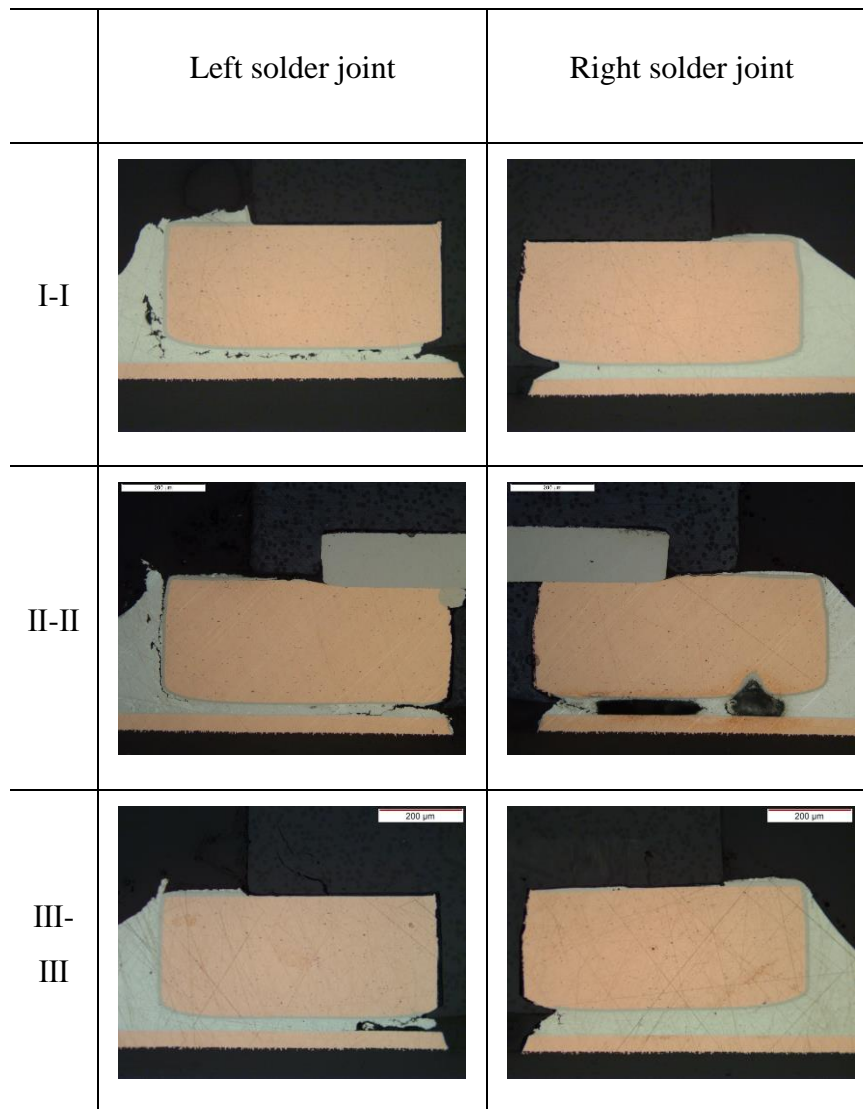


Fig. 4.8: Cross-section of shunt A (test Nr. 9: 3 mΩ, 45 A @2 s, 90 °C, 15000 PCs)

4.2.2 SEM analysis

SEM analysis is further performed on the middle cutting plane II - II of shunt A (3mΩ) to study the microstructural evolution of the solder under current stressing. Fig. 4.9 and Fig. 4.10 present the SEM pictures of the specimens after various testing time and the corner of the solder meniscus with a larger magnification. After reflow, the Sn-rich phases are surrounded by Ag₃Sn precipitates. Coarsening of Ag₃Sn precipitates takes place under current stressing. A crack is formed at the anode side of the solder meniscus after 15000 PCs. After more power cycles, the damage is enlarged and more grain boundaries are detected due to recrystallization. The cracks tend to grow along the grain boundaries. On the cathode side of the solder joint, only coarsening of Ag₃Sn precipitates is observed after 20000 PCs.

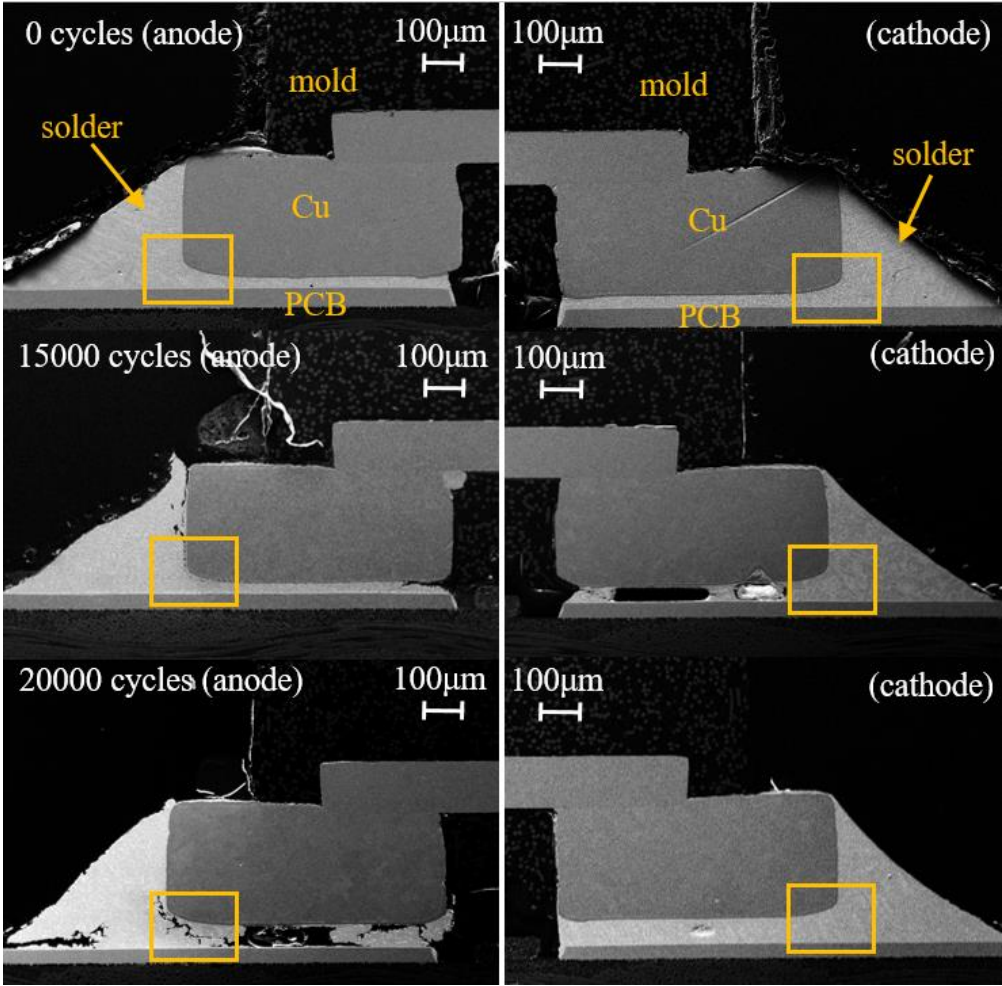


Fig. 4.9: SEM analysis of shunt A at different number of cycles

(test Nr. 9: 3 mΩ, 45 A @2 s, 90 °C, Mag= 40×)

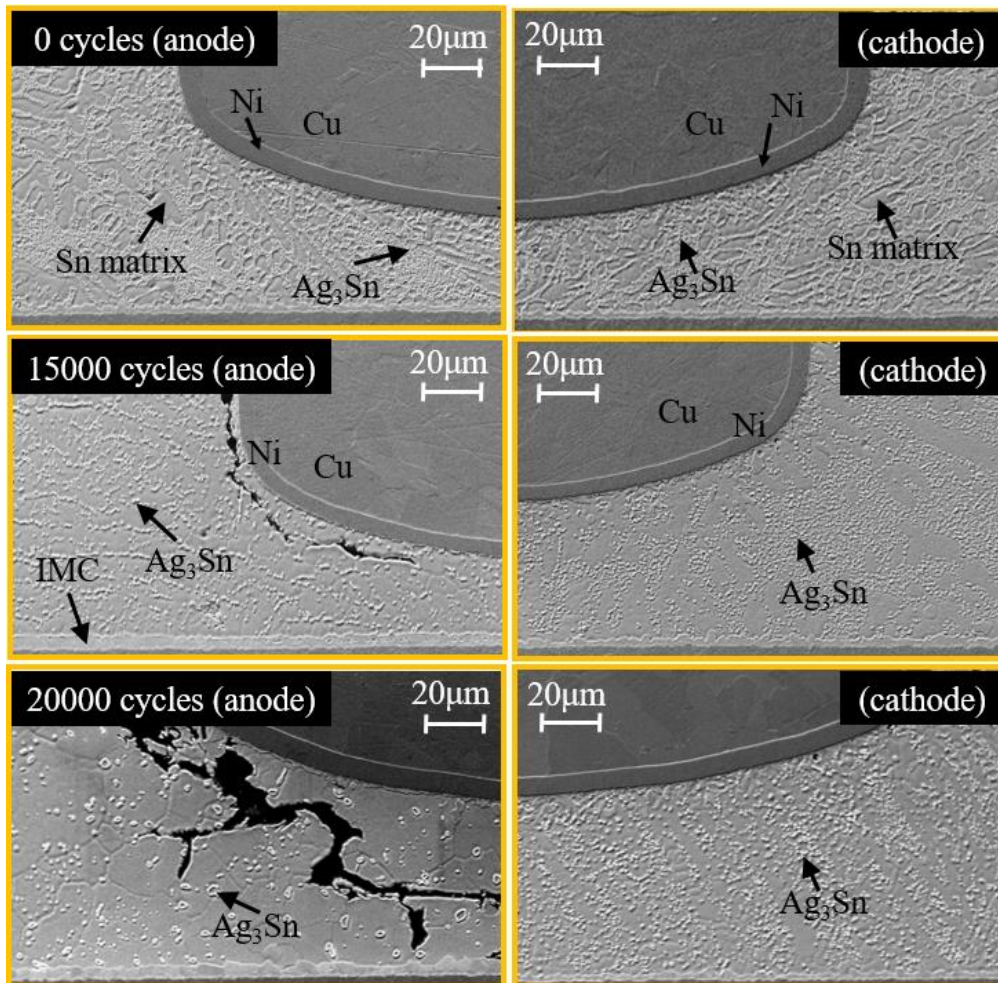


Fig. 4.10: Microstructural evolution of solder of shunt A (3 mΩ) at different stages of current stressing (Mag= 350×)

4.2.3 CT analysis

Cross-sectional imaging and SEM analysis are carried out on different specimens at various testing cycles. To monitor the degradation of solder of one representative shunt unit at different test stages, computer tomography (CT) has been performed for 3D imaging and analyzing the specimen non-destructively. The complete PCB assembly cannot be mounted for CT scan due to its large dimension and heavy weight. This could highly influence the resolution of the scan and interfere with the scan signal, especially during the rotation of the specimen. Therefore, the test layout of shunt A, as displayed in Fig. 4.11, has been modified to enable the removal of a shunt row during the power cycling test and restart the test after each CT scan. As shown in Fig. 4.12, the layout is adjusted so that power pins can be pressed into the PCB. Instead of being soldered on the PCB, the cables are attached with ring lug terminals and are connected to the power pins via screws. This allows for the intermediate removal of the shunt row for CT scans. The component for CT scan is highlighted in Fig. 4.12.

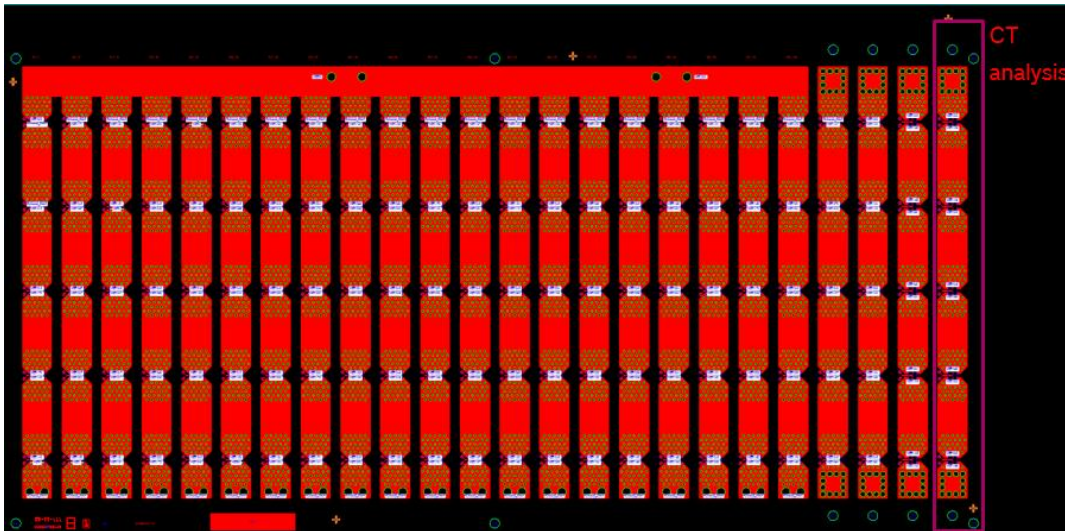


Fig. 4.11: Modified test layout for CT scan

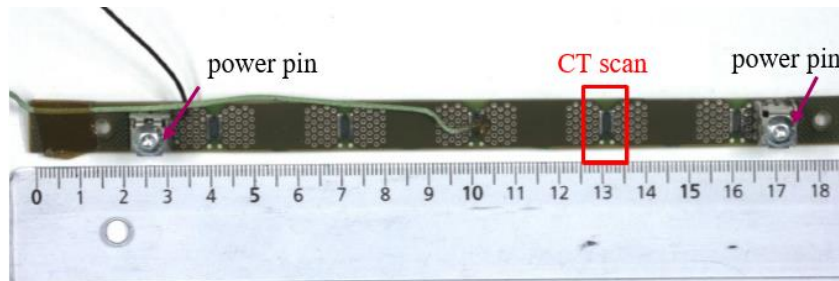


Fig. 4.12: Shunt unit for CT scan

Fig. 4.13 presents the equipment for CT scan, which is a GE VTOMEX CT scanner. The main parameters for the scans are listed in Table 4.1. The resolution is chosen to be $2.4 \mu\text{m}$ to obtain a scan with high quality. The higher the resolution is defined, the longer the scanning time will become. The chosen resolution is capable of capturing the initiation of the micro-cracks observed in the SEM analysis. The geometry of the scanned components is reconstructed, as shown in Fig. 4.14.



Fig. 4.13: Configuration of CT scanner

Table 4.1: Parameters for CT scan

Resolution	2.4 μm
Voltage	160 kV
Beam current	50 μA
Exposure time	500 ms

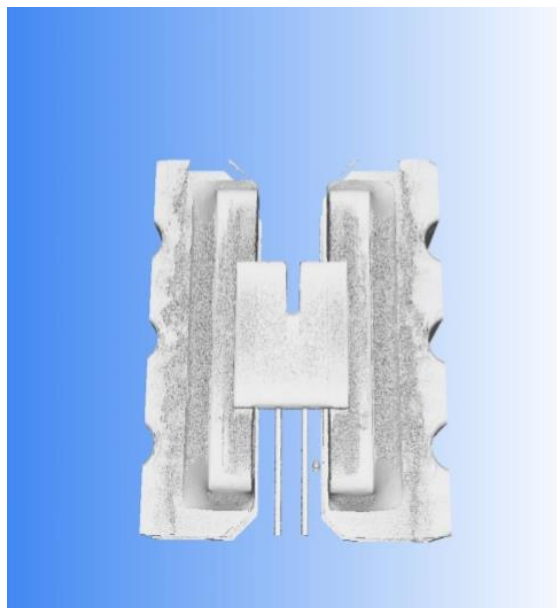
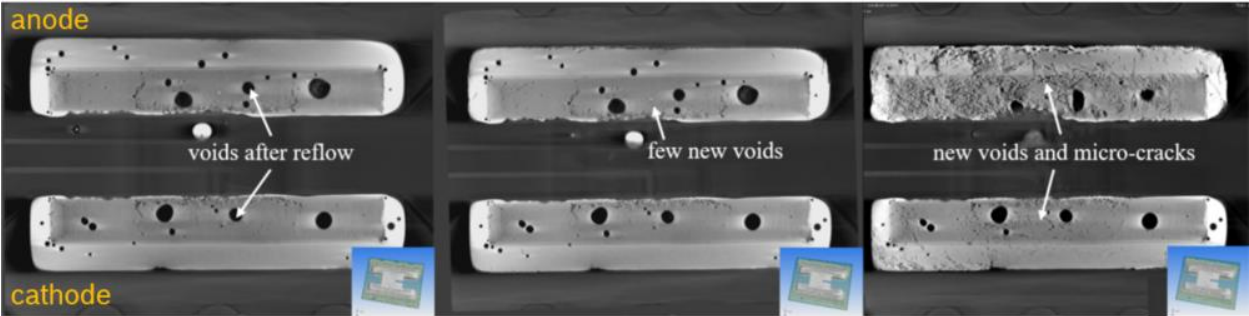


Fig. 4.14: 3D-rendering of scanned area (parts with higher density)

CT scanning has been performed on the shunt A ($3\text{ m}\Omega$) at three different stages, which are after reflow, after 10000 PCs and after 20000 PCs. The reconstruction of the three CT-scans is attached in the appendix. Slices of the three scans at the same scanning coordinates are presented in Fig. 4.15 to investigate the microstructural evolution of the solder joint due to current stressing. After reflow, some voids (area fraction 4.7% in the scanning plane) are detected in the solder joint. Few little voids (area fraction 4.8%) are formed in the solder after 10000 power cycles. After 20000 power cycles, many voids and micro-cracks (area fraction 27.6%) are observed, especially at the anode side of the solder joint. The three CT-scans are overlapped in Fig. 4.16 to compare the newly-formed voids and micro-cracks at each stage. The red line marks the new voids formed after 10000 PCs and the blue lines highlights the newly-formed voids and micro-cracks after 20000 PCs. It is noted that most of the damage occurs between 10000 PCs to 20000 PCs. Void formation also takes place at the other side of the solder joint where the temperature is lower. These newly formed voids are introduced by the current pulses and will degrade the strength of the solder material [123-124].



(a) Reflow (0 PC) (b) 10000 PCs (c) 20000 PCs

Fig. 4.15: CT scans of shunt A at different stressing stages (current downstream, test Nr. 9:
 $3\text{ m}\Omega$, $45\text{ A @ }2\text{s}$, $90\text{ }^\circ\text{C}$, $\text{Mag}=80\times$)

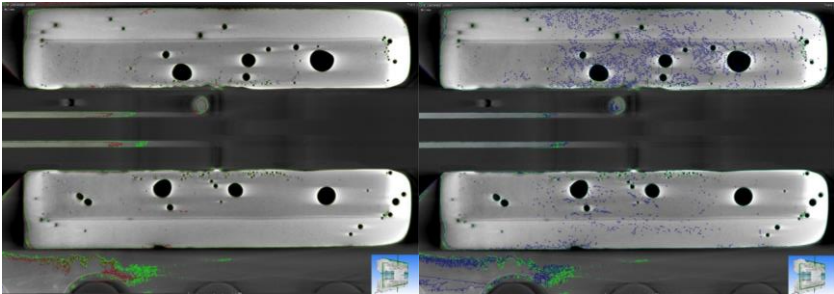


Fig. 4.16: Overlapping of the CT-scans

(Reflow: green line; 10000 PCs: red line; 20000 PCs: blue line)

4.3 Failure mode of shunt A* (3 mΩ)

4.3.1 Light microscope and SEM/ EDS analysis

Shunt A* with only Sn plating has been tested with the same loading condition as shunt A with Ni/Sn plating to investigate the interfacial reaction under active load and its influence on the reliability of components. Fig. 4.17 presents the cross-sectional picture of shunt A* after reflow. Apart from the removal of Ni plating outside the terminals, shunt A* yields the same geometry as shunt A and the same self-heating behavior as discussed in section 3.3.

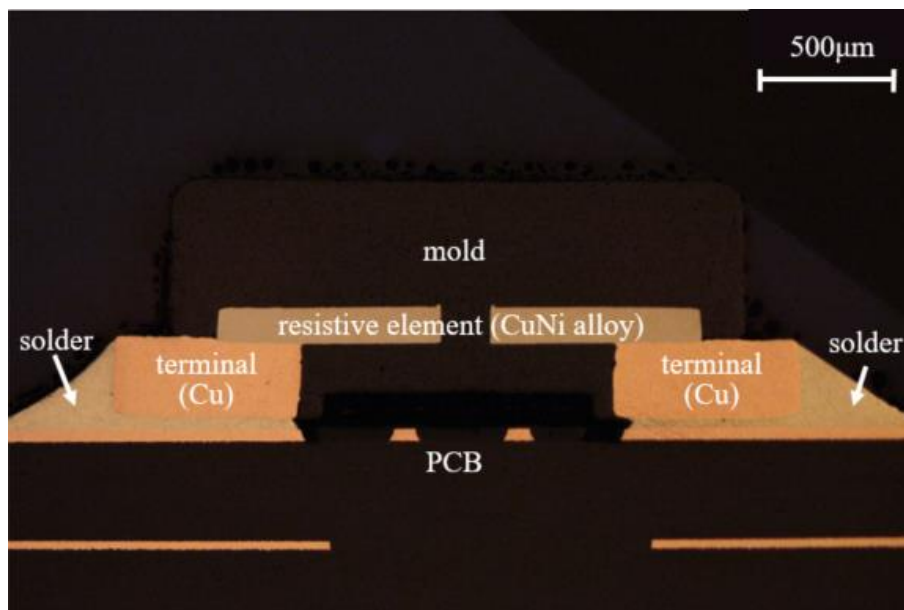


Fig. 4.17: Cross-section of shunt A* after reflow (3 mΩ, II - II cutting plane)

Before current stressing, the solder joint exhibits a quasi-single grain. After 5000 power cycles, many small grains are observed in the solder of shunt A* under polarized light, especially at the location of solder meniscus and solder standoff (Fig. 4.18). No obvious degradation is detected with light microscopy. The region of interest (ROI) A and ROI B where the new grain orientations are detected have been further studied with SEM. Fig. 4.19 displays the SEM analysis of ROI A and ROI B, respectively. At ROI A, many voids are noted in the solder joint and are located close to the corner of the solder meniscus. Near the region of void formation, many grain boundaries are detected and the newly formed grains might be the explanation for the different grain orientation observed with polarized light microscope.

At ROI B, recrystallization takes place and grain boundaries are observed. When the grains undergo stress, they tend to orientate, which could lead to the different grain orientation observed earlier. However, the crack is not growing along the grain boundaries of the solder joint, but along the interface between the bulk solder and the IMC layer at the PCB side.

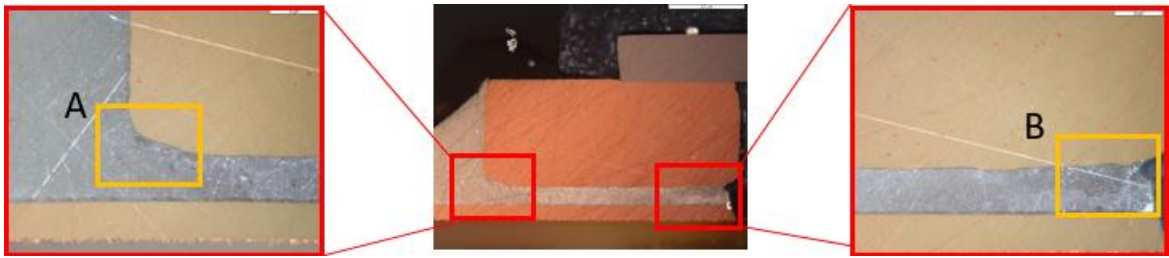


Fig. 4.18: Cross-section of shunt A* after 5000 power cycles under polarized light

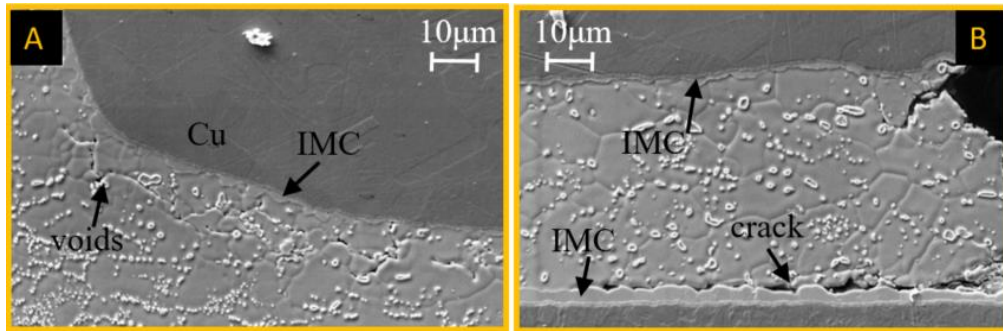


Fig. 4.19: SEM analysis of the ROI A and ROI B (Mag=600×)

Fig. 4.20 shows the cross-sections of shunt A* at 10000 and 150000 power cycles. Larger voids are detected at the corner of solder meniscus and the crack propagates to 100% through the solder joint after 15000 cycles of current stressing, which shows that shunt A* with only Sn plating is much more damaged than shunt A with Ni plating after 15000 power cycles.



(a) 10000 power cycles (PCs)



(b) 15000 PCs

Fig. 4.20: Cross-sectional analysis of the shunts A* after current pulses [124]

4.3.2 Interfacial reaction

The shunt A ($3\text{ m}\Omega$) and shunt A* ($3\text{ m}\Omega$) exhibit the same configuration and same self-heating behavior, yet different reliability. As observed from SEM analysis, void formation and micro-cracks are observed in shunt A* after 5000 power cycles with the loading conditions of 45 A and with the pulse duration of 2s (test Nr. 11) and a complete crack is formed after 15000 power cycles. On the other hand, shunt A with Ni/Sn plating shows significantly higher lifetime under the same loading conditions. Consequently, a detailed analysis on the interfacial reaction is of great significance to understand the impact of the plating and its influence on the reliability. Fig. 4.21 illustrates the regions of interest (ROI) to be investigated. Electrons flow downstream at the left solder joint, while upstream at the right side, leaving ROI1 and ROI4 as cathode locally, ROI2 and ROI3 as anode locally.

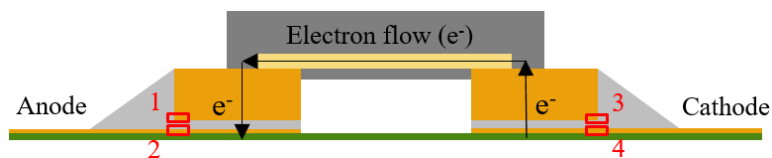


Fig. 4.21: Schematic diagram of the ROIs of shunt

ROI1: IMC1 on compound side

ROI2: IMC2 on PCB side

ROI3: IMC3 on compound side

ROI4: IMC4 on PCB side

After reflow, the solder joint yields the same microstructure at both terminal sides. The ROI1 and ROI2 of both shunt A and shunt A* are studied with EDS analysis. Fig. 4.22 exhibits the locations of elemental analysis and the spectra are plotted in Fig. 4.23 – Fig. 4.26.

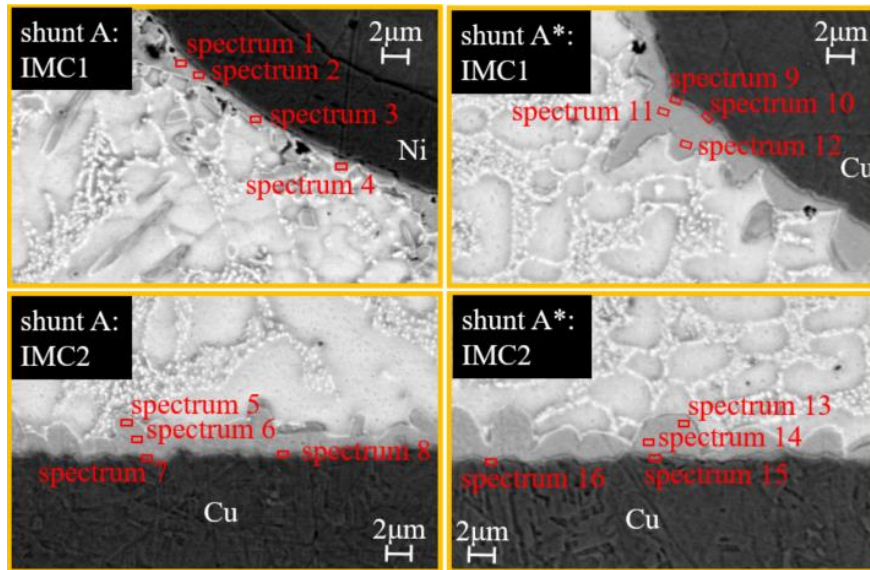


Fig. 4.22: Locations for EDS analysis of the shunt A and shunt A* (after reflow)

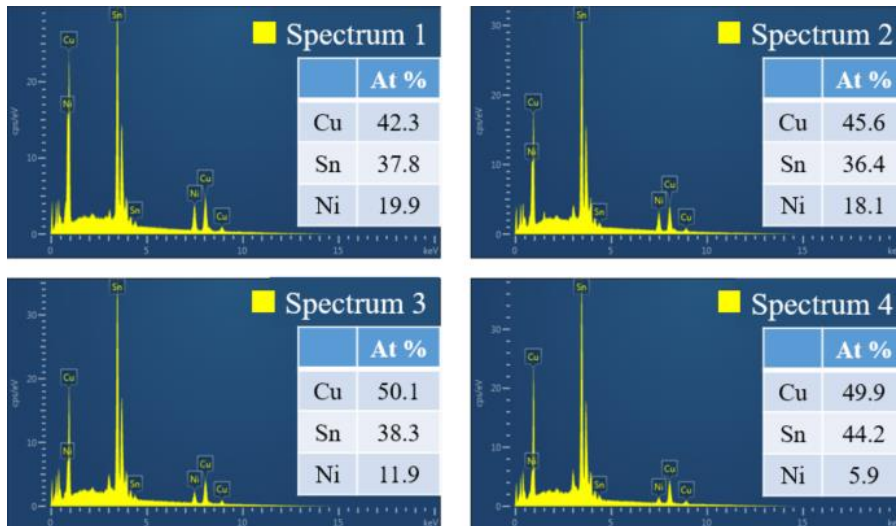


Fig. 4.23: EDS analysis of shunt A at ROI1 (IMC1)

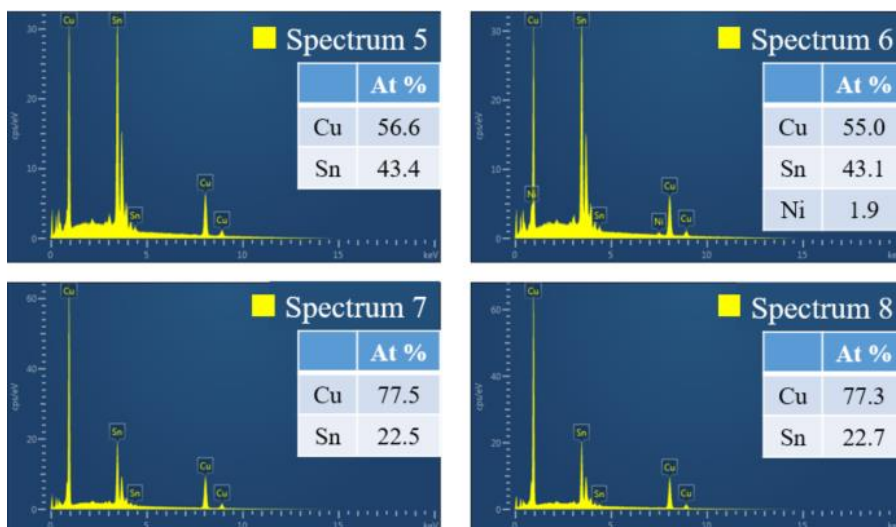


Fig. 4.24: EDS analysis of shunt A at ROI2 (IMC2)

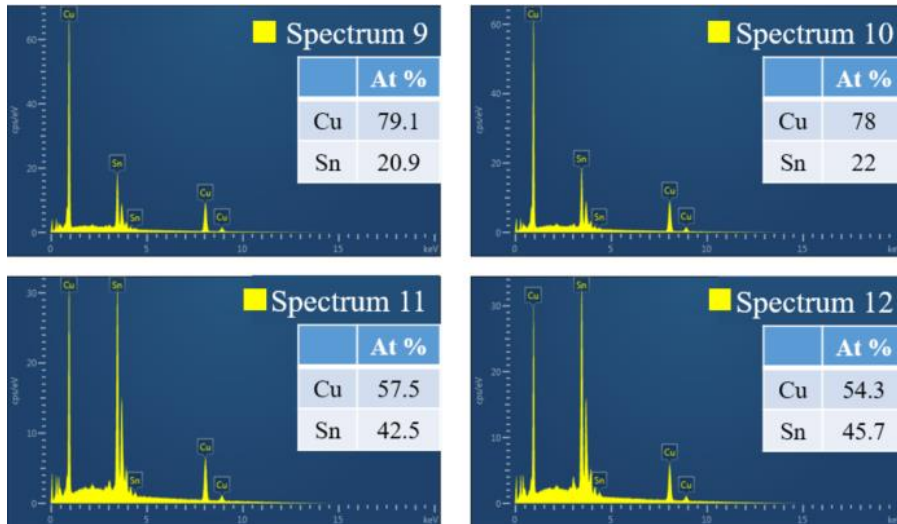


Fig. 4.25: EDS analysis of shunt A* at ROI1 (IMC1)

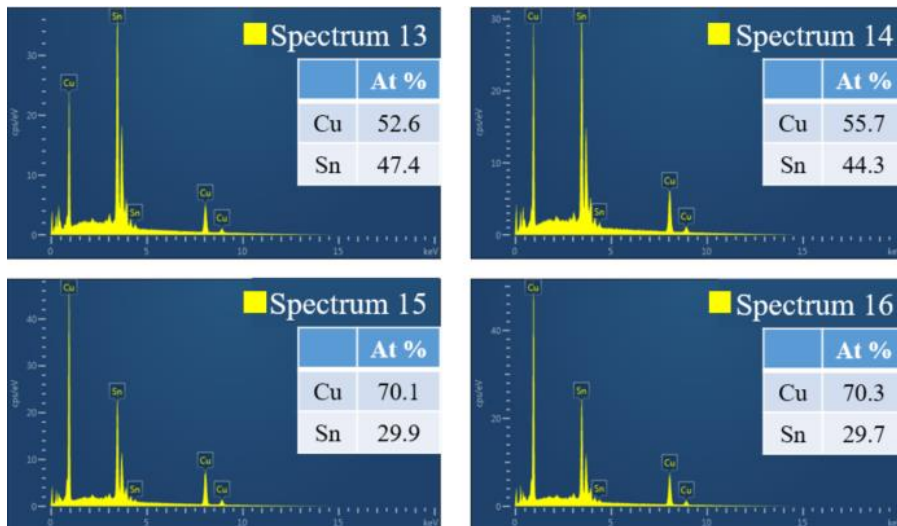


Fig. 4.26: EDS analysis of shunt A* at ROI2 (IMC2)

Based on the EDS analysis, the IMC1 formed on the component side of the shunt A is $(\text{Cu}, \text{Ni})_6\text{Sn}_5$ as displayed in spectrum 1,2,3 and 4. Ni diffuses from the plating into the IMC layer and the Ni content increases when the spectrum is taken closer to the plating. Despite of the slight difference of Ni content in the IMC, no secondary IMC phase is detected. At the PCB side of the shunt A, mainly two IMC phases are detected, which are Cu_6Sn_5 (spectrum 5) and Cu_3Sn (spectrum 7 and 8). Some Ni diffuses to the PCB side and forms $(\text{Cu}, \text{Ni})_6\text{Sn}_5$ with little Ni content, as the spectrum 6 shows.

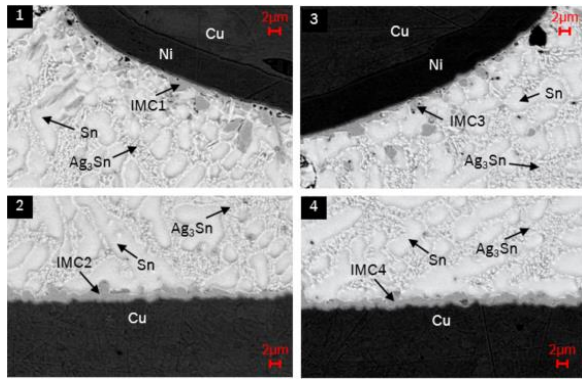
Without Ni plating, two IMC phases are observed at the component side of the shunt A* after reflow. The multiphase IMC is composed of ϵ -phase Cu_3Sn (spectrum 9, 10) and η -phase Cu_6Sn_5 (spectrum 11, 12). The thickness of the IMC1 at A* is also significantly higher than that of shunt A with the Ni plating. Both Cu_6Sn_5 (spectrum 13, 14) and Cu_3Sn (spectrum 15, 16) are detected in

the IMC at the PCB side of the shunt A*. A thin layer of Cu_3Sn is formed between the Cu_6Sn_5 compound and the Cu from the PCB. The thickness of the IMC formed on the PCB side of shunt A* (IMC2) is similar to that formed on the component side (IMC1).

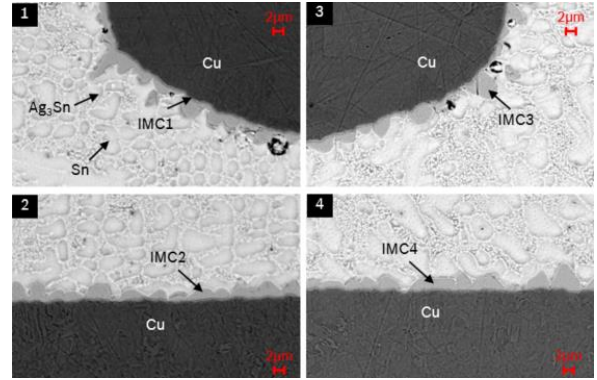
It can be concluded from the above observations that, the Ni plating prohibits the formation of Cu_3Sn phase. Fig. 4.27 and Fig. 4.28 illustrate the IMC formation of shunts A with Ni/Sn plating and shunts A* with only Sn plating at different testing stages, respectively. Since the self-heating of shunt A and shunt A* is asymmetric, the IMC growth at the anode side and at the cathode side are both analyzed.

As displayed in Fig. 4.27 for shunt A, Sn-rich structures are observed after reflow in both sides of the solder joints. The coarsening of Ag_3Sn precipitates occurs after 5000 PCs. After 10000 PCs, the thickness of IMC1 becomes smaller compared to IMC2 and IMC3. However, the temperature at ROI1 shows normally a higher value since it's closer to the hotspot of the component. With longer current stressing time, almost all the IMC1 is observed to be diffused away, as shown in Fig. 4.27 (d). Some hollow structures are detected at IMC2 layer, which has never been observed in IMC morphology after reflow. This indicates that the IMC1 is transported to the solder/IMC2 interface and becoming part of IMC2 layer, as Liu [107] also found out in his work. Voids and micro-cracks are formed after 15000 PCs, which corresponds well with the findings from CT scans where most of the damage is observed to occur between 10000 PCs to 20000 PCs.

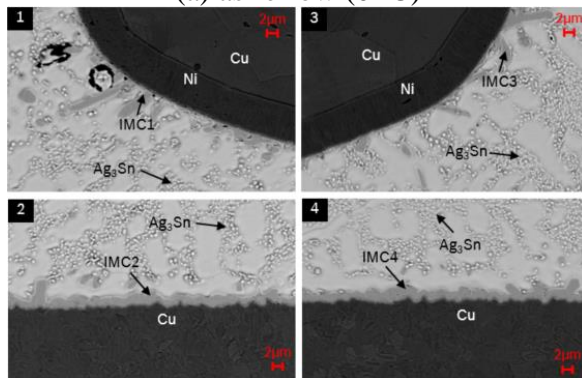
The polarity effect of IMC growth under current pulses is also detected in shunt A* with only Sn plating. A thicker IMC layer with scalloped shape is formed after reflow, which mainly composes of Cu_6Sn_5 and a very thin layer of Cu_3Sn . After 5000 PCs, the thickness of IMC1 seems to be reduced and shows a thinner layer than IMC2, IMC3 and IMC4, even though the local temperature at ROI1 yields the highest value among them. Besides, voids and micro-cracks are formed near the interface between IMC1 and solder. The voids and micro-cracks grow and propagate after more power cycles, which leads to earlier failure of the interconnect as shown in Fig. 4.28 (d). Therefore the difference in the interfacial reaction might explain the void formation and earlier failure of shunt A*, despite of the same heating behavior of the shunts.



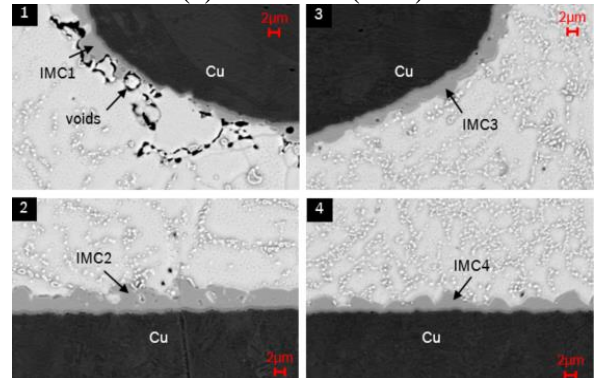
(a) as reflow (0PC)



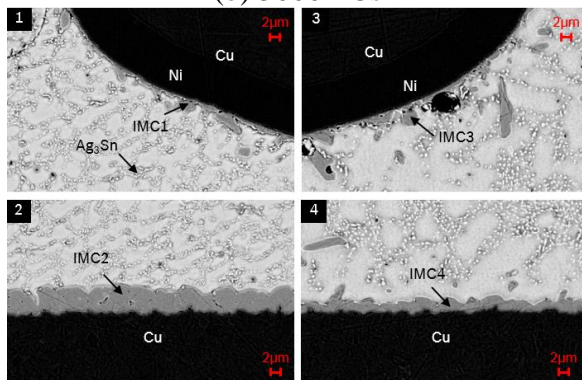
(a) as reflow (0PC)



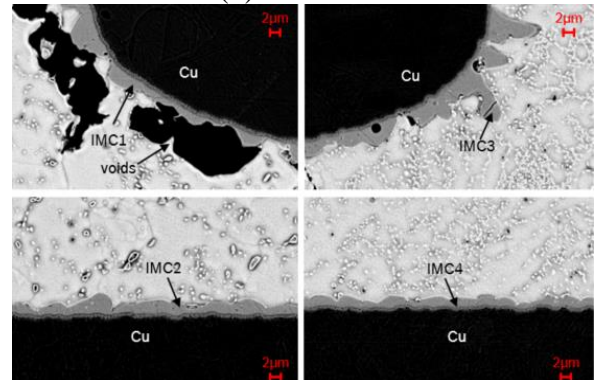
(b) 5000 PCs



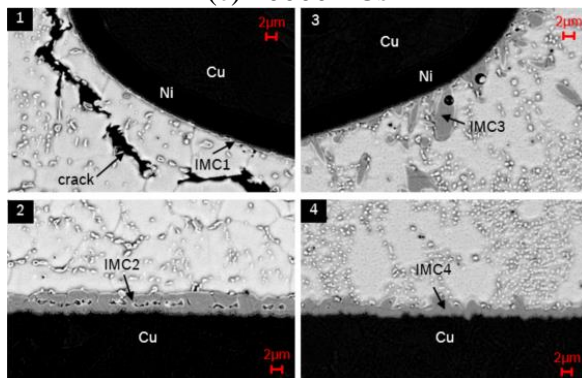
(b) 5000 PCs



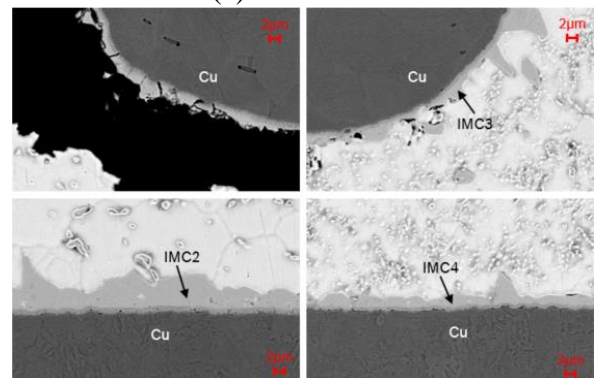
(c) 10000 PCs



(c) 10000 PCs



(d) 15000 PCs

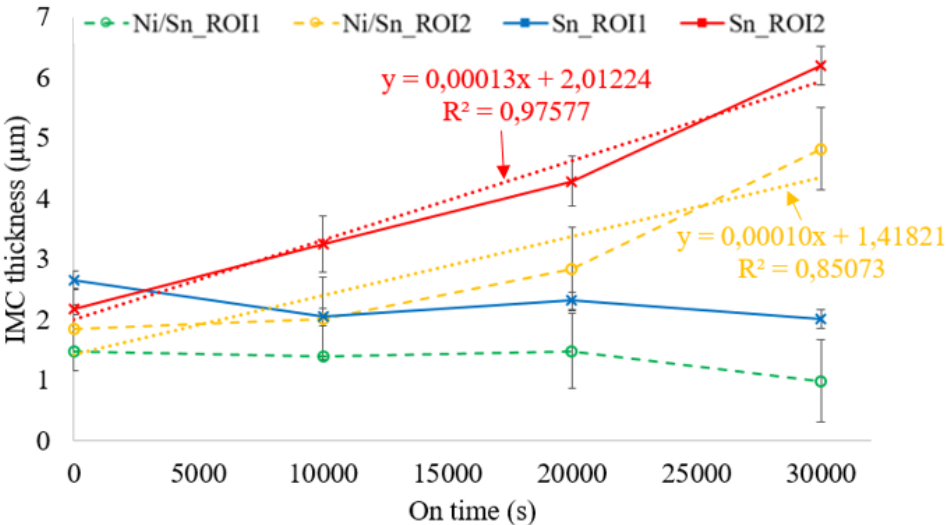


(d) 15000 PCs

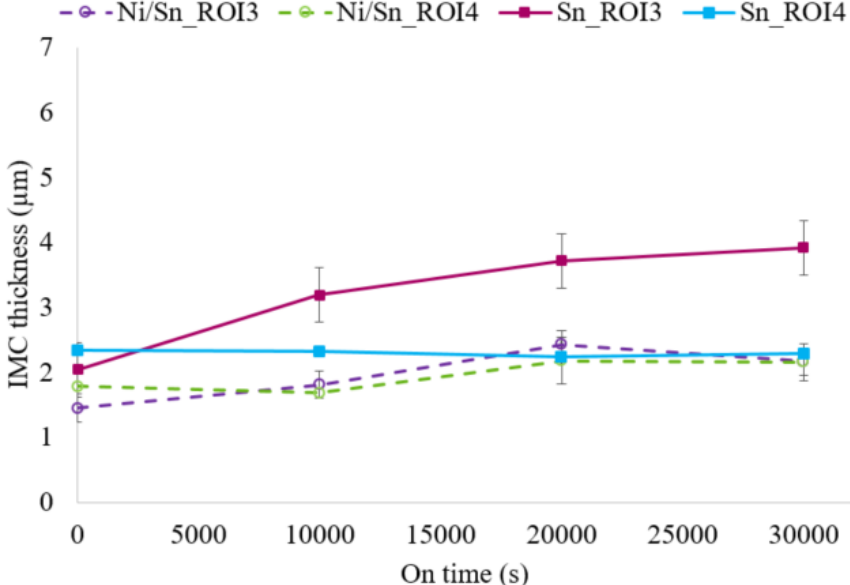
Fig. 4.27: IMC growth of shunt A with Ni/Sn plating at different cycles (Mag=1000×)

Fig. 4.28: IMC growth of shunt A* with only Sn plating at different cycles (Mag=1000×)

To further investigate the polarity effect on IMC growth owing to current stressing, five units of both shunts are taken out of the chamber at various number of power cycles to study the kinetics of IMC growth. The IMC thickness at different ROIs is calculated. The area of the measured IMC is measured by Image J software and the thickness is derived by dividing the measured area by the length of the interface. The IMC growth of solder joints with different plating is plotted with respect to testing time in Fig. 4.29. The ROI1 and ROI2 of both shunts undergo higher thermal load due to the asymmetric self-heating and the corresponding IMC growth is plotted in Fig. 4.29 (a). The IMC growth of ROI3 and ROI4 of both shunts, where the local temperature is lower, is presented in Fig. 4.29 (b).



a) IMC growth in left solder joint (higher temperature)



(b) IMC growth in right solder joint (lower temperature)

Fig. 4.29: IMC growth of the shunts A and A*

For both shunts with and without Ni plating, the IMC growth at ROI2 yields a linear correlation with respect to stressing time, as shown in the dotted fitting line and the fitting equations. T-test is conducted to assess the difference of the IMC growth of shunt A and shunt A*, as illustrated in Table 4.2. It can be observed from the P value that the IMC thickness at ROI2 of both shunts show insignificant difference after reflow. After current stressing at 5000 PCs, 10000 PCs and 15000 PCs, the IMC thickness at ROI2 of both shunts yield significant difference. This indicates that the different plating affects the IMC growth under current loads.

The IMC growth of shunts with only Sn plating at ROI3 displays a parabolic curve, which agrees with the typical IMC growth tendency under aging. The IMC thickness of shunts with Ni plating at ROI3 and ROI4 shows a slight increment with longer current stressing time, as a result of the lower temperature.

Table 4.2: T-test of the IMC growth

	0 PCs		5000 PCs		10000 PCs		15000 PCs	
	Sn_ ROI2	Ni/Sn_ ROI2	Sn_ ROI2	Ni/Sn_ ROI2	Sn_ ROI2	Ni/Sn_ ROI2	Sn_ ROI2	Ni/Sn_ ROI2
Mean	2.1735	1.8450	3.2541	2.0233	4.2906	2.8385	6.1995	4.8323
Variance	0.0076	0.1724	0.2535	0.0225	0.1888	1.4959	0.1355	0.8514
Observations	5	4	7	6	9	4	4	4
Pooled Variance	0.078251		0.148524		0.545318		0.493458	
Hypothesized Mean Difference	0		0		0		0	
df	7		11		11		6	
t Stat	1.750477		5.740568		3.272211		2.752566	
P(T<=t) two-tail	0.123507		0.00013		0.007436		0.033179	
t Critical two-tail	2.364624		2.200985		2.200985		2.446912	

The IMC thickness at ROI1 slightly decreases or remains unchanged for both shunts. The IMC growth tendencies at ROI1 and ROI2 are observed to be significantly different, despite that their local temperature is nearly the same. The polarity effect in the IMC growth can be explained by electromigration, where ROI1 and ROI2 serve as cathode and anode locally. Fig. 4.30 illuminates the kinetics of the interfacial reactions at ROI1 and ROI2.

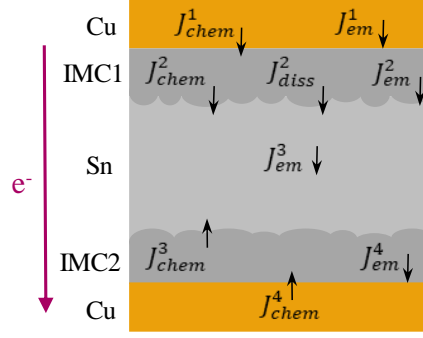


Fig. 4.30: Kinetics of IMC growth

$J_{chem}^1, J_{chem}^2, J_{chem}^3$ and J_{chem}^4 are the chemical diffusion of Cu in different phases. $J_{em}^1, J_{em}^2, J_{em}^3$ and J_{em}^4 characterize the electromigration of Cu at several interfaces and inside of the bulk solder. J_{diss}^2 is the dissolution of Cu from component terminal to solder. The IMC growth at ROI2 is marked as IMC2 and its thickness growth Δh_{IMC2} can be described as,

$$C_{Cu/Cu6Sn5} \frac{d\Delta h_{IMC2}}{dt} = J_{em}^3 + J_{chem}^4 - J_{em}^4 - J_{chem}^3 \quad (4.1)$$

The chemical diffusion of Cu from Copper pad to IMC2 and from IMC2 to solder can be calculated based on the concentration gradient of Cu in different phases, as shown in (4.2). C_{Cu} , $C_{Cu/Sn}$ and $C_{Cu/Cu6Sn5}$ are the Cu concentration in Cu, solder and IMC layer, respectively. The electromigration terms in (4.1) can be expressed by (4.3) and (4.4). Therefore, the thickness of IMC growth at ROI2 h_{IMC2} can be formulated as (4.5) [125].

$$J_{chem}^4 - J_{chem}^3 = D_{Cu/Cu6Sn5} \frac{C_{Cu} - C_{Cu/Sn}}{\Delta h_{IMC2} + h_0} \quad (4.2)$$

$$J_{em}^3 = C_{Cu/Sn} \frac{D_{Cu/Sn}}{kT} Z_{Cu/Sn}^* e \rho_{Sn} j \quad (4.3)$$

$$J_{em}^4 = C_{Cu/Cu6Sn5} \frac{D_{Cu/Cu6Sn5}}{kT} Z_{Cu/Cu6Sn5}^* e \rho_{Cu6Sn5} j \quad (4.4)$$

$$h_{IMC2} - \frac{M}{N} \ln |M + N h_{IMC2}| = (N_1 + N_2)t + C \quad (4.5)$$

$$M = D_{Cu/Cu6Sn5} \frac{C_{Cu} - C_{Cu/Sn}}{C_{Cu/Cu6Sn5}} \quad (4.6)$$

$$N_1 = \frac{C_{Cu/Sn} D_{Cu/Sn}}{kT C_{Cu/Cu6Sn5}} Z_{Cu/Sn}^* e \rho_{Sn} j \quad (4.7)$$

$$N_2 = - \frac{D_{Cu/Cu6Sn5}}{kT} Z_{Cu/Cu6Sn5}^* e \rho_{Cu6Sn5} j \quad (4.8)$$

$$D_{Cu/Sn} = D_1 \exp \left(- \frac{Q_1}{kT} \right) \quad (4.9)$$

$$D_{Cu/Cu6Sn5} = D_2 \exp \left(- \frac{Q_2}{kT} \right) \quad (4.10)$$

C is the fitting constant determined by the initial thickness of IMC h_0 . $D_{Cu/Sn}$ and $D_{Cu/Cu6Sn5}$ are the diffusion coefficient of Cu in solder and in IMC layer. D_1 and D_2 are diffusion coefficient at infinite temperature. Q_1 and Q_2 are the activation energy for diffusion. The other parameters for migration mechanisms have been illustrated in Table 2.3 with the additional index indicating the corresponding reaction phase.

It has been concluded that the growth rate of IMC2 is mainly governed by N1 [107]. The $C_{Cu/Sn}$ of shunts with only Sn plating is equivalent to nearly the solubility of Cu in Sn [125], noted as C_s . For shunts with Ni plating, the dissolution of IMC1 and the transport of the dissolve Cu will lead to the depletion of IMC1, as displayed in Fig. 4.24(d). With Ni as diffusion barrier, the concentration of Cu in Solder $C_{Cu/Sn}$ will decrease. Hence, less EM of Cu occurs in the solder and the growth of IMC2 is reduced with Ni plating. The reduced Cu concentration in the solder joint with Ni plating can be calculated from the slope of the IMC growth in Fig. 4.26 (a), which is $8.27E19 \text{ at.}\cdot\text{cm}^{-3}$.

The net flux of voids, Cu and Sn at the cathode can be described as (4.11) [126]. The self-diffusion of Sn is the same for both shunts with and without Ni plating. Therefore, the higher diffusion of Cu in shunts with only Sn plating leads to their enhanced void formation and earlier failure.

$$J_{voids} + J_{Cu} + J_{Sn} = 0 \quad (4.11)$$

4.3.3 EBSD analysis

The EM-induced void formation has been observed in solder joints subjected to high current loads via SEM analysis and CT scans. The diffusivity of Cu in Sn-rich solder and the self-diffusivity of Sn significantly depend on the grain orientation of β -Sn owing to its highly anisotropic properties [108-109]. Therefore, EBSD analysis is performed to investigate the correlation of the void formation and Sn grain orientations. The EBSD analysis is conducted in the SEM Supra 55VP (Zeiss) equipped with the EBSD-System from Oxford-Instruments (Aztec/ Channel 5). The analysis operates with the setup according to Table 4.3.

Table 4.3: Parameters for EBSD analysis

Step size	1.4 μm
Accelerating voltage	20 kV
Working distance	16.5 mm
Specimen tilt	70.0°
Camera exposure time	60 ms

Shunt A* specimens are selected to investigate the formation of the void-like damage at the corner of the solder meniscus. Fig. 4.31~Fig. 4.33 [124] present the SEM pictures of the specimens and the EBSD analysis at three testing stages. The inverse pole figure (IPF) of the crystal orientation of Sn along different directions are displayed. The large angle grain boundaries (LAGB) of Sn which exhibit a misorientation larger than 10° are marked as black lines and the corresponding crystal orientation and c-axis are specified.

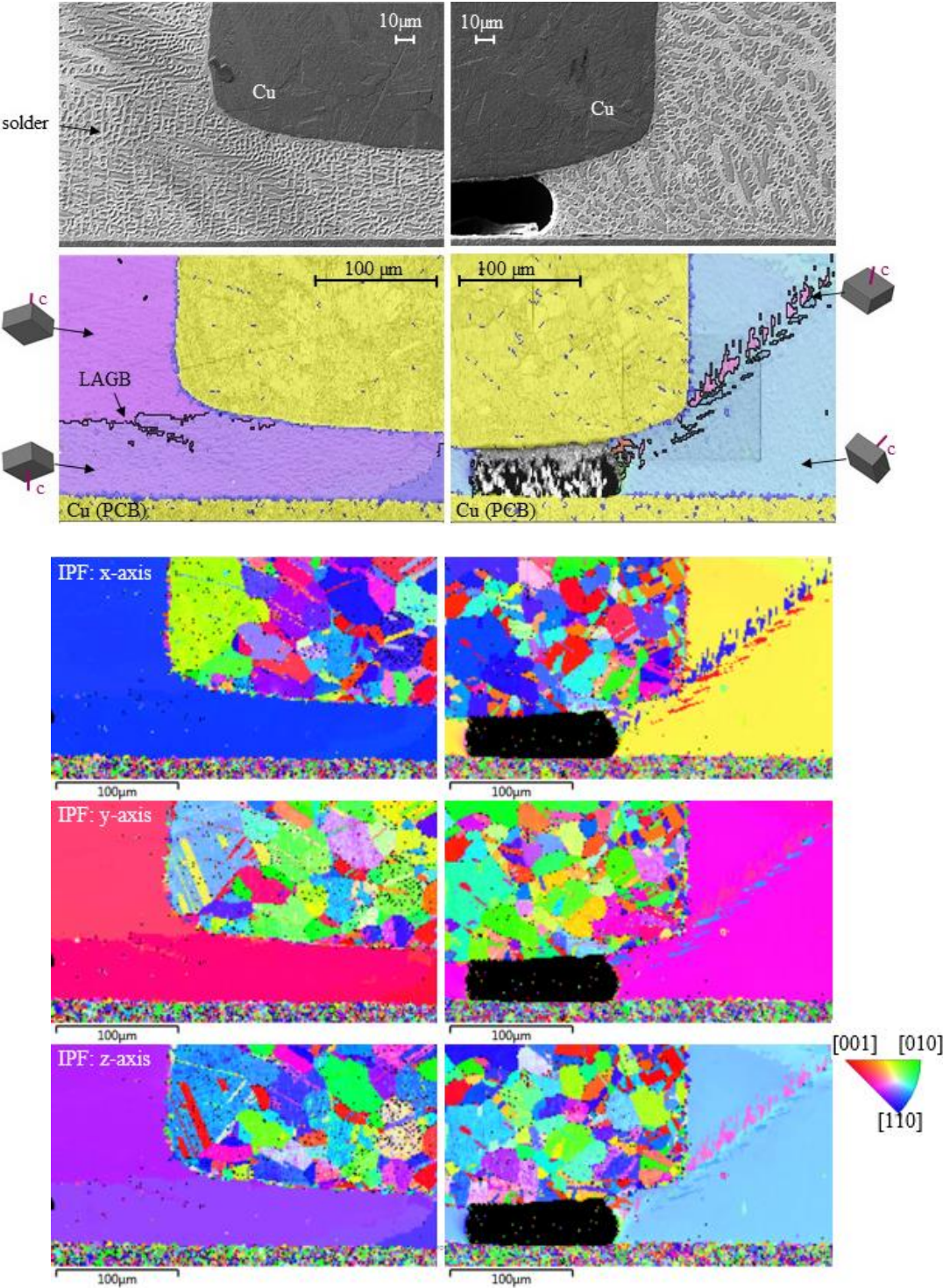


Fig. 4.31: SEM and EBSD analysis of solder joints of shunt A* as reflow [124]

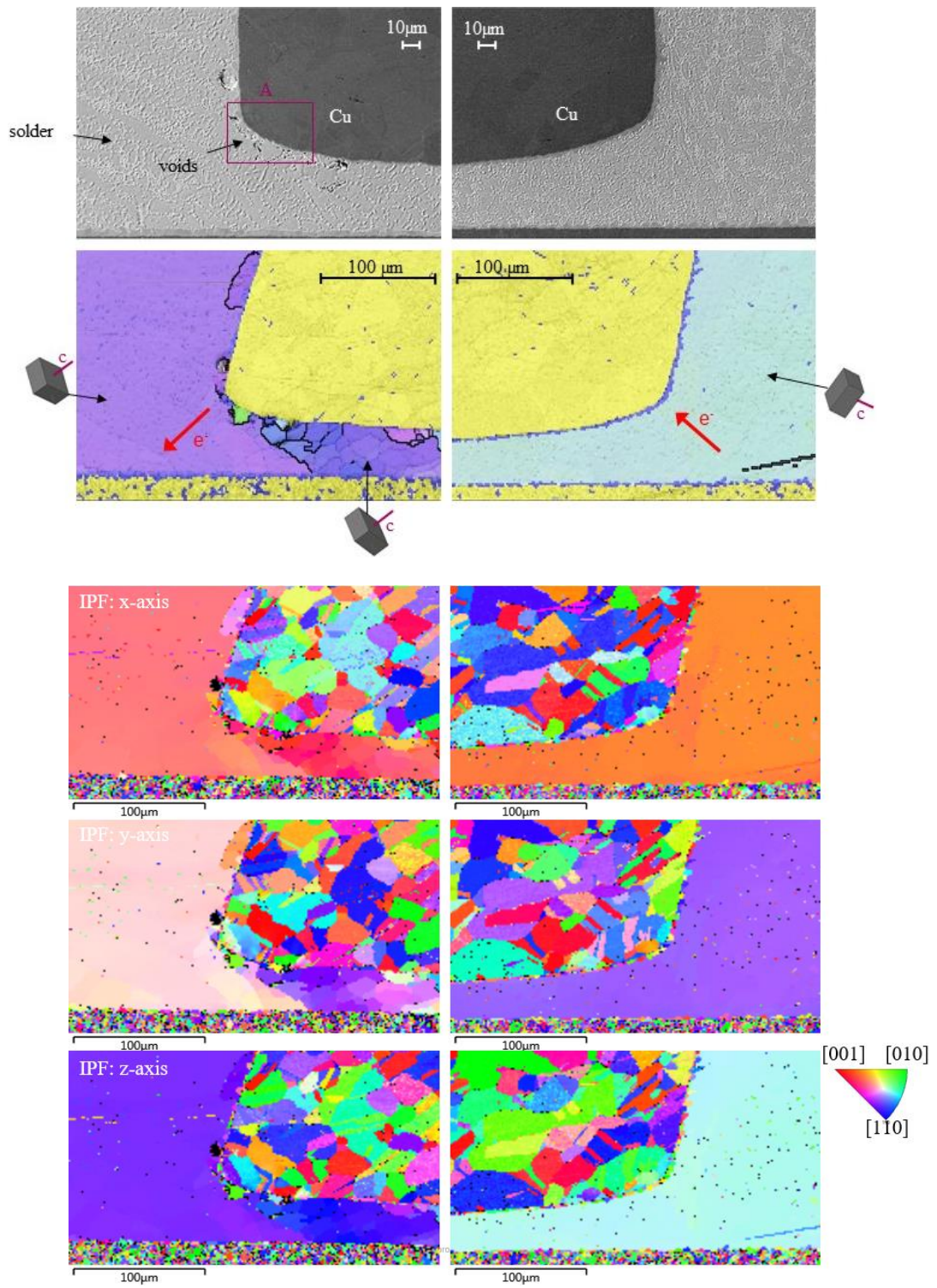


Fig. 4.32: SEM and EBSD analysis of solder joints of shunt A* after 5000 PCs [124]

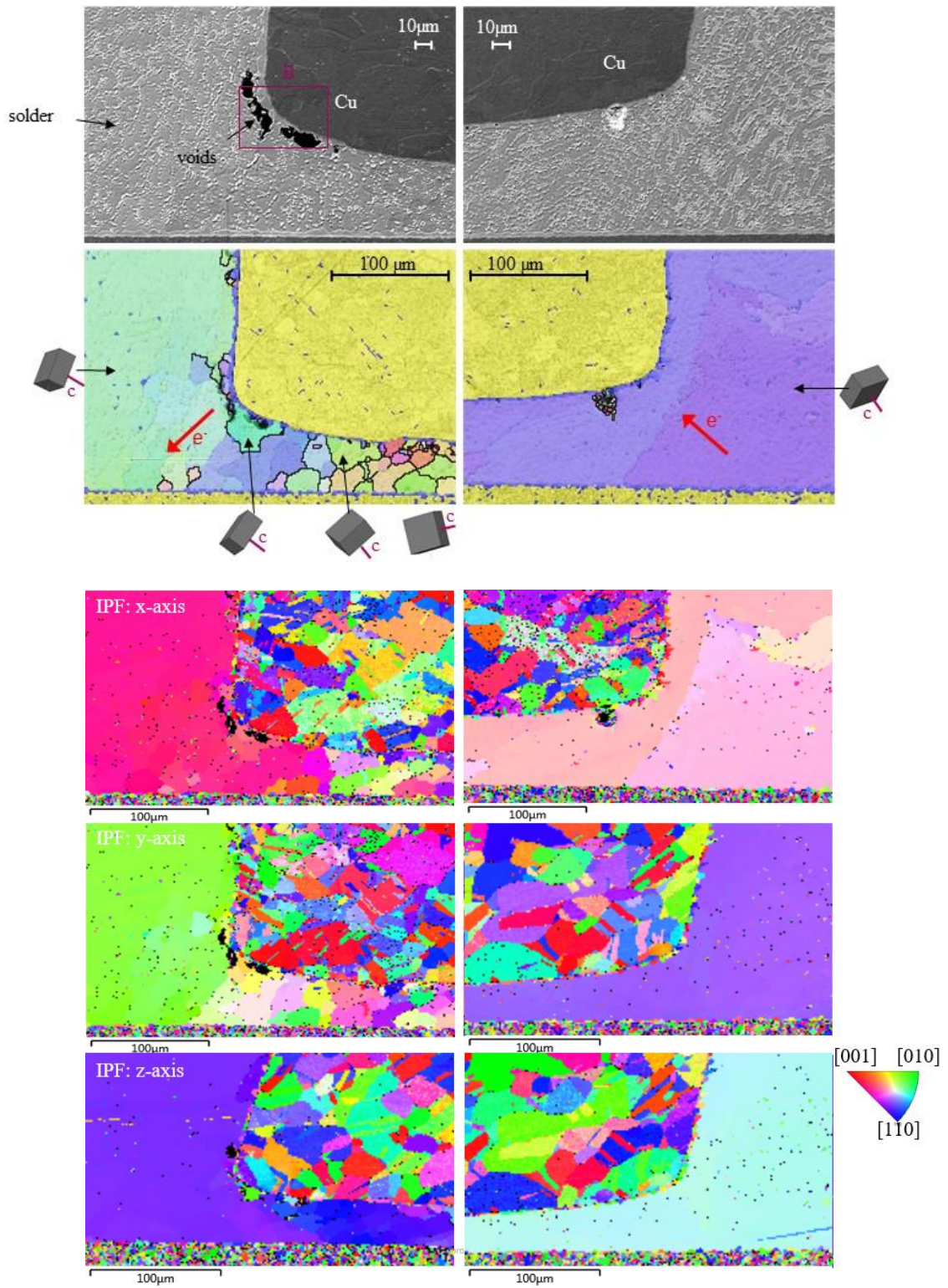


Fig. 4.33: SEM and EBSD analysis of solder joints of shunt A* after 10000 PCs [124]

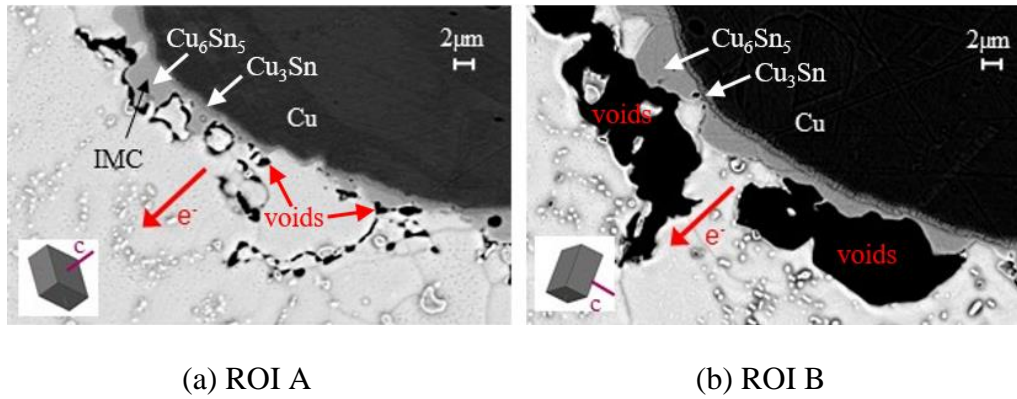


Fig. 4.34: The correlation of the void formation and Sn grain orientations (10000 PCs) [124]

As shown in Fig. 4.31, only two large Sn grains are detected at the left solder joint after reflow. At the right solder joint, two twin boundaries might have grown inside the solder, displaying a misorientation of about 60° with respect to the solder matrix. Despite the large pore in the right solder joint, no significant difference is observed in the microstructure of solder joints at both sides. After 5000 PCs, voids and micro-cracks are initiating at the corner of the left solder meniscus, as displayed in Fig. 4.32. Recrystallization takes place and small grains are formed predominantly at the solder standoff. As displayed in the IPF plots, most of the small grains share similar orientation and form a cluster with a common LAGB with respect to the neighboring solder matrix. More LAGBs are discovered after the current stressing. The right solder joint is comprised of a quasi-single grain of Sn and no additional LAGB is detected after 5000 PCs. After 10000 PCs, larger voids are detected at the corner of the left solder meniscus, as exhibited in Fig. 4.33. The misorientation of the grains at the standoff is enhanced, hence more LAGBs are formed at the standoff. However, the right solder joint exhibits a quasi-single grain of Sn similar to what is observed earlier.

The polarity of microstructural evolution in both sides of the solder joints can be explained by the higher temperature in the left solder joint due to asymmetric self-heating. Recrystallization occurs under current loads and the new grains orientate under cyclic thermo-mechanical stress, forming LAGBs. Thermo-mechanical fatigue cracks tend to initiate and propagate at the recrystallized region with LAGBs [17]. However, the void-like damage is located at the corner of the solder meniscus, instead of the standoff where LAGBs are detected. Consequently, the degradation mechanism for the observed voids and micro-cracks is likely to be EM rather than recrystallization-assisted crack nucleation [124]. The correlation of the void formation and Sn grain orientations is displayed in Fig. 4.34. Fig. 4.34 (a) presents the voids and micro-cracks formed in ROI A with larger magnification. The damage is located at the IMC/solder interface. The void-like damage in ROI B, as shown in Fig. 4.34 (b), is locating in the solder and close to

the interface. This observation could be explained by the orientation of Sn grains at the corner of meniscus with respect to the electron direction. The c-axis of β -Sn is almost parallel to the electron direction in ROI A, hence the Cu is the dominant diffusant in EM. A thinner IMC layer is observed and voids are formed at the interface due to the depletion of Cu. At ROI B, the c-axis of β -Sn is approximately perpendicular to the electron direction and the enhanced Sn self-diffusion leads to depletion of Sn [124].

4.4 Failure mode of shunt B

Fig. 4.35 displays the cross-sectional picture of shunt B after reflow. Many voids are detected in the solder joint due to the incomplete removal of flux residues. Light microscope imaging and SEM analysis are carried out on the test units after current loads. Fig. 4.36 exhibits the failure analysis of two representative specimens after 20000 PCs at II - II cutting plane, where the most severe damage occurs. The cross-sectional pictures in Fig. 4.36 show that cracks can initiate and grow in the left solder joint (unit 1) or in the right solder joint (unit 2). No polarity effect is observed in the failure mode, which differs from the findings from shunt A and A*.

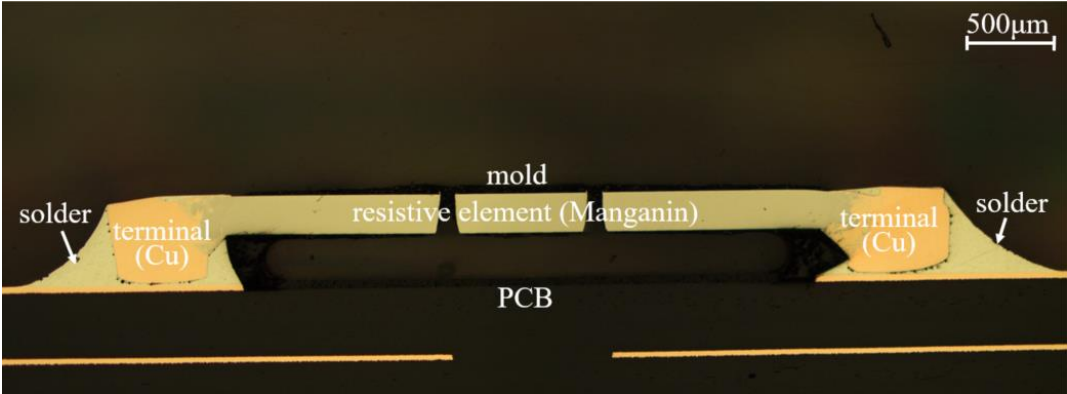


Fig. 4.35: Cross-section of shunt B after reflow (30 mΩ, II - II cutting plane)

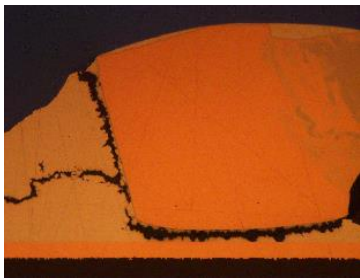
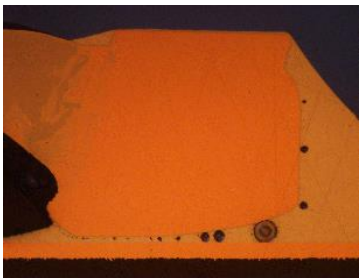
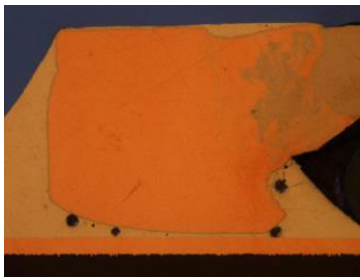
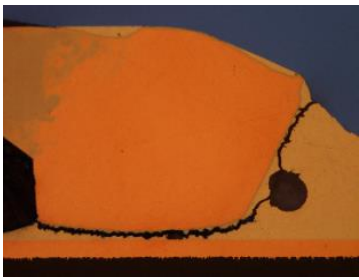
Shunt unit	Left solder joint	Right solder joint
1		
2		

Fig. 4.36: Cross-sectioning of shunt B (test Nr. 13: 30 mΩ, 10 A @ 1 s, 90 °C, 20000 PCs)

Fig. 4.37 and Fig. 4.38 present the microstructural evolution of the solder joint of shunt B before current stressing and after 20000 power cycles. No obvious difference in microstructure has been observed between the left and right solder joint, as a result of the symmetric self-heating of shunt B. In the representative shunt unit shown in Fig. 4.37, a crack is formed across the bulk solder joint on the right side (cathode side), with micro-cracks initiating from the solder standoff on the left side (anode side). After 20000 power cycles, coarsening of Ag_3Sn precipitates is detected and no large microstructural evolution has been observed.

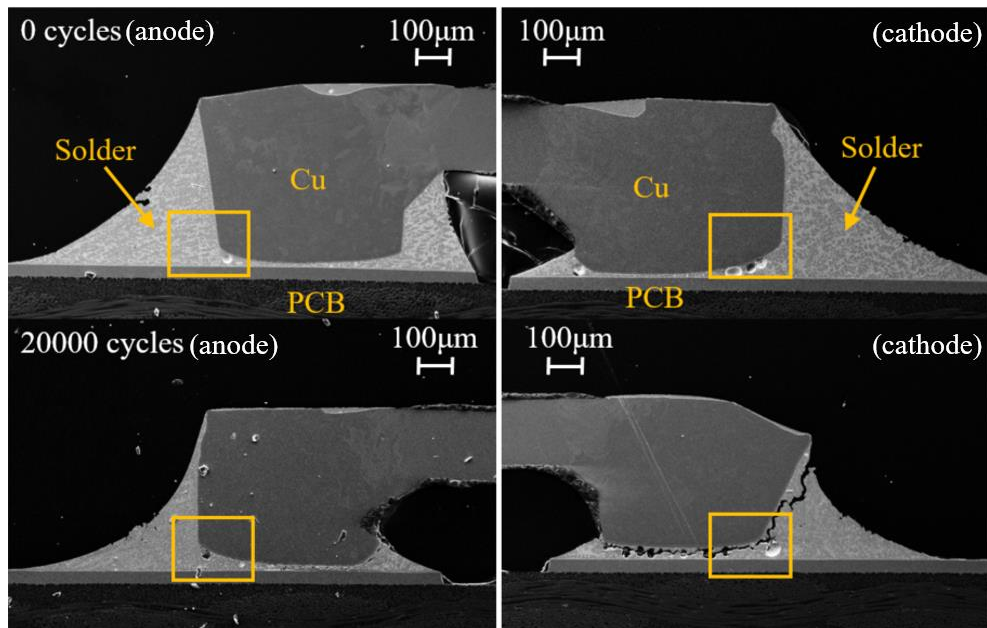


Fig. 4.37: SEM analysis of shunt B at different number of cycles

(test Nr. 13: 30 mΩ, 10 A @1 s, 90 °C, Mag= 40×)

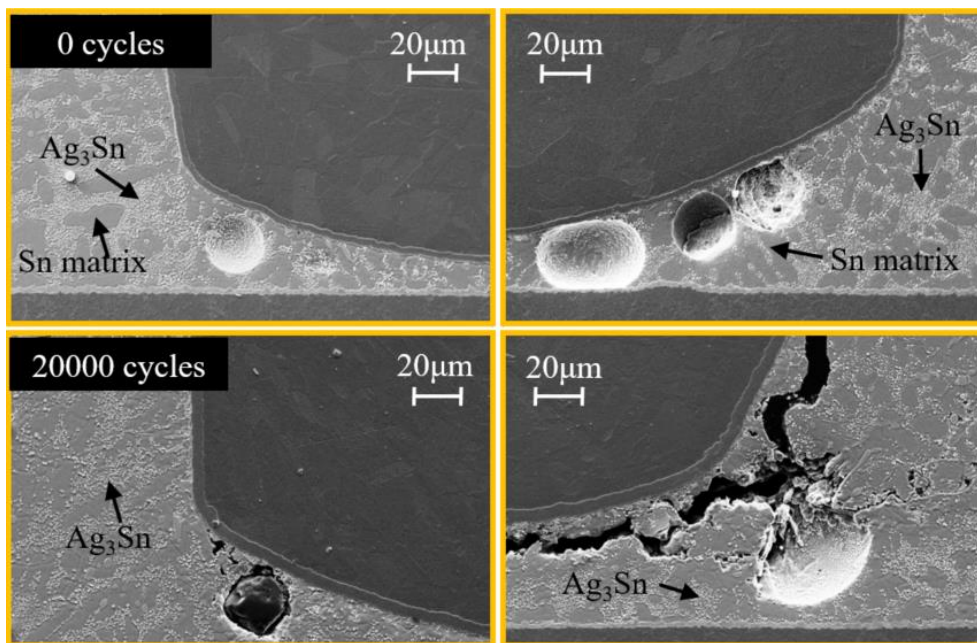


Fig. 4.38: Microstructural evolution of solder of shunt B at different stages of current stressing

(Mag= 250×)

4.5 Failure mode of shunt C

The cross-sectional pictures of shunt C (Fig. 4.39) show that the two terminals exhibit a slight difference in the geometry. The Cu terminal on one side is smaller and so is the thickness of the corresponding solder standoff. The Cu terminal on the other side is slightly larger and its corner shows a sharper curvature. The sharp corner might hinder the outgasing of solder flux and result

in large voids located near the corner. The larger voids could lead to the higher thickness of the standoff, since the volume of the solder paste on both sides should be the same.

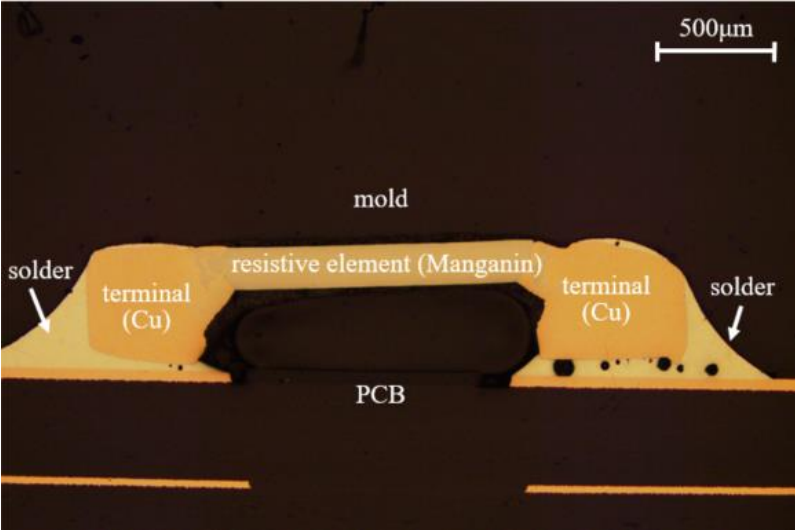


Fig. 4.39: Cross-section of shunt C after reflow (3 mΩ, II - II cutting plane)

Fig. 4.40 presents the cross-sectional pictures of shunt C after different numbers of power cycles. The crack is observed to initiate from the solder standoff and propagate later through the whole solder joint. No polarity effect is detected in the failure mode. However, the crack length is often longer in the side of the solder joint, where the thickness of the standoff is thinner.

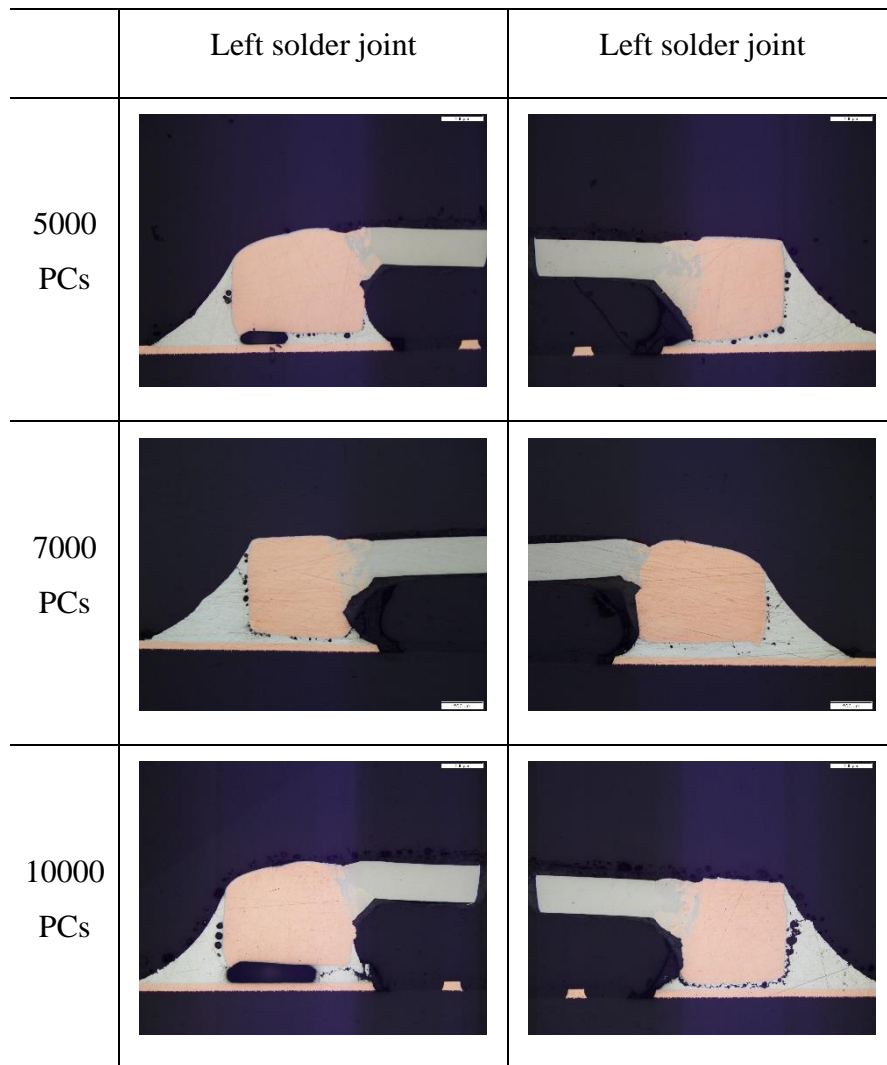


Fig. 4.40: Cross-section of shunt C (test Nr. 19: 3 mΩ, 45 A @2 s, 90 °C)

Fig. 4.41 displays the SEM analysis of shunts after 16000 PCs. Large cracks are observed in the solder joint with thinner solder standoff. At the other side of the solder joint, a smaller crack is initiating at the solder standoff. The marked ROI A, ROI B, ROI C and ROI D exhibit the critical location where damage is normally formed. The microstructural evolution of the solder joint at the location of ROIs is shown in Fig. 4.42 with larger magnification. Coarsening of Ag₃Sn and recrystallization are observed in both sides of the solder joint after current stressing. No polarity effect of microstructure evolution is noticed in the Sn matrix. Large cracks are formed at the standoff and the meniscus of the left solder joint, propagating along the grain boundaries. More severe damage occurs at the side of the solder joint with thinner solder standoff, which is independent of the current direction. Hence the dominant failure mode of shunt C exposed to current pulses is observed to be related to TMF cracks, owing to the impact of the configuration, voiding and various standoff height.

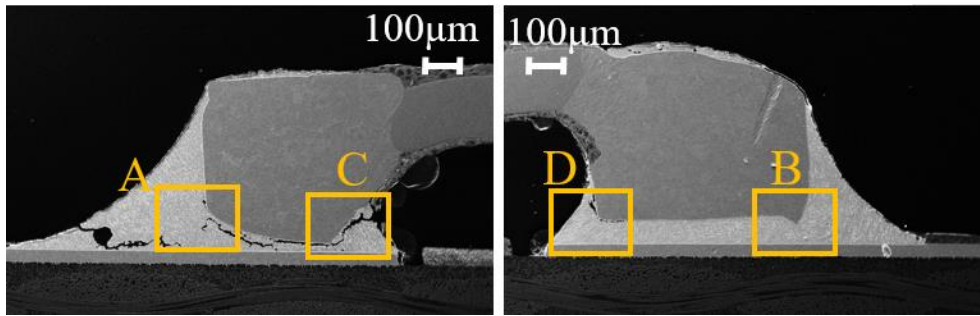


Fig. 4.41: SEM analysis of shunt C after 16000 PCs (test Nr. 19: 3 mΩ, 45 A @ 2 s, 90 °C, Mag=40×)

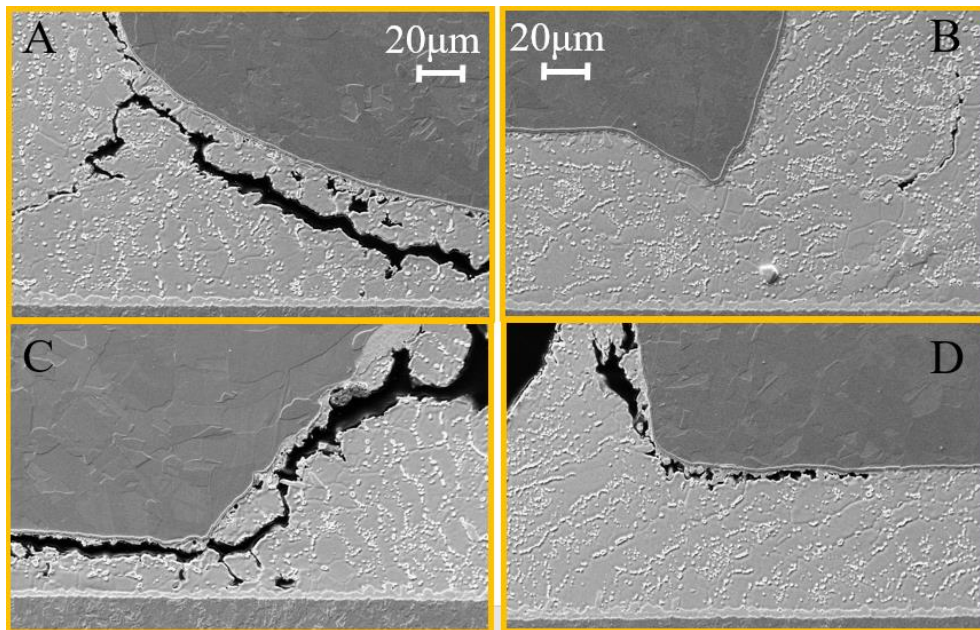


Fig. 4.42: Microstructural evolution of solder of shunt C (test Nr. 19: 3 mΩ, 45 A @ 2 s, 90 °C, mag=250×)

5 Simulation

FEM simulation is performed to assess the electrical, thermal and structural fields in the assembly during power-cycling tests. Thermo-electrical analysis mode is utilized to study the temperature fluctuation owing to the Joule-heating of the components. Transient structural analysis is further carried out to investigate the resultant response of the solder interconnect due to the mismatch of temperature and the mismatch of CTE of the joint elements. This chapter will discuss the detailed approach regarding the modeling of the assembly, material assignment, definition of the boundary conditions and post-processing. The numerical results are evaluated and compared with the experimental observations.

5.1 Modeling and boundary conditions

The main geometrical dimensions of the components are specified in the product specification. The missing parameters are obtained by measuring the cross-sectional pictures. One important missing parameter is the dimension of the laser cut in the resistive element. Laser trimming in the resistor is commonly used to adjust the resistance value via narrowing or lengthening the current flow, which highly influences the self-heating behavior of shunts under active loads.

5.1.1 Geometry modeling

a) Model of shunt A

The schematic construction of shunt A is displayed in Fig. 5.1 and the main dimensions are listed in Table 5.1. Cross-sectional images are taken to measure the dimensions of the inner structure of the shunt. Fig. 5.2 exhibits the simulative model of shunt A with 5 mΩ and 3 mΩ in comparison with the cross-sections of the representative specimens.

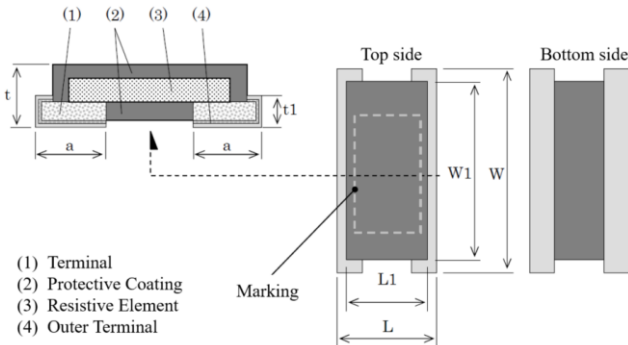
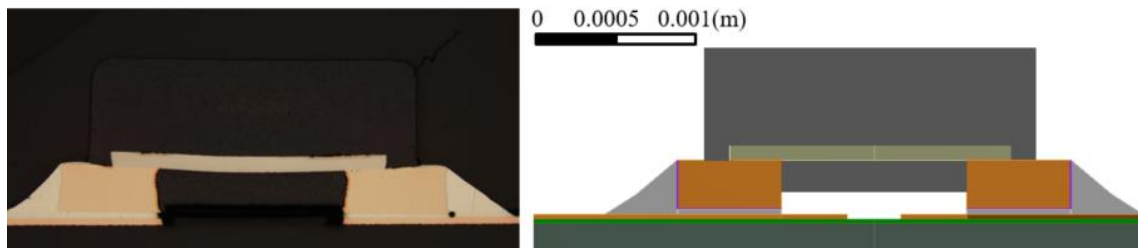


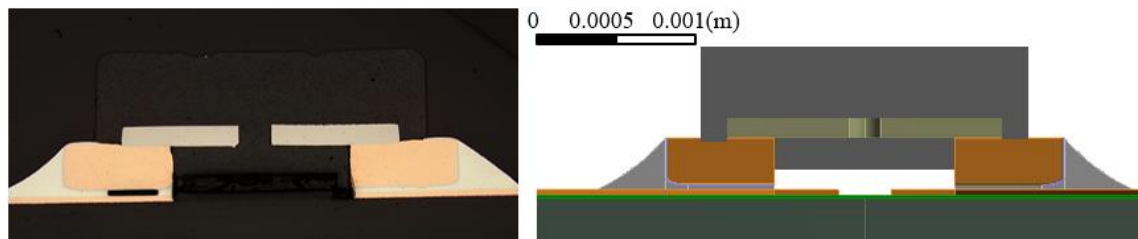
Fig. 5.1: Schematic construction of shunt A

Table 5.1: Main dimensions of shunt A

	t	a	t1	W	W1	L	L1
Dimension [mm]	1.00 ±0.25	0.60 +0.15/-0.20	0.30 ±0.10	5.00 ±0.25	4.6 ±0.10	2.55 ±0.25	2.15 ±0.10



(a) Cross-section and simulation model of shunt A (5 mΩ)



(b) Cross-section and simulation model of shunt A (3 mΩ)

Fig. 5.2: Simulation model of shunts A

b) Model of shunt B

The configuration and main dimensions of shunt B are illustrated in Fig. 5.3 and Table 5.2. Five laser cuts are observed in each shunt B component, which explains its relatively higher resistance compared to other shunts. As shown in Fig. 5.4, a half-model of shunt B is generated owing to the symmetric geometry and symmetric boundary conditions of shunt B. Though the geometry of shunt A is also symmetric, a full simulation model is required due to its asymmetric self-heating phenomenon and the polarity effect in the failure mode.

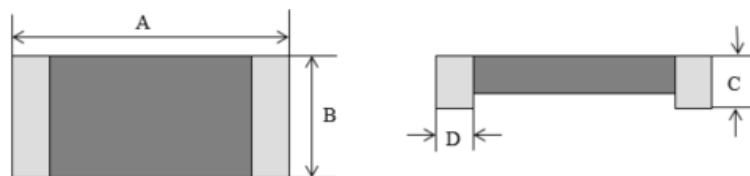


Fig. 5.3: Schematic construction of shunt B

Table 5.2: Main dimensions of shunt B

	A	B	C	D
Dimension [mm]	5.08 ± 0.254	2.54 ± 0.254	0.635 ± 0.254	0.508 ± 0.254

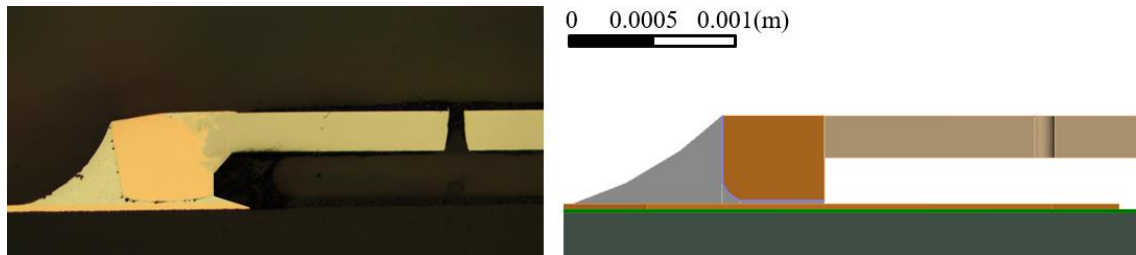


Fig. 5.4: Cross-section and half model of shunt B

c) Model of shunt C

The configuration of shunt C is displayed in Fig. 5.5. Table 5.3 shows the main dimensions of shunt C. A half simulation model is created for shunt C as well due to its symmetric electrical and thermal field. As mentioned in Chapter 4, one of the Cu terminals of shunt C is slightly smaller and is inclined to fail first. Therefore, the dimension of the smaller terminal is utilized for generating the simulation model since it describes the weaker location and is attributed to more critical loading conditions. The cross-sectional image and the half model of shunt C are presented in Fig. 5.6.

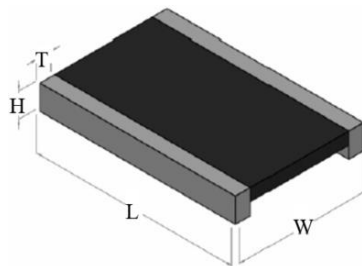


Fig. 5.5: Schematic construction of shunt C

Table 5.3: Main dimensions of shunt C

	L	W	H	T
Dimension [mm]	5.08 ± 0.254	2.54 ± 0.254	$0.508 + 0.178 / - 0.00$	0.381 ± 0.254

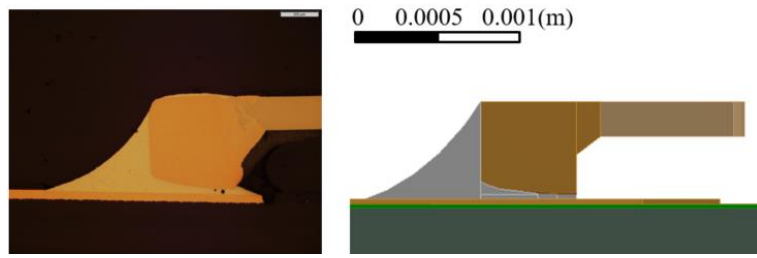


Fig. 5.6: Cross-section and half model of shunt C

The test layout has been introduced in section 3.2. The PCB is modelled as 6 layers of alternating copper foil and prepreg, which is in agreement with the PCB production. The same PCB stack-ups have been modelled for all the assemblies. The simulation model of the assembly of shunt A (5 mΩ and 3 mΩ) is displayed in Fig. 5.7 and the half model of the assembly of shunts B and C is shown in Fig. 5.8.

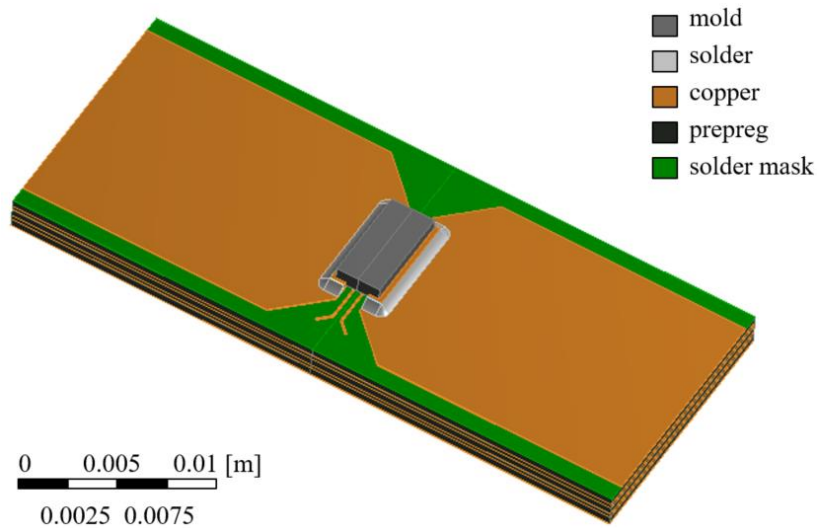
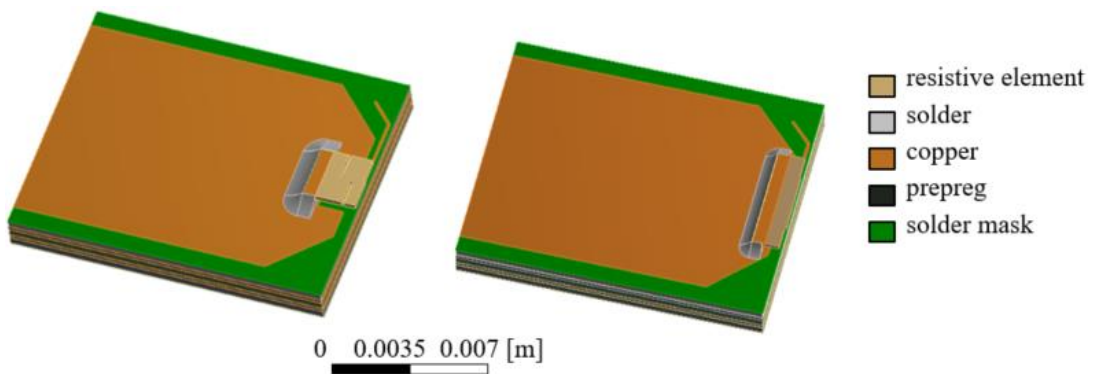


Fig. 5.7: Simulation model of the assembly of shunt A



(a) assembly of shunt B

(b) assembly of shunt C

Fig. 5.8: Half model of the assembly of shunt B and shunt C

5.1.2 Material assignment

The main material properties of the shunts are provided by suppliers and are listed in Table 5.4. The terminals of all the shunts consist of pure copper. The resistive element of shunt A is made of CuNi alloy. The material of the resistive element of shunt B and C is a Ni-Cr alloy. The Seebeck coefficient of Cu-CuNi alloy is collected from the work from Chukwu [121, 127]. The thermoelectric effect is not investigated at the joint of Cu-NiCr alloy, since the two materials are connected via a melt area and no polarity in self-heating is observed. The shunt B and shunt C are encapsulated in a very thin layer of mold, which hardly affects the deformation of the component under active load.

The material data of the PCB are obtained via TMA (Thermal Mechanical Analysis) and DMA (Dynamic Material Analysis) measurements from Bosch internal. The Chaboche model is implemented to characterize the time-dependent cyclic plasticity of the solder material. The stress-strain data are derived from low cycle fatigues tests of the SAC 405 solder joint at different temperature and at different strain rates. The material model applies for loading conditions with a strain rate from 10^{-3} [s⁻¹] to 10^{-1} [s⁻¹]. The thermo-mechanical stress induced by the high current pulses occurs at a strain rate in the order of 10^{-1} [s⁻¹], which is within the application of the adopted Chaboche model. The Chaboche model derived from data fitting is interpreted in Ansys Parametric Design Language (APDL) script, which is later defined in the pre-processing.

Table 5.4: Material properties for simulation.

	Mold	Cu-Ni alloy	Ni-Cr alloy	Terminal	Terminal plating
Coefficient of liner expansion [-]	25.0	15.0	13.0	16.5	13.0
Elastic modulus [GPa]	2.5	199.5	193.05	130.0	206
Thermal conductivity [W/m·K]	0.487	23.0	14.6	398-400	91
Specific heat [J/g·K]	1.1	0.4	0.5	0.39-0.40	0.443
Density [g/cm ³]	1.6	8.9	8.1	8.9	7.95
Poisson's ratio	0.4	0.343	0.3	0.312	0.31
Resistivity [$\Omega \cdot m$]	1.0E8	4.50E-7	1.33E-6	2E-9-2.9E-8	6.93E-8
Seebeck coefficient [V/K]	-	-3.5E-5	-	6.5E-6	-

5.1.3 Boundary conditions

(1) Thermo-electrical analysis

The thermo-electrical analysis in Ansys is originally a static analysis. APDL script is implemented to change the analysis to transient analysis since the temperature change is highly affected by the time constant.

The current profile is defined according to the testing conditions (Table 3.5) and the current is applied to the top copper pad of the PCB. Current is flowing through the component to the other side of the PCB, where the voltage is defined to be 0 V. For the half model of shunt B and shunt C, the voltage at the symmetric plane is defined to be 0 V. The temperature of the assembly is raising up due to the self-heating of the component and cools down to the environmental temperature via convection. The surfaces of the assembly are selected as convective surfaces, which are highlighted in yellow for shunt A and in red for shunt B in Fig. 5.9. The convection coefficient is preliminary defined to be 25 W/m^2 as ECU-level simulation. The boundary conditions of shunt C are assigned to be the same as that of shunt B. Three current pulses are simulated to reach stabilized results, which serve as the input for the further structural analysis.

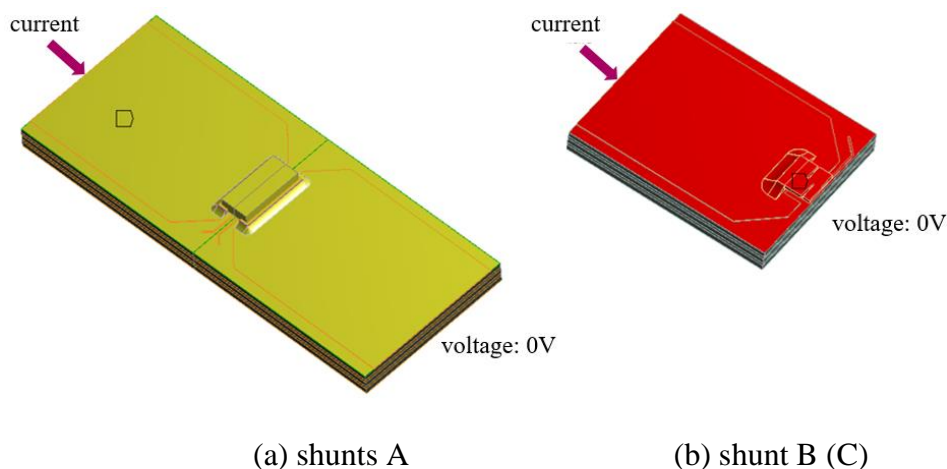


Fig. 5.9: Boundary conditions for the thermo-electrical analysis

(2) Static structural analysis

The temperature distribution in the assembly is derived after solving the thermo-electrical analysis and is afterwards imported into the static structural analysis as temperature load. The mechanical boundary conditions for static structural analysis are illustrated in Fig. 5.10. For the simulation model of shunt A, the displacement and rotation of the PCB are restrained by fixing 6 degrees of freedom of vertex 1-3. Half models are created for shunt B and shunt C, therefore the displacements at the symmetric planes are defined to restrain the movement of the model in the direction perpendicular to the plane (z-axis). The displacements of vertex 4 and 5 define the

fixation of the PCB and restrict the rotation of the PCB, as interpreted in Fig. 5.10 and Table 5.5. The mechanical boundary conditions of the assembly of shunt C are the same as the boundary conditions of shunt B, as shown in Fig. 5.10 (b).

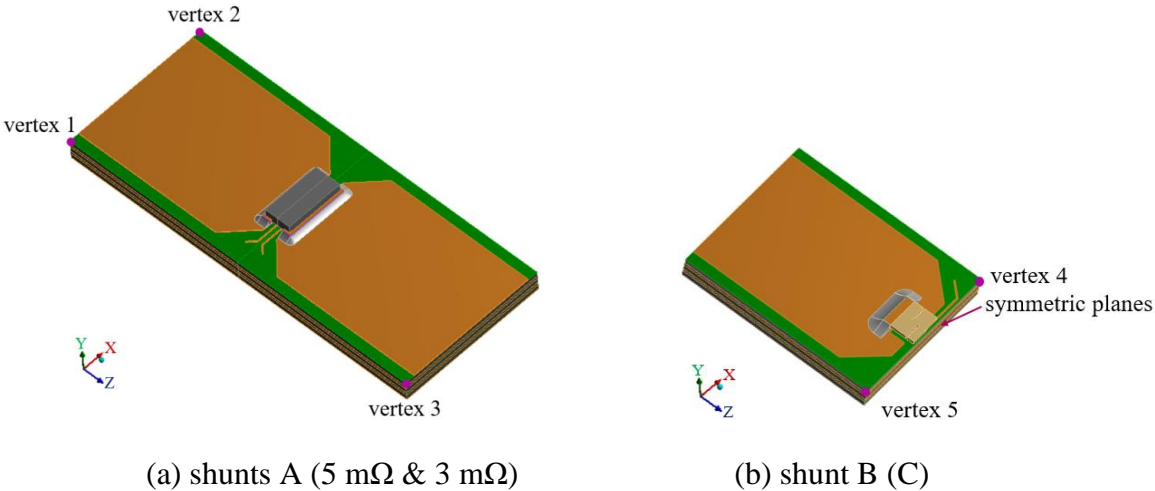


Fig. 5.10: Mechanical boundary conditions for static structural analysis

Table 5.5: Mechanical boundary conditions

	x-axis	y-axis	z-axis
Vertex 1	0	0	0
Vertex 2	free	0	0
Vertex 3	free	0	free
Vertex 4	0	0	free
Vertex 5	free	0	free
Symmetric planes	free	free	0

5.2 Validation of the model

5.2.1 Mesh investigation

Fig. 5.11 presents the simulation model after meshing. The solder joint is the ROI where the failure takes place. Therefore, the solder standoff is meshed with sweeping method to obtain hexahedral elements. The meshing shown in Fig. 5.11 yields 50 elements in x-direction, 10 elements in z-direction, and 3 elements in y-direction. Meshes with high mesh densities provide precise results while increasing CPU time and memory requirements. However, simulation errors can occur if the mesh is too coarse. Hence, a mesh sensitivity analysis is conducted to obtain an appropriate method of meshing to derive reasonably good results and to avoid wasting the computer resources and

simulation time. Different mesh sizes, as displayed in Fig. 5.12, are applied to the solder standoff and the corresponding simulation solutions are compared. If the simulations with different meshing sizes yield nearly identical results, the larger mesh size is considered to be adequate for good results. If the simulations give results with large differences, the applied meshing sizes should be further refined.

The stress introduced by the current pulses is of great significance to assess the thermo-mechanical load exerted on the solder. Therefore, the normal stress in the solder standoff is chosen to be compared among the different meshing sizes. The normal stress derived from simulation is plotted with respect to the number of the elements in the solder standoff in Fig. 5.13. When the mesh density reaches meshing method 3, the normal stress shows minor increment with increasing mesh elements. This indicates that the meshing method 3 is appropriate for obtaining useful simulation results and further refining of the mesh is not necessary. A similar mesh sensitivity study is also performed for the model of shunt B and mesh density 3 is optimal for the following simulations, as shown in Fig. 5.13. For the other bodies in the model, sweeping method is applied wherever possible. Hex dominant is implemented when the geometry is complex. The shunt C yields the same dimension of the solder pad. Therefore, the same mesh density is utilized in case of the simulation model of shunt A.

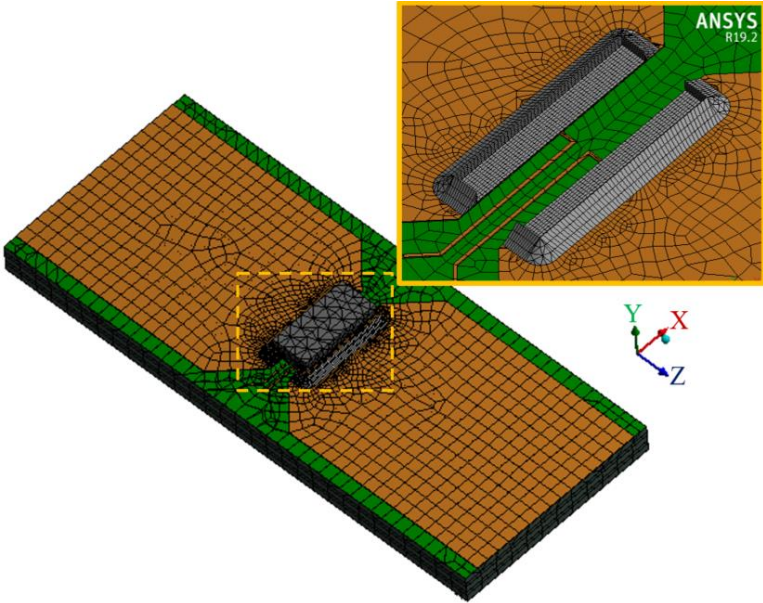


Fig. 5.11: Meshing of shunt A

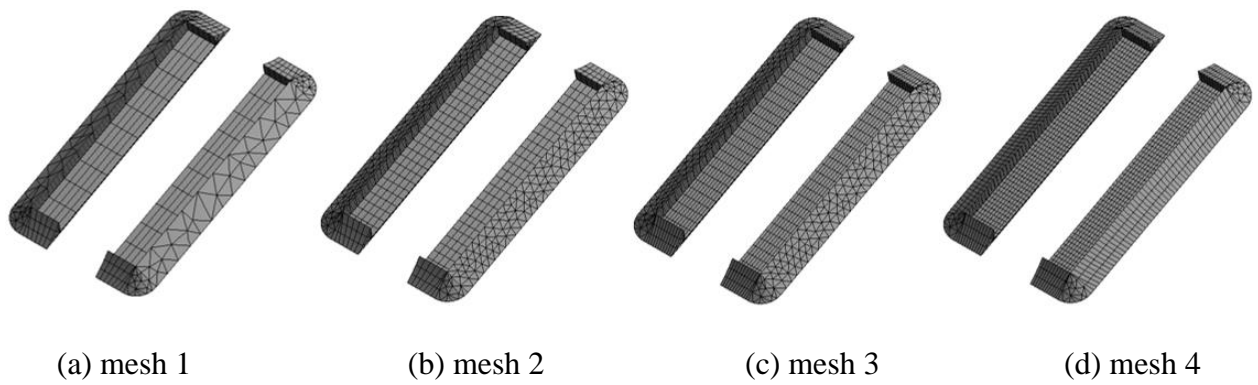


Fig. 5.12: Different meshing sizes of the solder standoff

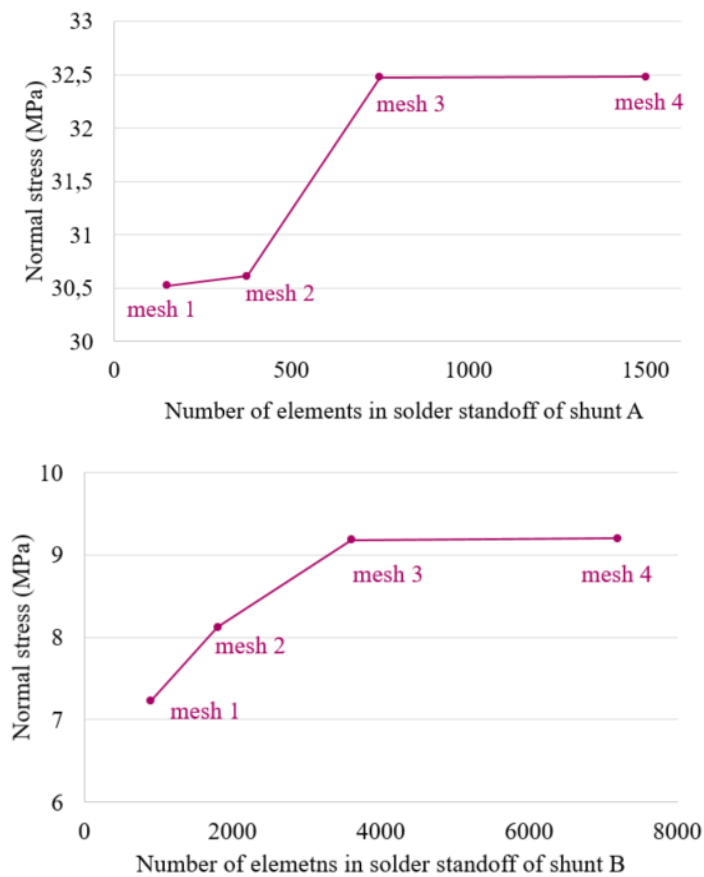


Fig. 5.13: Meshing investigation of the simulation model

5.2.2 Validation with measurements

(1) Validation of resistance

The resistance of shunts highly depends on the dimensions of the resistive element and the laser cut, which significantly affects the self-heating of the components. The information regarding the dimensions of the component is provided by product specification and is further measured with cross-sections. The locations of laser cuts are fixed based on the measurement. Shunt A and shunt C have one laser cut in each component, while each shunt B has 5 laser cuts. The width and length

of the laser cuts are measured from cross-sectional images. Each specimen shows a slight difference in the measurement. The width and length of the laser cuts are chosen as parameters and the final dimensions for model generation are determined via parametric study to validate the simulation model with the corresponding resistance of the components.

Fig. 5.14 exhibits the distribution of electric voltage of the assembly with the optimal parameter selected via parametric study. The resistance of shunt A in Fig. 5.14 (a) is calculated to be 4.93 mΩ via dividing the electric voltage by current, which yields a relative difference of -1.29% with the resistance measurement. Fig. 5.14 (b) presents the contour of electric voltage after the current stressing of 45 A. The resistance is evaluated to be 3.23 mΩ, which is within 8% of the relative difference from the measured value. The resistance of the half model of shunt B and shunt C is calculated to be 14.33 mΩ and 1.52 mΩ, with relative difference within ±4.44% with the measurement. Therefore, the simulation models represent well the electrical properties of each shunt component.

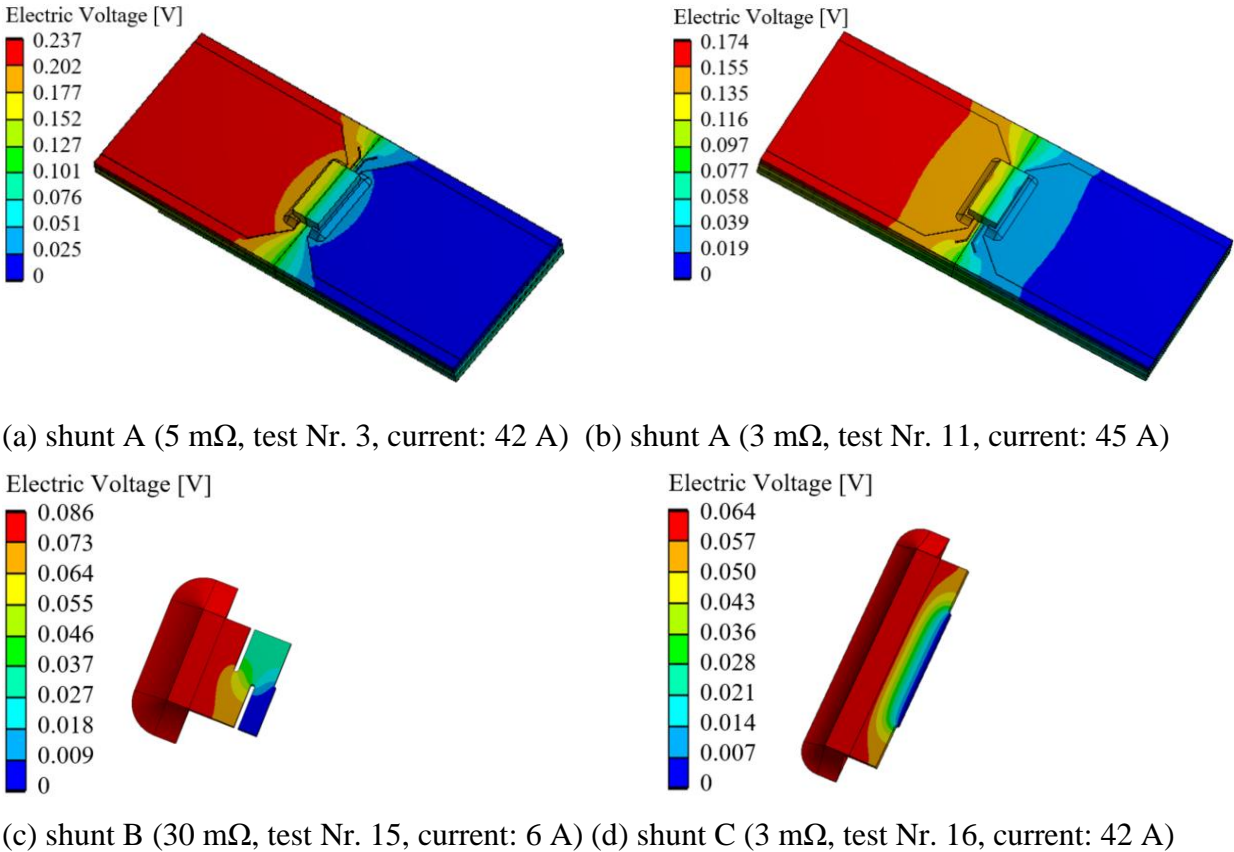


Fig. 5.14: Electric voltage of the assembly at the end of the current pulse

(2) Validation of thermal simulation

The thermal simulation of the assembly is validated with thermography measurements. As illustrated in chapter 3, thermography measurements are conducted to investigate the self-heating

of the components. Fig. 5.15 displays one representative thermography measurement of shunt A (3 mΩ) at room temperature. The probes marked with “SP” are selected by the spotmeter tool of the FLIR software. Three probes of the numerical model are selected for comparison of the simulation results and the thermography measurement. A parametric study is performed to derive the optimal Peltier coefficient and convection coefficient which lead to a temperature distribution in agreement with the thermography. The thermal simulations of the three probes are displayed in Fig. 5.16 and the corresponding thermography measurement points are plotted in the same diagram for comparison.

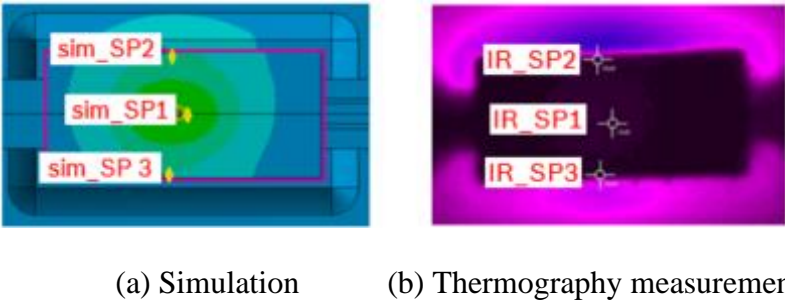


Fig. 5.15: Probes of simulation and thermography measurements of shunt A

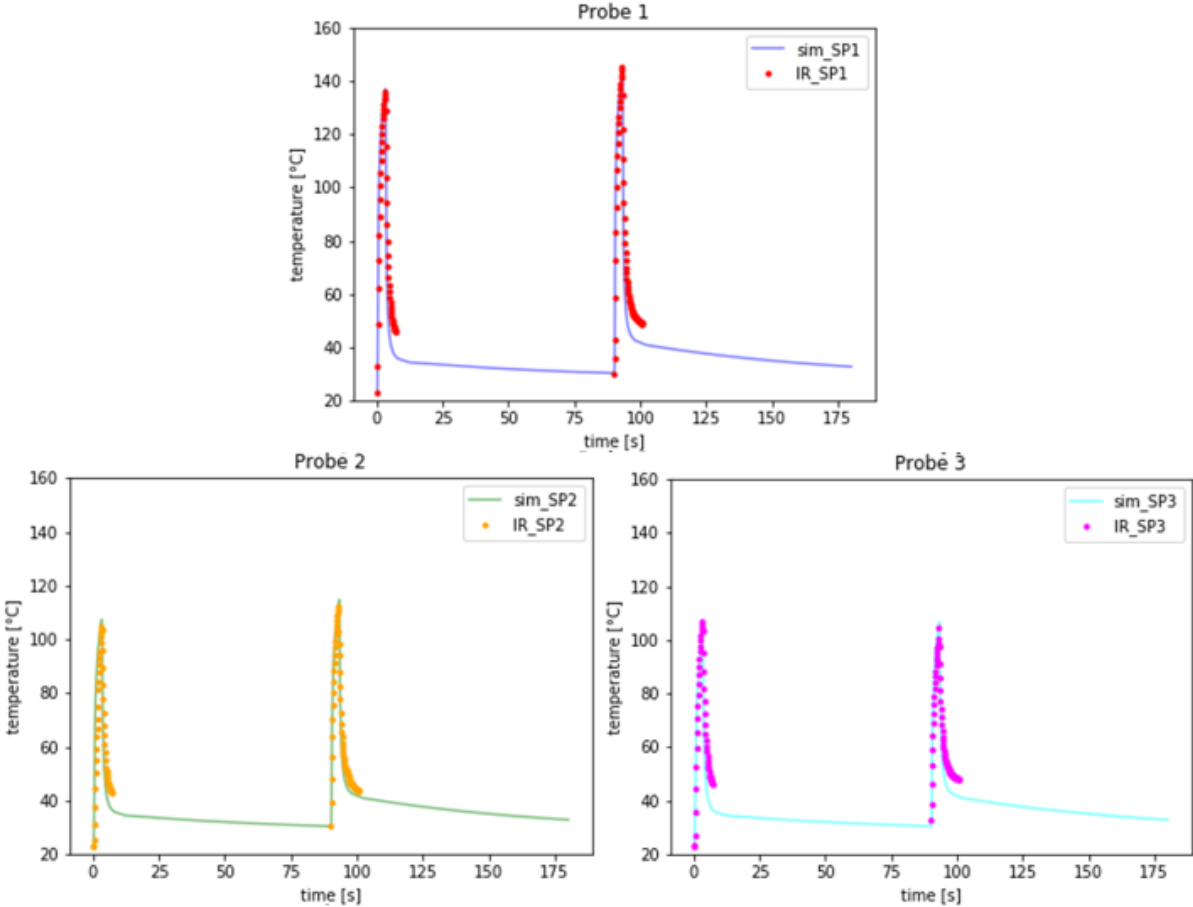
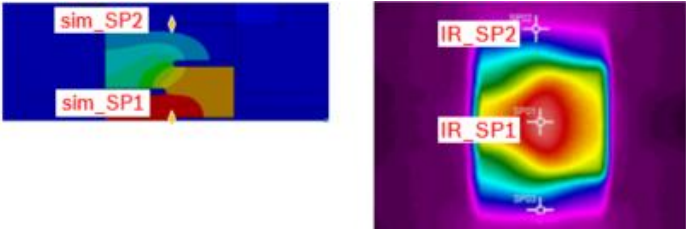


Fig. 5.16: Comparison of simulation and thermography measurements of shunt A (3 mΩ; 34 A @3 s; room temperature)

Probe 1 is located at the hotspot and is exposed to the highest temperature among the three probes. Probe 2 and Probe 3 are located symmetrically, however yield different temperature due to the Peltier effect. It is observed that the solid line obtained from simulation is in good agreement with the measurement points at the heating stage, reaching the maximal temperature with $\pm 5\%$ relative difference. The IR measurement shows a relatively slower cooling rate than the simulation when current is removed. This discrepancy can be accepted since the air circulation in the test chamber is faster than the IR measurement environment. It is noted that the asymmetric self-heating can be reproduced via simulation by taking the Peltier effect into account. Consequently, the simulation model offers an accurate description of the self-heating of shunt A and will be further used to evaluate the damage parameters of the assembly.

For shunt B and shunt C, two probes are selected for the comparison of thermal simulation and thermography measurements. Probe 1 is locating at the symmetric plane of the half model, which corresponds to the hotspot SP1 marked in thermography measurement. The positions of the probes for shunt B and shunt C are specified in Fig. 5.17 and Fig. 5.19 respectively. The simulated temperature profile of the probes and the measured temperature data are plotted in Fig. 5.18 and Fig. 5.20. It is observed that the shape of the simulative profile fits well with the measured data points, including the heating-up stage and cooling-down stage. The relative difference of the simulated and measured temperature of probe 1 is within $\pm 5.5\%$ for shunt B and within $\pm 5.0\%$ for shunt C. The relative difference of probe 2 for both shunt B and shunt C is within $\pm 2.1\%$. It can be concluded that the simulation model of shunt B and shunt C also characterizes well the self-heating of the components.



(a) Simulation (b) Thermography measurement

Fig. 5.17: Probes of thermography measurements of shunt B

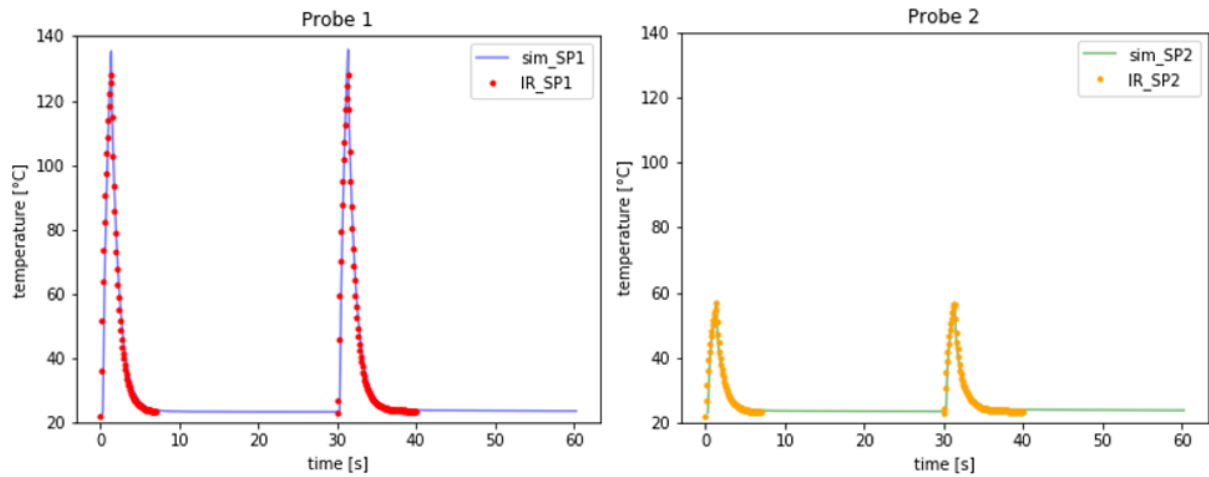
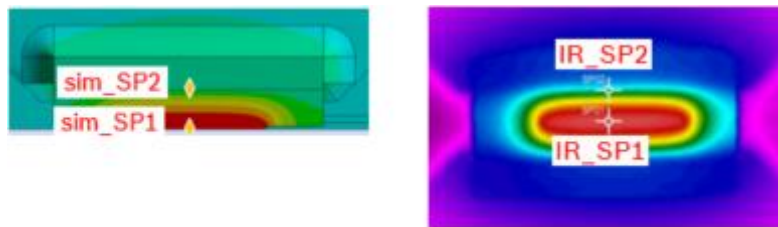


Fig. 5.18: Comparison of simulation and thermography measurements of shunt B
(30 mΩ, 6 A @1 s, room temperature)



(a) Simulation (b) Thermography measurement

Fig. 5.19: Probes of thermography measurements of shunt C

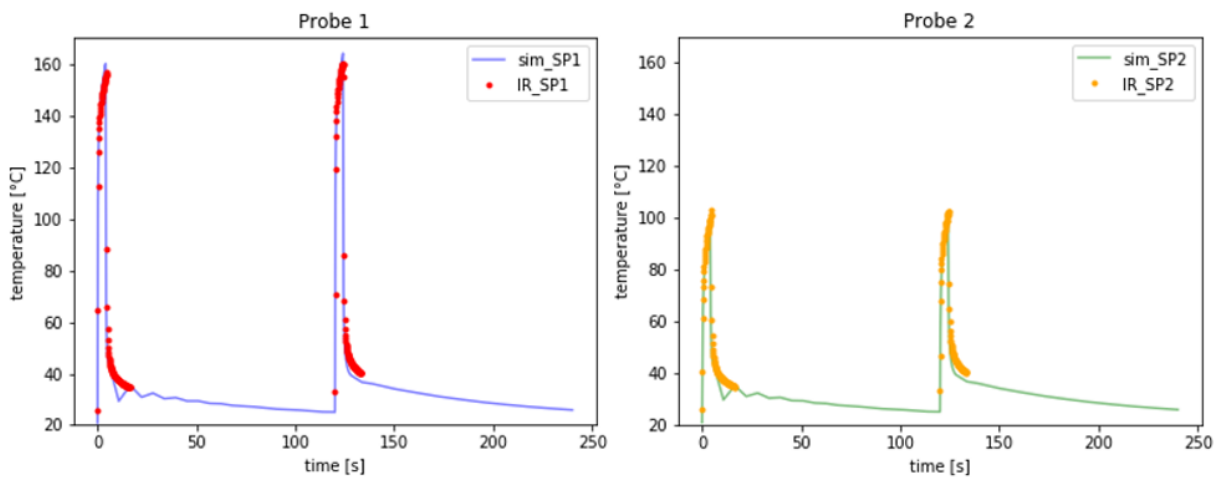


Fig. 5.20: Comparison of simulation and thermography measurements of shunt C
(3 mΩ, 35 A @4 s; room temperature)

5.3 Evaluation of simulation results

The electrical-thermal-structural simulations of all the test conditions (test Nr. 1- test Nr. 19) are interpreted in this section. The results are discussed according to shunt types. The simulation

results in the solder joint are displayed and discussed in detail, since the solder joint is the weakest location where failure occurs.

5.3.1 Simulation of shunt A (5 mΩ)

(1) Electro-thermal analysis

Power cycling tests of 8 different loading conditions have been conducted on shunt A (5 mΩ), as specified in section 3.2.4. Numerical investigation has been performed on each loading condition and the results after three current pulses are selected for evaluation. Fig. 5.21 exhibits the electro-thermal analysis of the assembly under a representative loading condition (Test Nr. 6).

As displayed in Fig. 5.21, the distribution of the current density in the solder joint is symmetric, regardless of the current direction. Current crowding is observed at the corner of the solder meniscus, which yields a current density around $3.78E3 \text{ A/cm}^2$. The temperature is distributed asymmetrically in the assembly and in the solder joint, as a result of the thermoelectric effect. The maximal temperature of the solder joint at the anode side (left side) is around $10 \text{ }^\circ\text{C}$ higher than at the cathode side (right side). The solder joint at anode side also yields a higher thermal gradient.

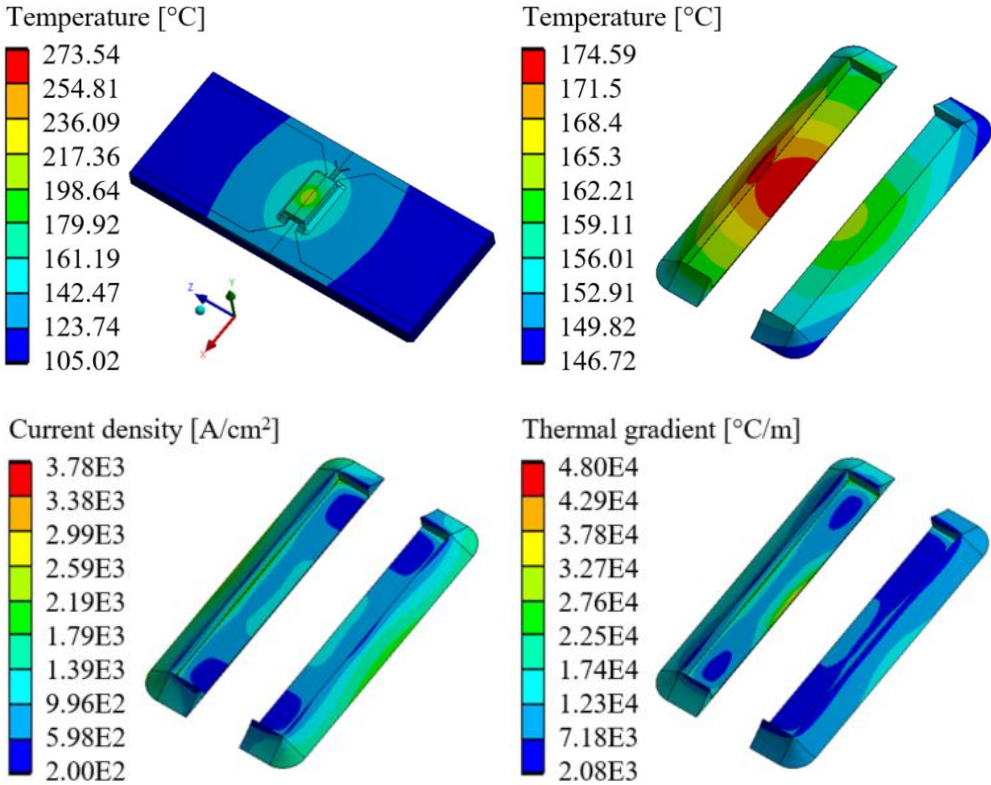


Fig. 5.21: Electro-thermal simulation of shunt A (test Nr. 6: 5 mΩ, 34 A @3 s, 100 °C)

The electrical and thermal field of other loading conditions yield a similar distribution. The results of the corresponding loading conditions are summarized in Table 5.6. Test Nr. 1 applies the highest

current density on the solder joint since the exerted current range is the highest. The solder joint undergoes the highest temperature under Test Nr. 3 due to the longest pulse length and the maximal heat generation.

Table 5.6: Electro-thermal simulation of all the loading conditions of shunt A (5 mΩ)

Test	Max. current density [A/cm ²]	Max. temperature [°C]	Max thermal gradient [°C/m]
1	7.89E3	179.80	1.41E5
2	6.81E3	155.54	1.06E5
3	4.66E3	182.48	6.79E4
4	3.94E3	151.19	4.91E4
5	3.17E3	134.10	3.39E4
6	3.78E3	174.59	4.80E4
7	2.93E3	143.50	3.05E4
8	2.05E3	120.68	1.71E4

(2) Mechanical analysis

The result of the thermal simulation is imported to structural analysis as input load. The materials of the assembly expand and contract due to the thermal fluctuation, which leads to the deformation of the assembly, as displayed in Fig. 5.22. Solder joints have to accommodate the deformation and undergo cyclic thermo-mechanical stress. The maximal normal stress is located at the solder standoff for both sides. The accumulated plastic strain describes the accumulation of the cyclic thermo-mechanical load and indicates the occurrence of thermo-mechanical fatigue. As a result of the higher thermal load at the anode side, the accumulated plastic strain yields a higher value at the anode side of the solder joint. And the maximal accumulated plastic strain is located at the solder standoff at the anode side.

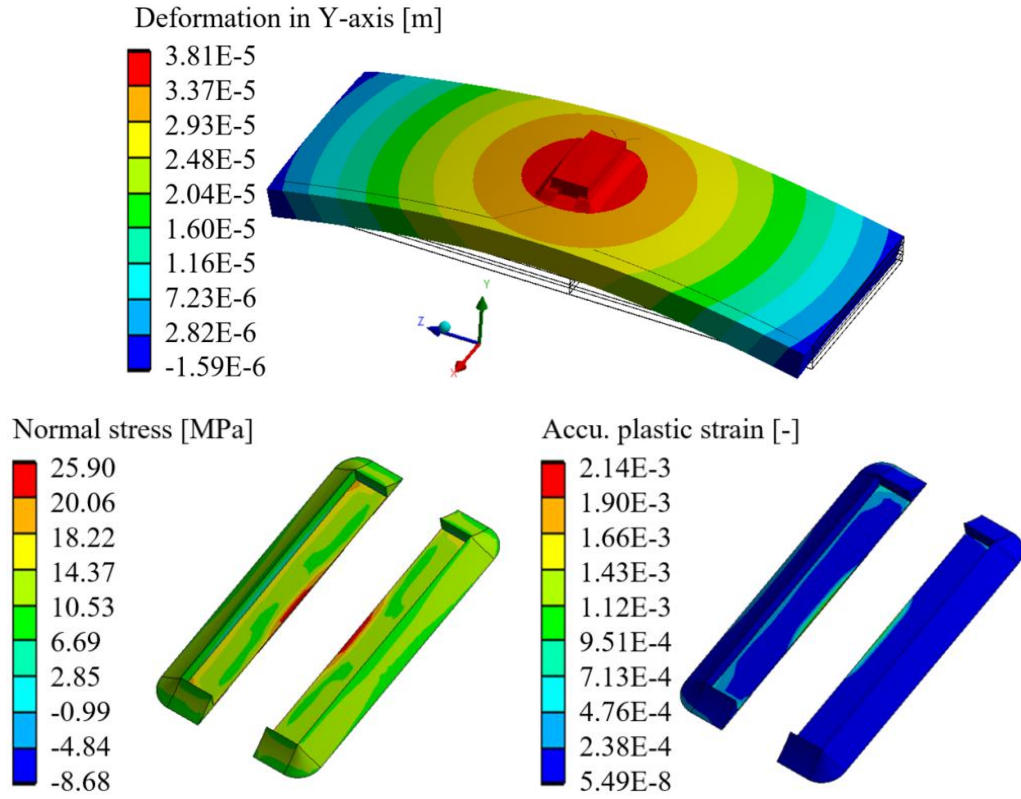


Fig. 5.22: Structural simulation of shunt A (test Nr. 6: 5 mΩ, 34 A @3 s, 100 °C)

The parameters are further evaluated with weighted volume average (VWA) method to avoid singularity and mesh dependency as described in (5.1). The accumulated plastic strain $\varepsilon_{acc_VWA}^{pl}$ in the anode solder joint is evaluated with VWA method during post-processing. The solder elements are listed in descending order of their accumulated plastic strain. The sum of the product of each element volume V_i and the accumulated plastic strain $(\varepsilon_{acc}^{pl})_i$ divided by the total volume of all selected elements equals to the $\varepsilon_{acc_VWA}^{pl}$. In this work, the elements with maximum 20% accumulated plastic strain are selected for the evaluation.

$$\varepsilon_{acc_VWA}^{pl} = \frac{\sum_{i=1}^n [(\varepsilon_{acc}^{pl})_i \cdot V_i]}{\sum_{i=1}^n V_i} \quad (5.1)$$

Stress and strain exhibit a similar distribution for all the other test conditions and the corresponding values are documented in Table 5.7. It is noted that the solder joint undergoes relatively high thermo-mechanical loads under test Nr. 1, Nr. 2, Nr. 3, Nr. 4 and Nr. 6 owing to the higher current range.

Table 5.7: Structural analysis of all the loading conditions of shunt A (5mΩ)

Test	Max. normal stress [MPa]	Max. accu. plastic strain [-]	VWA accu. plastic strain [-]
1	56.34	2.43E-02	2.56E-3
2	55.32	1.18E-02	1.07E-3
3	33.94	6.14E-03	1.58E-3
4	25.44	1.87E-03	6.65E-4
5	20.03	6.52E-04	9.97E-5
6	25.24	2.14E-03	3.60E-03
7	19.46	3.93E-04	5,45E-05
8	15.75	1.22E-04	1.69E-05

(3) Simulation of migration phenomenon

As mentioned in section 2.4, electromigration might take place when the current density is around $2.0E3 \text{ A/cm}^2$ and will become dominant when the current density reaches $1.0E4 \text{ A/cm}^2$. The loading conditions of shunt A fall into the critical range. Hence the risk for migration is investigated. The algorithm to investigate the migration phenomenon has been illustrated in section 2.4. The diffusion parameters are defined according to Table 5.8. Fig. 5.23 presents the material flux density and the divergence of material flux density due to electromigration and thermomigration. It is observed that the maximum EM-induced material flux density and divergence of material flux density in the solder joint is located at the corner of the solder meniscus, while the maximum TM-induced material flux density and divergence of material flux density takes place at the edge of the solder standoff. The EM-induced parameters yield approximately three orders of magnitude higher values than the TM-induced parameters. Consequently, the EM-induced material transport can be considered as the dominant migration mechanism and the solder joint is subjected to high risk of electromigration under the testing conditions of this work.

Table 5.8: Diffusion parameters for simulation of migration phenomenon

$Z^*_{Cu/Sn}$	$Z^*_{Cu/Cu6Sn5}$ n5	ρ_{Sn} ($\Omega \cdot m^{-1}$)	ρ_{Cu6Sn5} ($\Omega \cdot m^{-1}$)	C_{Cu} (at. $\cdot cm^{-3}$)	$C_{Cu/Cu6Sn5}$ (at. $\cdot cm^{-3}$)
2 [128]	26 [129]	11E-8	17.50E-8	8.44E22 [125]	3.7E22 [125]
c_s (at. $\cdot cm^{-3}$)	D_1 ($m^2 \cdot s^{-1}$)	Q_1 (eV)	D_2 ($m^2 \cdot s^{-1}$)	Q_2 (eV)	
0.11E21 [125]	2.40 E-7 [107]	0.34	1.81 E-5 [130]	1.37 [130-131]	

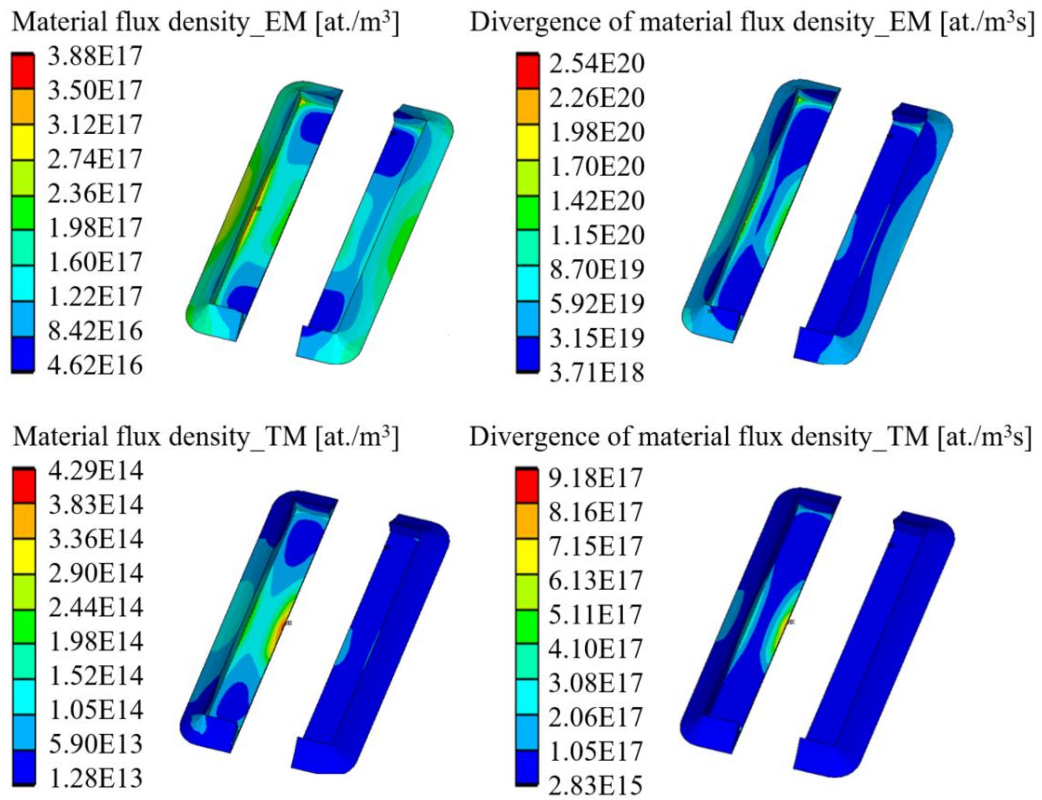


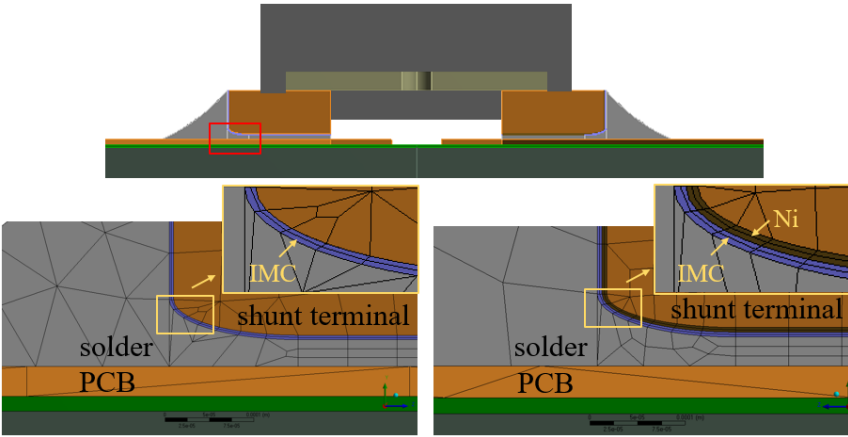
Fig. 5.23: Electromigration and thermomigration of solder joints of shunt A (Test Nr. 6, 5 m Ω , 34 A @3 s, 100 °C)

5.3.2 Simulation of shunt A (3 m Ω) and shunt A*

(1) Electro-thermal-structural analysis

The simulation and evaluation procedure of shunt A (3 mΩ) and shunt A* are similar to the above analysis with shunt A (5 mΩ). The simulation of the interface of shunt A (3 mΩ) and shunt A* are highlighted in this section owing to their different plating.

In the simulation model of shunt A (3 mΩ) with only Sn plating, a IMC layer with 5 μm thickness is modelled between the shunt terminal and the bulk solder joint. The IMC layer is meshed with 2 layers of elements. Apart from the IMC layer, a Ni layer is modelled between the IMC and termination for the shunt with Ni plating, as displayed in Fig. 5.24. The IMC formed with and without Ni plating is detected by EDS analysis to be (Cu, Ni)₆Sn₅ and Cu₆Sn₅, respectively. The Ni addition leads to higher elastic modulus and higher hardness in the IMC layer, as listed in Table 5.9 [80].



(a) shunt with only Sn plating (b) shunt with Ni plating
Fig. 5.24: Simulation models of shunt A (3 mΩ) with different plating

Table 5.9: Material properties of IMC

Material	Elastic modulus [GPa]	CTE [ppm·K ⁻¹]
IMC: Cu ₆ Sn ₅	124.16 [80]	17.2
IMC: (Cu, Ni) ₆ Sn ₅	133.80 [80]	17.2

Fig. 5.25 presents the electro-thermal simulation of shunt A* with only Sn plating, where the higher temperature and thermal gradient are observed to be located at the anode side. Hence the asymmetric self-heating phenomenon of shunt A is reproduced by considering the Peltier effect. The mechanical load distribution depicted in Fig. 5.26 verifies the higher thermo-mechanical load at the anode side. The comparison of shunts with and without Ni plating is listed in Table 5.10, where Test Nr. 9-10 are performed on shunt A components and Test Nr. 11-12 are carried out on shunt A* components with the same loading conditions.

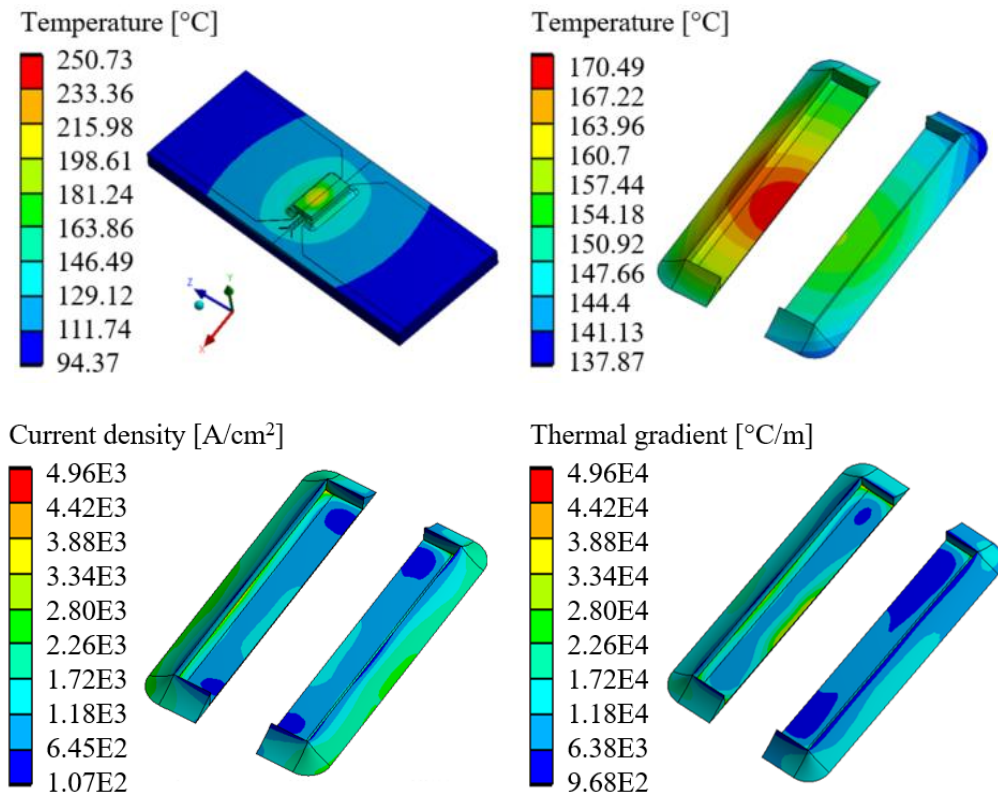


Fig. 5.25: Electro-thermal simulation of shunt A* (test Nr. 11: 3 m Ω , 45 A @2 s, 90 $^{\circ}\text{C}$)

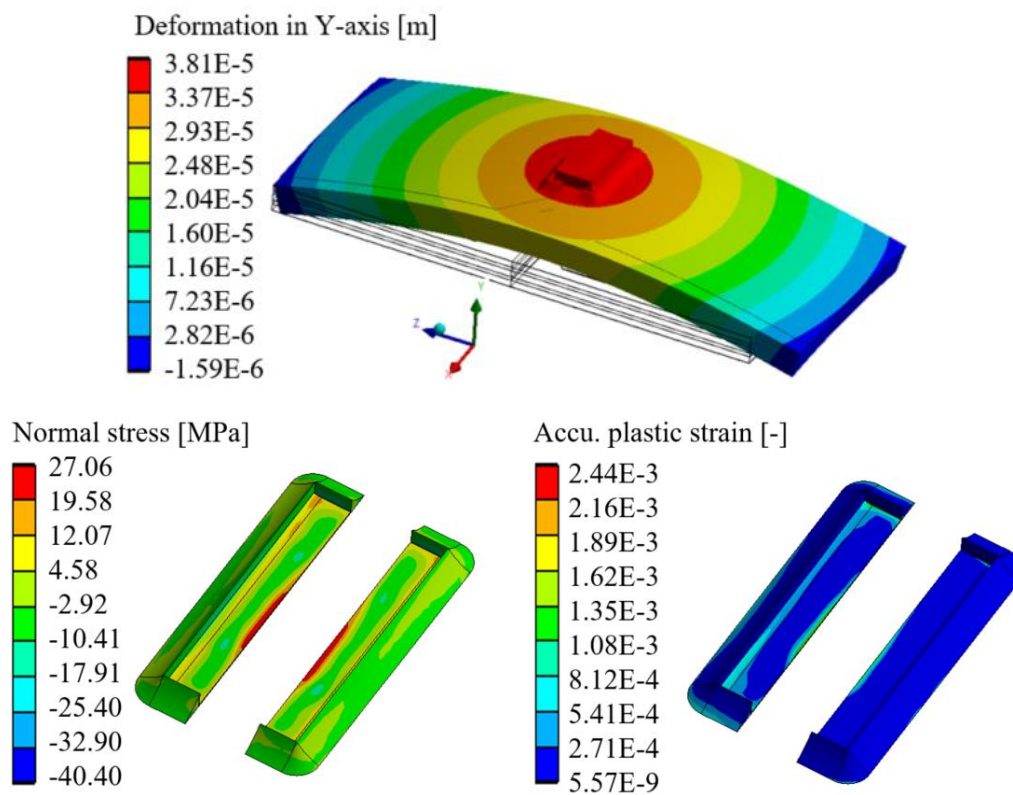


Fig. 5.26: Structural simulation of shunt A* (test Nr. 11: 3 m Ω , 45 A @2 s, 90 $^{\circ}\text{C}$)

Table 5.10: Simulation results of shunt A (3 mΩ) and shunt A*

Test	Max. current density [A·cm ⁻²]	Max. temperature [°C]	Max. normal stress [Mpa]	Max. accu. plastic strain [-]	VWA accu. plastic strain [-]
9	4.96E3	170.49	27.08	2.47E-3	4.41E-4
10	4.19E3	147.72	21.36	7.80E-4	10.00E-5
11	4.96E3	170.49	27.06	2.44E-3	4.40E-4
12	4.19E3	147.73	21.077	7.13E_4	9.91E-5

It is observed from Table 5.10 that, Ni plating and the different IMC compound have little influence on the current distribution and thermal distribution in the solder joint. Nearly the same maximum current density and maximum temperature are detected in Test Nr. 9 and Test Nr. 11, where the same current profiles are applied. The normal stress and accumulated plastic strain are slightly higher in Test Nr. 9 and Test Nr. 10, in comparison with Test Nr. 11 and Test Nr. 12. This could be explained by the higher Young's modulus of (Cu, Ni)₆Sn₅. The morphology of the IMC layer is not modelled in the simulation. The IMC layer, which is composed of Cu₆Sn₅, normally shows a scalloped structure, while the IMC of (Cu, Ni)₆Sn₅ exhibits a planarized layer. The planarization of the interface reduces the contact area between the IMC and solder, resulting in a decrease of shear force [25]. Therefore, thermo-mechanical mismatch cannot explain the earlier failure of shunt A with only Sn plating, even considering the morphology of the IMC layers. The degradation of the solder material due to the migration mechanism needs to be evaluated.

(2) Simulation of migration phenomenon

The EM- and TM- induced degradation are simulated and shown in Fig. 5.27. The divergence of material flux density induced by EM is approximately three orders of magnitude higher than TM, which indicates that the EM is the dominant migration phenomenon in the given loading condition. The maximal EM-induced divergence material flux density is located at the corner of the solder meniscus. This corresponds well with the experimental observations, where a polarity effect in IMC growth and void formation are detected. The simulation results describe well the location of material transport as observed in experiments.

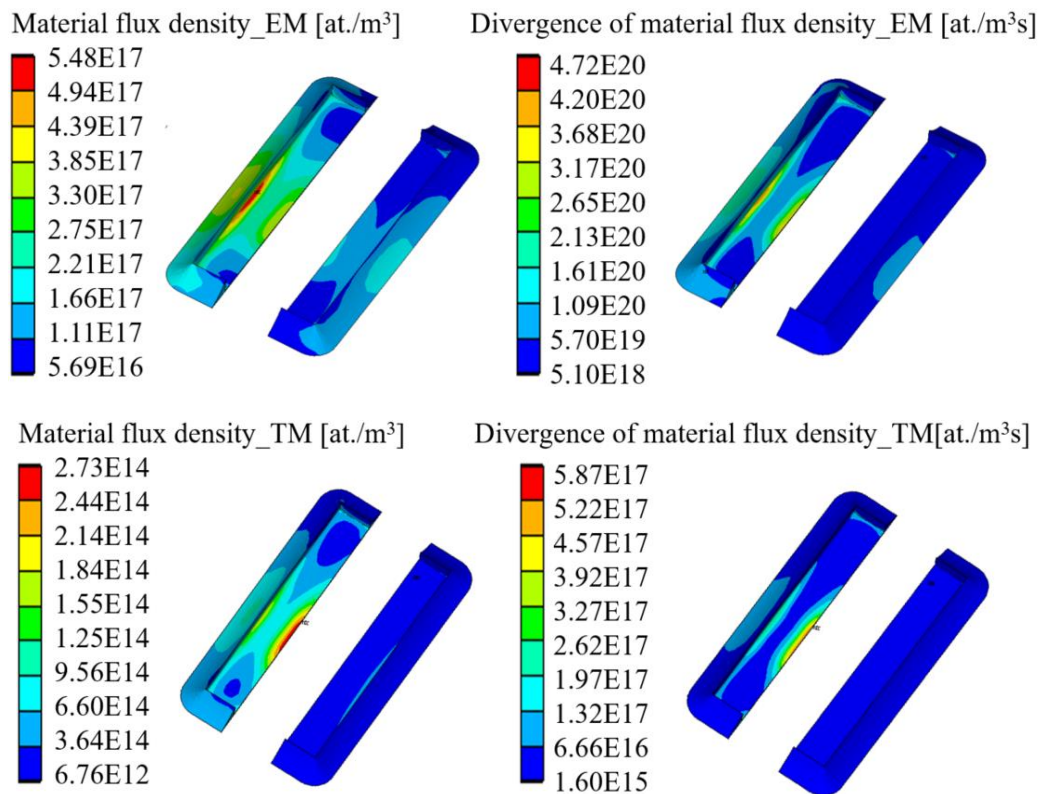


Fig. 5.27: Electromigration and thermomigration of solder joints of shunt A* (test Nr. 11, 3 mΩ, 45 A @2 s, 90 °C)

The EM-induced divergence material flux is evaluated by VWA method and the overview of other test conditions are listed in Table 5.11. The diffusion parameters shown in Table 5.8 are utilized for the simulation. The concentration of Cu in solder with Ni plating is derived via the analysis of IMC growth in section 4.3.2. It is noted that shunt A* without Ni plating exhibits significantly higher divergence of material flux density in the solder joint than shunt A with Ni plating under the same loading condition. This indicates excessive material transport in shunt A* under current stressing and explains the earlier failure of shunt A*.

Table 5.11: Electromigration simulation result of shunt A (3mΩ) and shunt A*

Test	Plating	VWA divergence of material flux density [at./m ³ ·s]
9	Ni/Sn	1.17E20
10	Ni/Sn	5.67E19
11	Sn	1.73E20
12	Sn	7.54E19

(3) Simulation of void formation

The effect of EM-induced void formation on the interconnect reliability is further investigated via voids simulation. The evolution of atomic density N with respect to testing time t can be calculated by the total divergence of material flux $\text{div}(\overrightarrow{J_{total}})$, as described by (5.2).

$$\text{div}(\overrightarrow{J_{total}}) + \frac{\partial N}{\partial t} = 0 \quad (5.2)$$

The criterion for void formation is defined by a reduction of the local atomic concentration to 85% of the initial concentration [123]. The elements fulfilling the criterion are selected into a cluster. The stiffness of the elements in the cluster is reduced in the structural analysis so that the elements act as voids [124]. The procedure for the simulation of void formation is displayed in Fig. 5.28 [124].

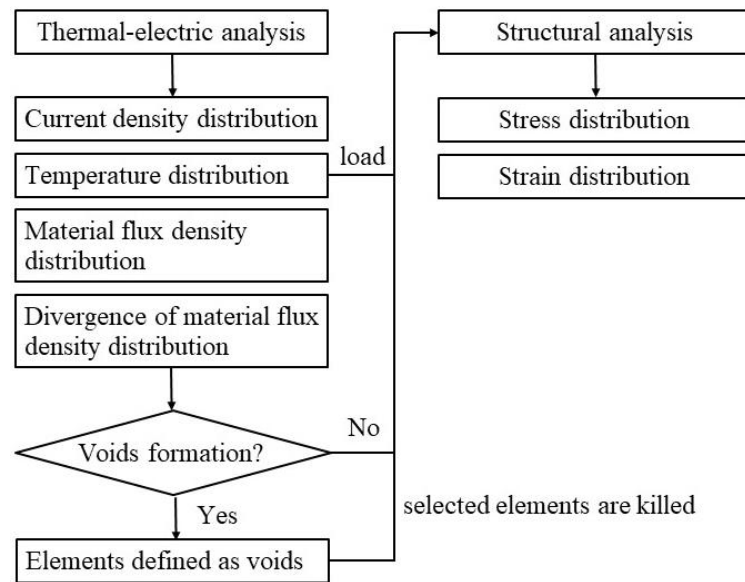


Fig. 5.28: Procedure for simulation of void formation [124]

In this work, the EM-induced material transport is the dominant migration phenomenon. Therefore, the EM-induced divergence of material flux is evaluated to calculate the local atomic density of solder material. The void formation in the solder joint of shunt A* at different power cycles is simulated and presented in Fig. 5.29. The distribution of accumulated plastic strain in the evolved geometry is also displayed. The number of elements which are defined as voids at a different testing stages is listed in Table 5.12. The corresponding volume weighted averaged (VWA) accumulated plastic strain is specified. No large void formation or change in accumulated plastic strain is detected after 5000 PCs, which agrees with the SEM analysis in Fig. 4.25 (b). Few voids (1.12% volume fraction of solder joints) are generated after 10000 PCs, especially at the corner of the solder meniscus. This corresponds well with the voids and micro-cracks observed in

Fig. 4.25 (c). At 15000 PCs, significant material depletion (20.02% volume fraction of solder joints) occurs mainly at the solder meniscus and the accumulated plastic strain in the solder joint is significantly increased. The coalescence of voids in the simulation is comparable to the SEM analysis shown in Fig. 4.25 (d).

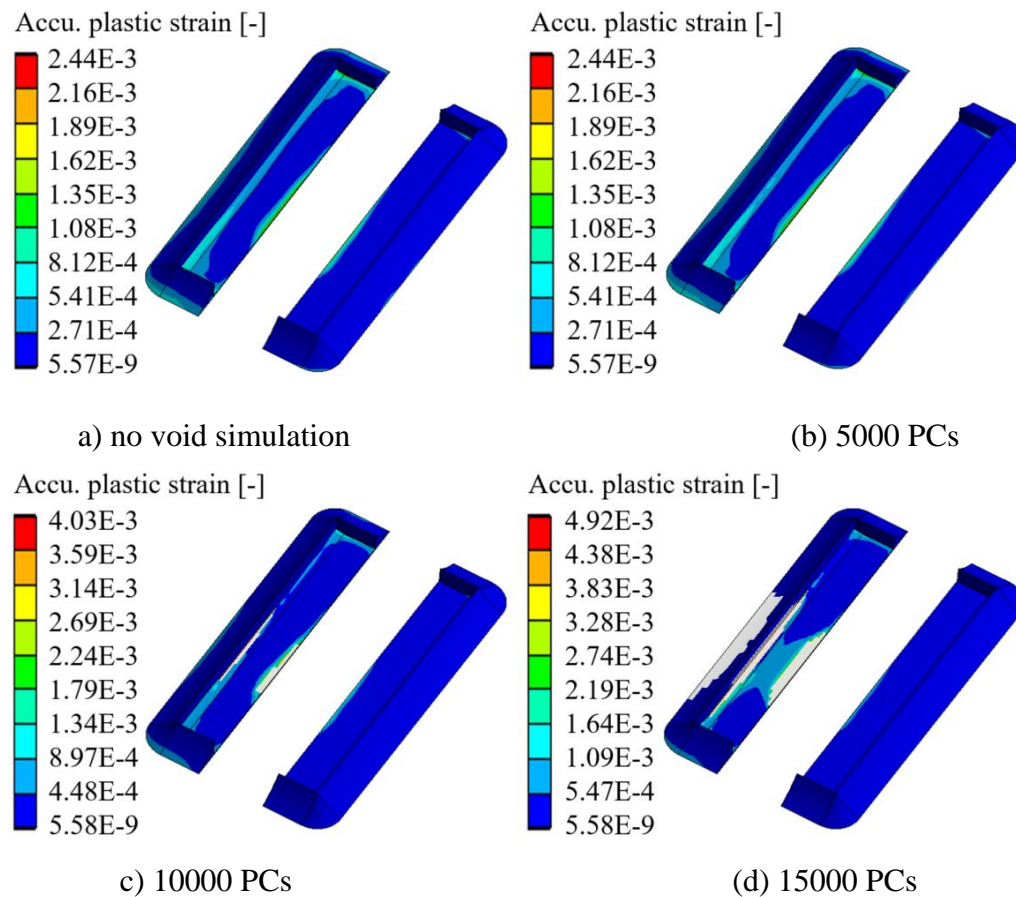


Fig. 5.29: Void formation in solder joint of shunt A* at different cycles [124]
(Test Nr. 11, current: 45A, pulse length: 2s, 90°C)

Table 5.12: Simulation of void formation for shunt A* at different cycles [124]

Power cycles	Nr. of void elements (volume fraction)	Max. accumulated plastic strain [-]	VWA accumulated plastic strain [-]
0	0 (0%)	2.44E-3	4.40E-4
5000	1 (0%)	2.44E-3	4.40E-4
10000	22 (1.12%)	4.03E-3	5,69E-4
15000	336 (20.02%)	4.92E-3	8,52E-4

5.3.3 Simulation of shunt B and shunt C

The same simulation procedure is conducted for shunts B and shunts C. Fig. 5.30 and Fig. 5.31

interpret the distribution of current density, temperature, normal stress and accumulated plastic strain in the solder joints under the representative test conditions for shunts B and for shunts C respectively. The shunt B is subjected to relatively low current density since the applied current is lower than for the other shunt components. The highest temperature is located at the solder standoff and the thermal gradient in the solder joint is small. The maximum normal stress and accumulated plastic strain are both located at the edge of the solder standoff. The distribution of all the simulation parameters in shunt C is similar to shunt B. The major difference is that the solder joint of shunt C undergoes higher current density and higher thermal gradient. The simulation results of other testing conditions of shunt B and shunt C are summarized in Table 5.13. The evaluation of the EM phenomenon of shunt B and shunt C are displayed in Fig. 5.32. Large influence of singularity at the edges of the solder joint is observed in shunt B. The VWA divergence of material flux, as listed in Table 5.13, shows that the risk for EM in shunt B is significantly lower than in shunt C. The maximum material flux density and divergence of material flux density in shunt C occur at the corner of the solder meniscus, which yields similar distribution as shunt A.

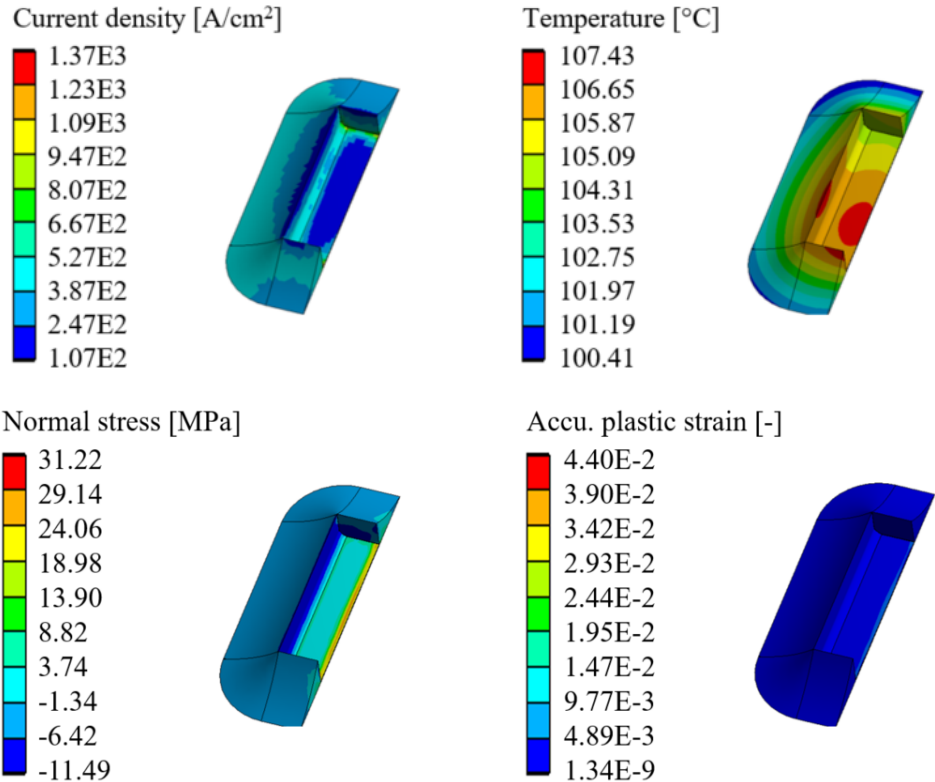


Fig. 5.30: Thermo-electrical-mechanical simulation results of shunt B (test Nr. 13: 30 mΩ, 10 A @ 1 s, 90 °C)

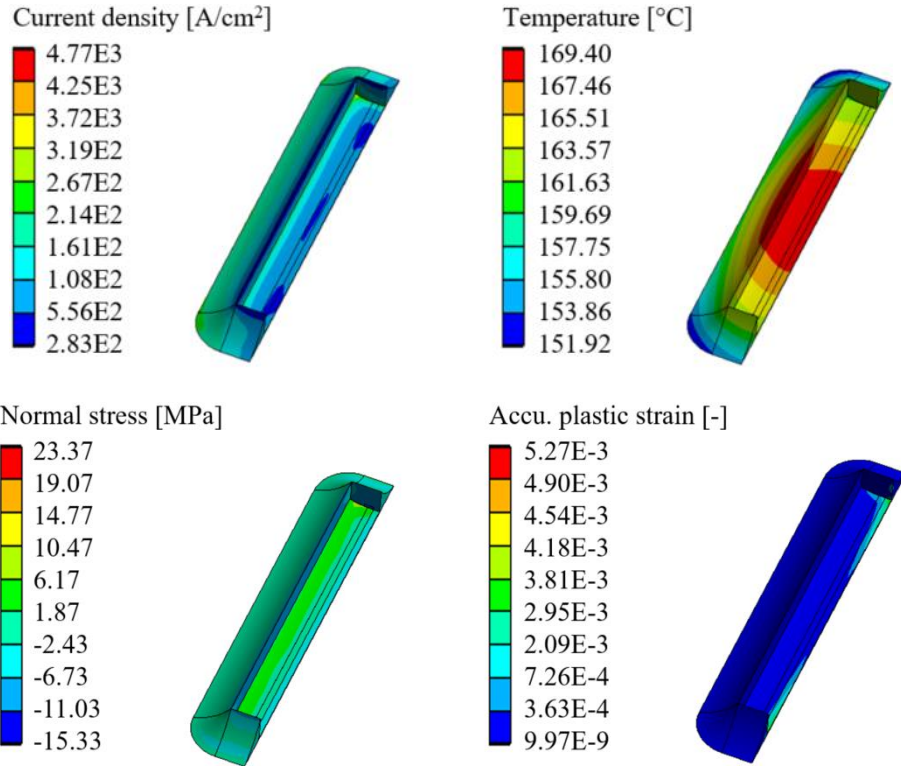
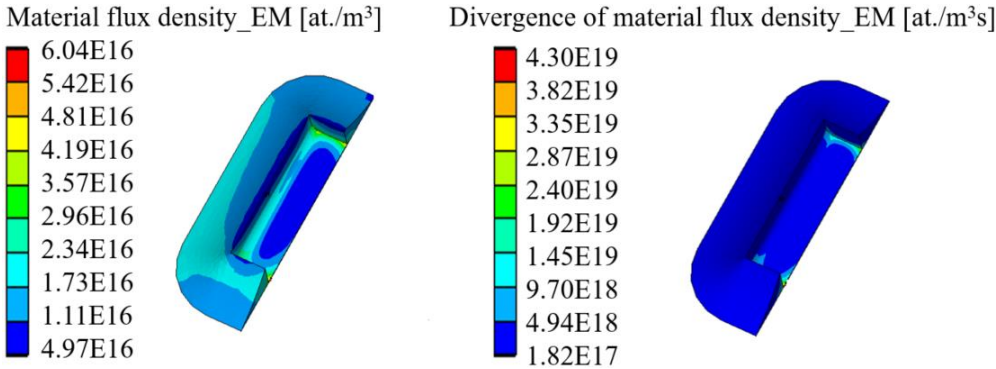
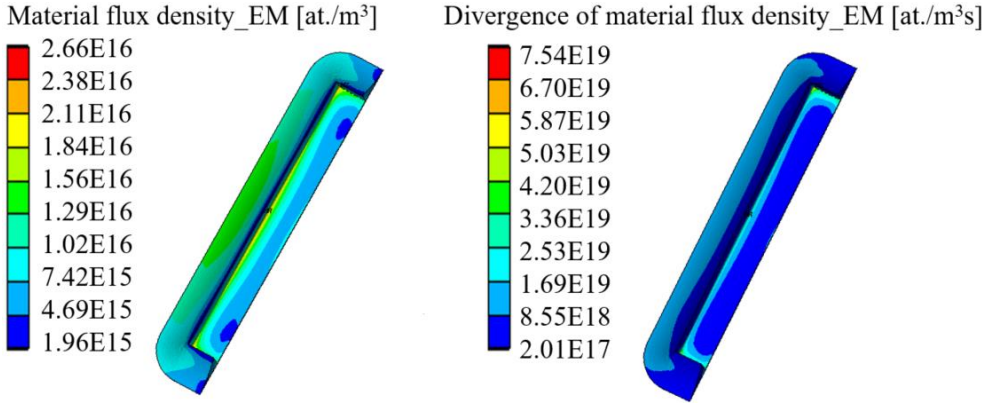


Fig. 5.31: Thermo-electrical-mechanical simulation results of shunt C (test Nr. 16, 3 mΩ, 42 A @3 s, 80 °C)



(a) shunt B (test Nr. 13)



(b) shunt C (test Nr. 16)

Fig. 5.32: Electromigration of solder joints of shunt B and shunt C

Table 5.13: Simulation results of shunt B and shunt C

Test	Max. current density [A/cm ²]	Max. temperature [°C]	Max. normal stress [MPa]	VWA accu. plastic strain [-]	VWA divergence of material flux density [at./m ³ ·s]
13	1.37E3	107.43	31.22	4.90E-4	1.86E16
14	1.21E3	101.24	17.89	8.07E-5	6.80E15
15	9.10E2	96.32	9.80	8.44E-6	1.81E15
16	4.78E3	169.21	23.1	2.16E-4	9.01E19
19	5.11E3	172.24	26.8	3.60E-4	1.13E20

The discussed simulation results exhibit the thermal, electrical and structural fields in the assembly of shunts under the tested conditions. Accumulated plastic strain and divergence of material flux density are normally used to characterize the failure mechanism of thermo-mechanical fatigue and electromigration respectively. As emphasized in chapter 2, these two failure mechanisms can dominate the failure of the solder joints under current loads. The damage parameters will be further investigated with the experimental findings in the following chapter.

6 Lifetime model

This chapter presents the summary of the statistical lifetime data from the tests. The failure modes analyzed in chapter 4 and the corresponding simulations discussed in chapter 5 will be compared and investigated. A lifetime model will be proposed based on the experimental and numerical results, which enables the lifetime prediction for future products and test conditions.

6.1 Lifetime data evaluation

The test results are summarized in Table 6.1. Test Nr. 1 and Test Nr. 2 lack sufficient statistical data. Most of the test conditions contain 30 measurement channels and each channel consists of the daisy chain of 5 components. In some tests with less critical loading conditions, there is no failure or limited failure detected until the end of the test.

Table 6.1: Overview of test results

Test number	Shunt	Resistance (mΩ)	Measurement channels	Failed channels
1			5	5
2			5	5
3			30	30
4			30	30
5		5	30	0
6	A		30	30
7			30	18
8			30	11
9			30	29
10		3	20	18
11			30	30
12	A*	3	10	10
13			30	30
14	B	30	30	29
15			30	14
16			30	27
17			30	0
18	C	3	30	0
19			30	28

The lifetime data specified in Table 6.1 are further analyzed with the three-parameter Weibull distribution. Many pseudo-failures occur at the same power cycles during the test of shunt B. This might be caused by the interference of measuring software. The test runs with sufficient lifetime data of shunt A (5 mΩ), shunt A (3 mΩ) and shunt A* (3 mΩ), shunt B and shunt C are statistically evaluated and their Weibull plots are shown in Fig. 6.1, Fig. 6.2, Fig. 6.3 and Fig. 6.4, respectively. The parameters of the Weibull distribution are illustrated in Table 6.2. The slope parameter characterizes the failure mode of the specimens. It is observed that the slope parameters vary from 1.0 to 2.5, which might be explained by the complex failure mode of TMF and EM. Other lifetime parameters are also listed in Table 6.2 for further comparison. Failure-free time specifies the operation time before the first failure occurs, MTTF and characteristic lifetime denote when 50% and 67.3% of the specimens fail.

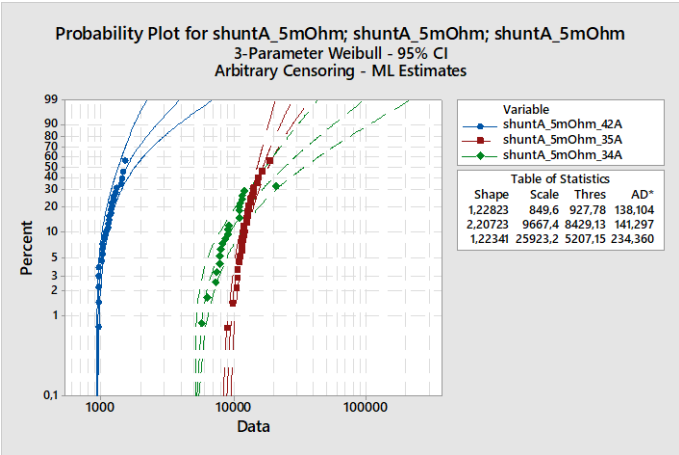


Fig. 6.1: Weibull analysis of shunt A (5 mΩ)

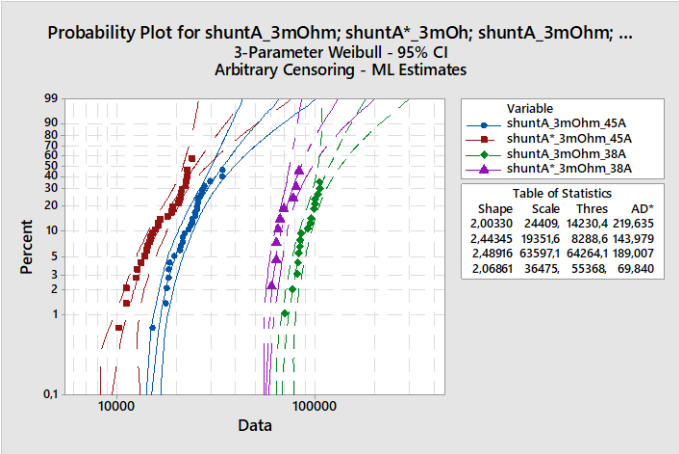


Fig. 6.2: Weibull analysis of shunt A (3 mΩ) and shunt A* (3 mΩ)

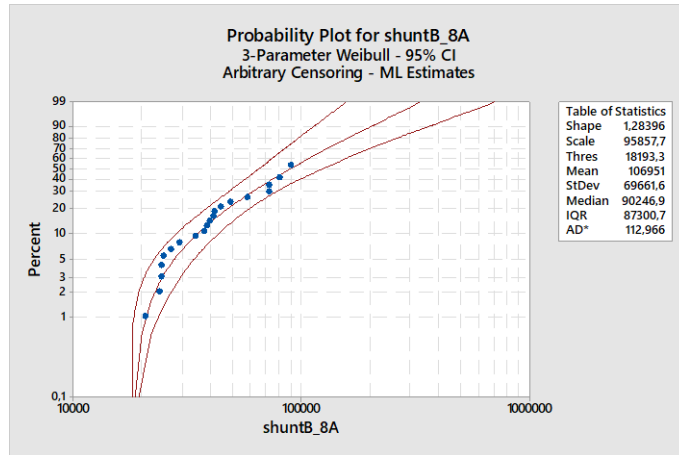


Fig. 6.3: Weibull analysis of shunt B (30 mΩ)

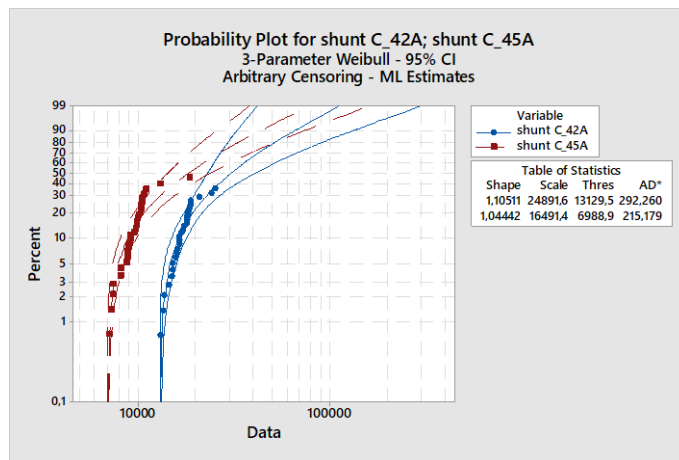


Fig. 6.4: Weibull analysis of shunt C (3 mΩ)

Table 6.2: Lifetime parameters of the Weibull distribution

Test number	Shunt	Resistance (mΩ)	Slope β	Scale parameter η	Failure-free time γ	MTTF
1			-	-	-	4200
2			-	-	-	10000
3		5	1.228	850	928	1723
4	A		2.207	9667	8429	16990
6			1.223	25923	5207	29474
9			2.000	24409	14230	35862
10		3	2.489	63597	64264	120685
11			2.440	19352	8289	25500
12	A*	3	2.069	36475	55368	87678
14	B	30	1.284	95858	18193	106951
16			1.105	24892	13130	37111
19	C	3	1.044	16491	6989	23196

6.2 Failure mode and damage parameter

A suitable damage parameter is required to describe the failure mode of the solder joints and correlate the local stress to the tested lifetime data. The dominant failure mechanism of shunt A under power cycling load is recrystallization-assisted crack nucleation and propagation. As highlighted in Fig. 6.5, the crack initiates from the edge of the solder standoff and the corner of the solder meniscus. The cracks propagate along the grain boundaries and later join into a large crack through the whole solder joint. The maximal accumulated plastic strain is located at the edge of the solder standoff and corresponds well with the crack initiation location. Apart from thermo-mechanical fatigue, EM also degrades the solder joint. It can be verified by the damage at the corner of the solder meniscus, where the maximal divergence of material of flux due to EM is located.

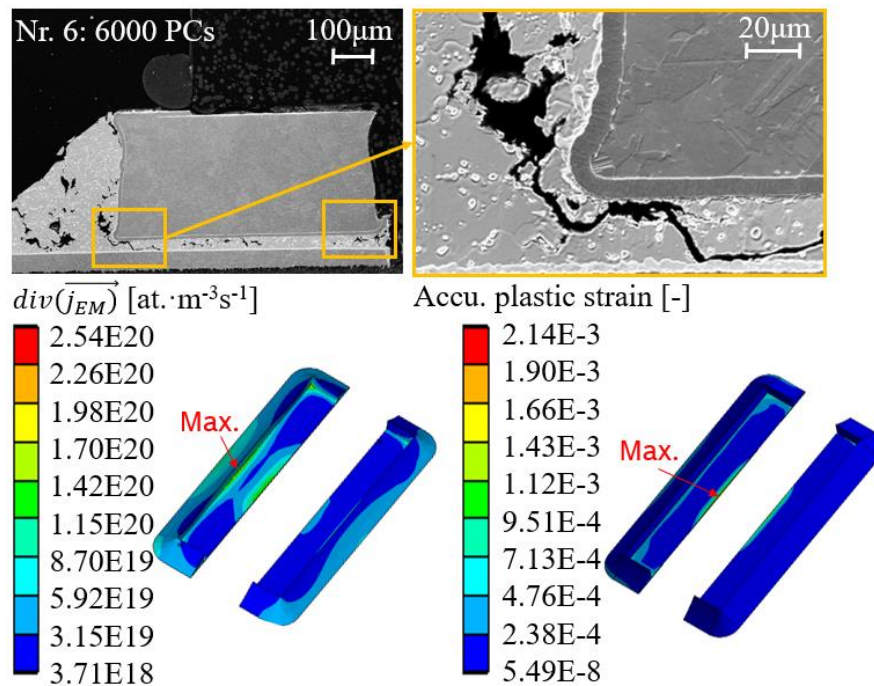


Fig. 6.5: Failure mode and damage parameter of shunt A (test Nr. 6: 5 mΩ)

The contribution of TMF and EM to the solder failure is further investigated by comparing shunt A (3 mΩ) and shunt A*. As displayed in Fig. 6.6, cracks initiate and grow at the corner of the solder meniscus and at the edge of the solder standoff of shunt A (3 mΩ), which agrees to the location of maximum divergence material flux density and maximum accumulated plastic strain respectively. The shunt A (3 mΩ) and shunt A* undergo the same electrical and thermal loads as well as the same resultant thermo-mechanical loads, as illuminated in section 5.3.2. However, the EM-induced degradation in shunt A* is enhanced due to the removal of the diffusion barrier. Therefore, the enhanced EM leads to the earlier failure of shunt A*. Fig. 6.7 presents the void formation observed in the solder joint of shunt A* and the simulation results at the same power

cycles. It is noted that the void simulation corresponds well with the SEM analysis and could interpret the increment of accumulated plastic strain and the earlier failure of shunt A*.

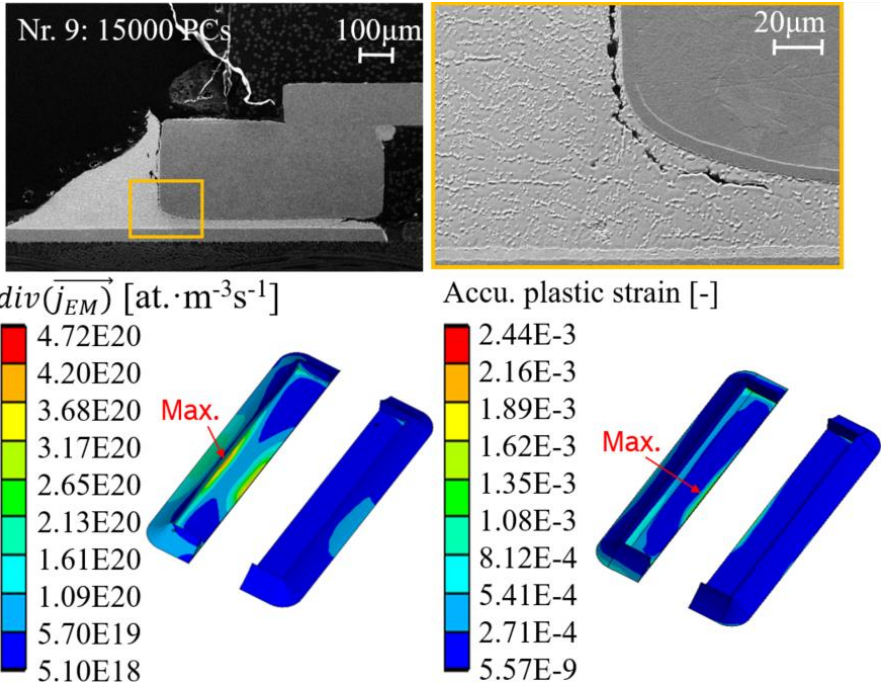


Fig. 6.6: Failure mode and damage parameter of shunt A (test Nr. 9: 3 mΩ)

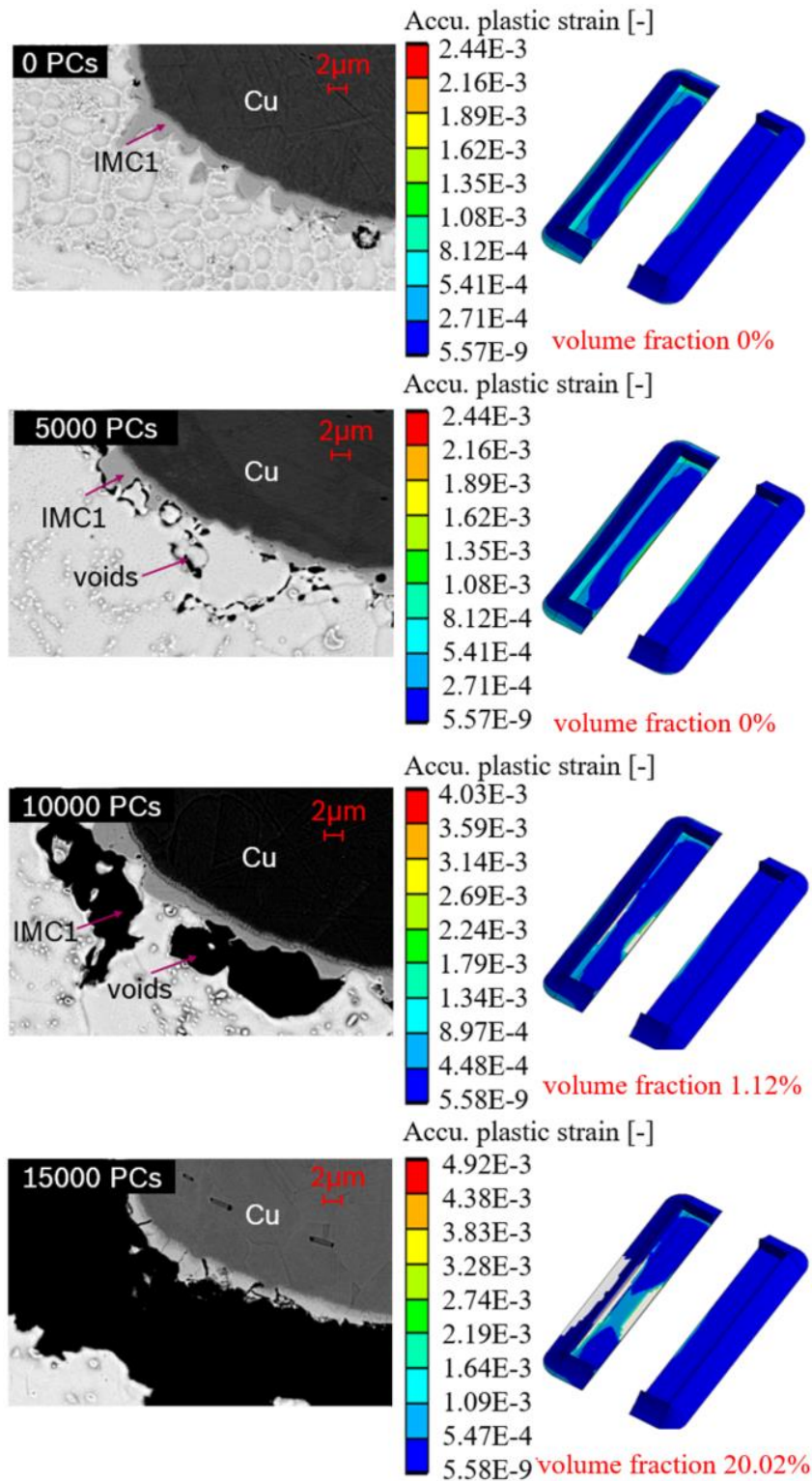


Fig. 6.7: Void formation and void simulation of shunt A* (test Nr. 11: 3 mΩ)

TMF is the dominate failure mechanism in solder joints of shunt B and shunt C, as shown in Fig. 6.8 and Fig. 6.9. The crack initiates from the edge of the solder standoff and agrees with the location of maximal accumulated plastic strain. Solder joints of shunt B undergo little risk for EM, owing to the low current density. The solder joints of shunt C are subjected to higher divergence of material flux density and the maximum material transport takes place at the corner of the solder

meniscus, which is similar to shunt A. However, it is difficult to differentiate the contribution of both failure mechanisms since no obvious void formation is detected.

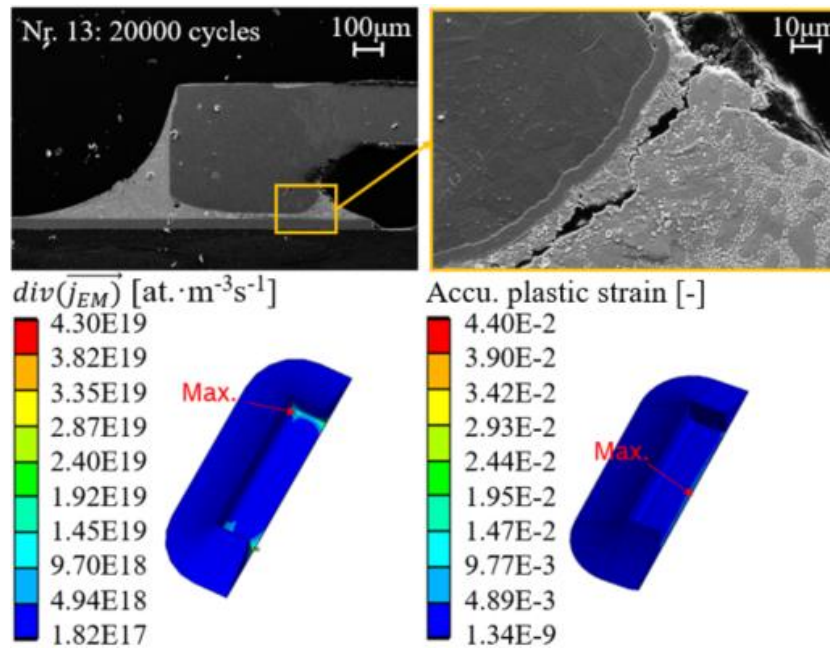


Fig. 6.8: Failure mode and damage parameter of shunt B (test Nr. 13: 30 mΩ)

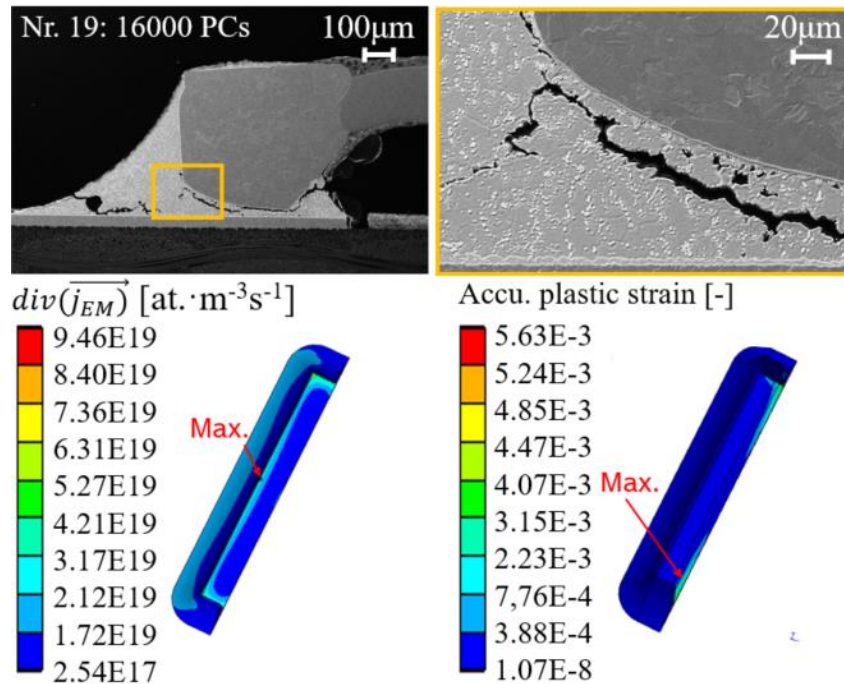


Fig. 6.9: Failure mode and damage parameter of shunt C (test Nr. 19: 3 mΩ)

The discussed damage parameters of the test conditions are summarized and exhibited in Fig. 6.10. The bars display the contribution of thermo-mechanical fatigue and the dotted line shows the risk for EM. It is observed that, most of the test conditions subjected to large thermo-mechanical load, are also exposed to a severe EM phenomenon. The higher the current density, the higher is the thermal load on the assembly. Therefore, the tendency of the damage parameter of the TMF failure

mechanism is similar to that of the EM failure mechanism. The solder joint of test Nr. 6 undergoes less accumulated plastic strain than test Nr. 4, even the amount of divergence of material flux density is higher. This is owing to the higher ambient temperature in test Nr. 6 and EM is highly activated by temperature. The green bars depict the damage parameter of shunt A (3 mΩ) with different plating. Even though the accumulated plastic strain is the same under the same loading conditions, the EM-induced degradation is performing differently due to the impact of the plating. The EM-induced degradation results in the earlier failure of test Nr. 11 and test Nr. 12, compared to test Nr. 9 and test Nr. 10. The simulated formation of voids and the voids observed in SEM analysis can verify the EM-induced degradation.

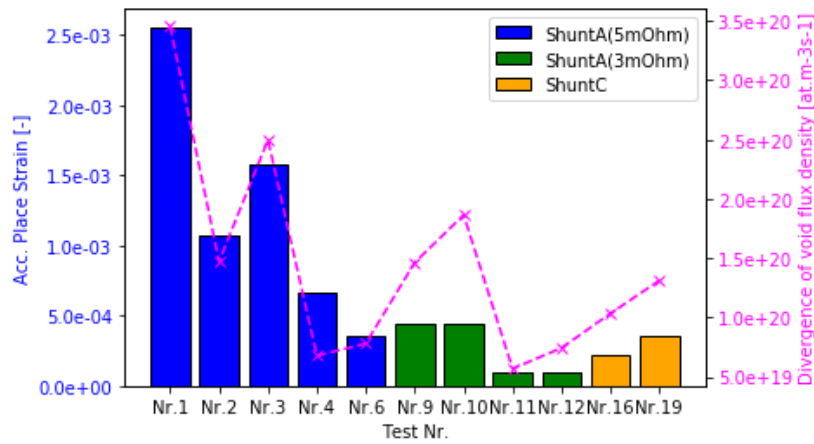


Fig. 6.10: Damage parameters of various test conditions

6.3 Derivation of lifetime model

When only thermo-mechanical fatigue is taken into account, the Coffin-Manson model is extensively implemented. The correlation of lifetime data (MTTF) and the accumulated plastic strain ε_{acc}^{pl} can be described by (6.1)

$$mttf = a * (\varepsilon_{acc}^{pl})^b \quad (6.1)$$

where a and b are fitting constants of the model.

Based on the experimental observations in this work, the coupling of thermo-mechanical fatigue and EM leads to the failure of solder joints under high current pulses. An additional term is proposed to modify the Coffin-Manson model to take the complex failure mechanism into account, as described in (6.2).

$$mttf = a * (\varepsilon_{acc}^{pl})^b y^c \quad (6.2)$$

where y is the product of the divergence of the material flux density and the pulse length of the current load, which characterizes the weakening of solder joints owing to EM. The damage parameters evaluated in Fig. 6.10 and the lifetime data analyzed in Table 6.2 are fitted to derive

the parameters of the model. The data-fitting is shown in Fig. 6.11 and the parameters are listed in Table 6.3. The data of test Nr. 1 and test Nr. 2 are displayed in the plot, while not included in the data-fitting process due to the insufficient statistics. The fitting parameter of R^2 is very close to 1, which indicates the high precision of the fitting model. The dotted red line indicates $\pm 25\%$ accuracy of the fitting model.

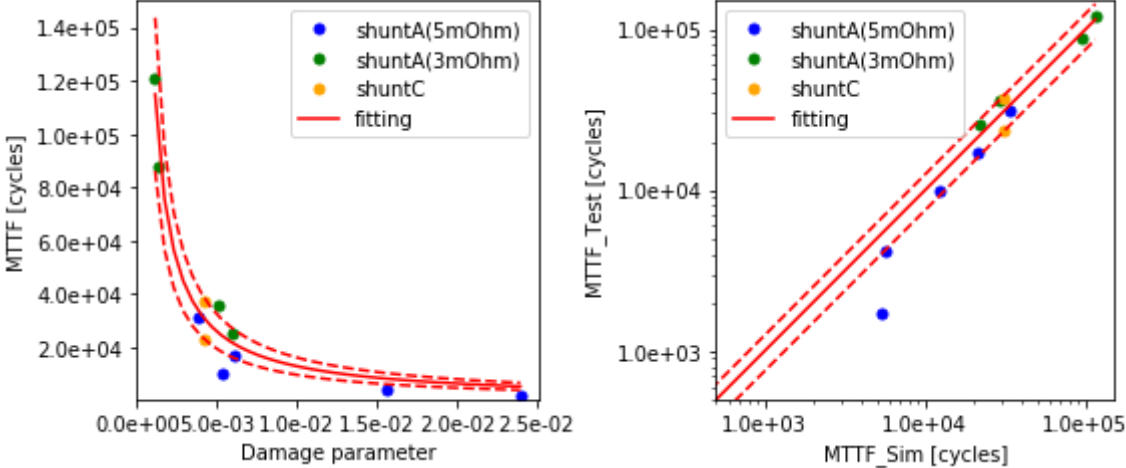


Fig. 6.11: Fitting of lifetime model

Table. 6.3: Fitting parameters of lifetime

a	b	c	R^2
126.119	-0.578	-0.684	0.967

Fig. 6.9 presents a direct comparison of the lifetime obtained from tests and derived from the model. Except for test Nr. 3, the proposed lifetime model predicts the lifetime of different components within $\pm 25\%$ accuracy. The discrepancy of the test result and model prediction of test Nr. 3 could be explained by the overstressing condition. As shown in Fig. 6.10, the mold material (resin) of shunt A melts after the test Nr. 3 due to the critical loading condition. Therefore, the reduced lifetime in the test might result from the overload and component damage.

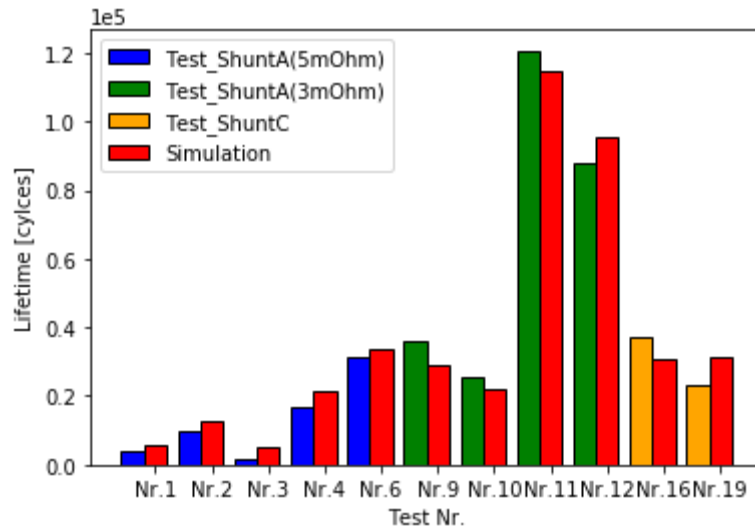


Fig. 6.12: Comparison of test lifetime and model prediction

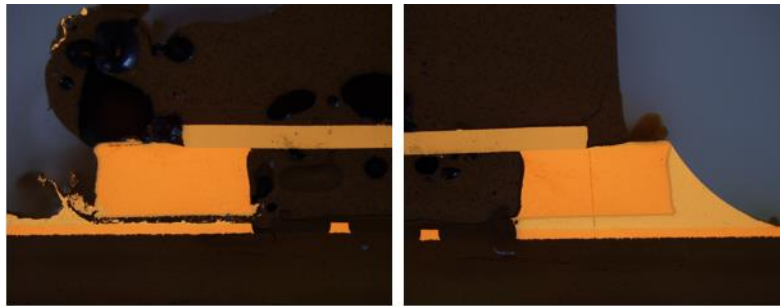


Fig. 6.13: Overstressed shunt A ($5\text{ m}\Omega$) under test Nr. 3

It can be concluded that the solder failure occurs under high current pulses owing to the coupling of EM-induced degradation of solder and TMF. The EM phenomenon is more dominant in shunt A than shunt B and shunt C. Based on the understanding of the failure mechanism, a new lifetime model is proposed to evaluate the lifetime of solder joints of shunts subjected to high current loading conditions. The damage parameter in the model considers the contributions of TMF and EM to the failure. This model can serve to assess the reliability of the assembly of other shunt components with similar configurations and to predict service life for other high current loading conditions.

7 Summary and outlook

In this work, the performance of solder interconnects (SAC 405) exposed to field-like current loads has been investigated experimentally and numerically. Shunt components are selected for the study due to their simple configuration and relatively high service life. Various loading conditions with different current range, pulse length and ambient temperature have been tested. Online electrical measurement has been performed to detect the failure of the assembly. Failure occurs in the solder joints under the power cycling tests, which reproduces the failure detected in the field conditions.

Failure analysis methods such as light microscopy, SEM/EDS and CT scanning have been carried out on the specimens at different testing stages. In the assembly of shunt A, failure takes place at the terminal side which is connected to the anode of the power supply. While there is no polarity effect in the failure modes of shunt B and shunt C. This observation agrees with the self-heating behavior of the shunts. In shunt A, extra heat generation and loss occurs at the interface between the resistive element and the terminal owing to the Peltier effect. The self-heating of shunt B and shunt C is symmetric since the resistive element and the terminals are joint via a fused zone.

The microstructural evolution of the solder material subjected to high current loads is analyzed thoroughly to study the failure mechanism. In shunt A, formation of voids is observed at the anode side of the solder meniscus, which serves as an indicator for EM. Crack initiation and propagation take place at the edge of the solder standoff and the corner of the solder meniscus. The cracks join later to form a complete crack through the solder joint, resulting in final electrical failure. In shunt B and shunt C, crack formation starts from the solder standoff and proceeds through the solder joint. Recrystallization and coarsening of Ag_3Sn precipitates are observed after current stressing. The microstructural evolution weakens the solder joints and provides favorable sites for crack initiation.

To further identify the contribution of EM to the failure, shunt A (3 m Ω) and shunt A* (3 m Ω) without diffusion barrier are investigated. The IMC formed in shunt A (3 m Ω) only consists of $(\text{Cu}, \text{Ni})_6\text{Sn}_5$. The IMC formed in shunt A* (3 m Ω) is mainly composed of Cu_6Sn_5 with a thin layer of Cu_3Sn . With current stressing, a polarity effect of IMC growth is detected. The thickness of IMC2 on PCB side (anode locally) grows linearly with respect to stressing time, while the thickness of IMC1 on component side (cathode locally) decreases. This verifies the material transport due to EM. To investigate the correlation between EM-induced degradation of solder and grain orientations of the Sn matrix, EBSD analysis has been conducted on shunt A*. It is observed that the crack in the solder standoff propagates along the LAGBs, which agrees with the TMF failure mode. The void-like damage at the corner of the solder meniscus takes place at the

IMC/solder interface when the c-axis of β -Sn is parallel to the electron direction. When the c-axis of β -Sn is perpendicular to the electron direction, the damage is located in the solder. This could be explained by the correlation of Sn grain orientation and the dominant diffusant of EM.

To describe the above experimental observations, simulation models of the shunt assembly are generated and FEM analysis is conducted for the test conditions. Current distribution, thermal gradient and the resultant thermo-mechanical stress in the solder joints are obtained via electrical-thermal-structural simulation. Current is distributed symmetrically in the assembly. The solder joint of shunt A undergoes higher temperature at anode side, taking the Peltier effect into account. The heat distribution of the simulation models has been validated with the thermal measurements. The maximum thermo-mechanical stress and accumulated plastic strain locate at the solder standoff, which corresponds with the recrystallization and the formation of LAGBs observed in SEM and EBSD analysis. The divergence of material flux density has been evaluated as well to investigate the risk for the migration phenomenon. In shunt A, the maximum divergence of material flux density due to EM takes place at the corner of the solder meniscus, where the formation of voids is detected. The void formation at different stressing stages has been further simulated and the simulated void fraction shows good agreement with the SEM analysis. The accumulated plastic strain is significantly increased when coalescence of the voids occurs, which weakens the solder joints and reduces their lifetime.

Based on the experimental observations and numerical results, a lifetime model is derived to assess the reliability of solder joints of shunts subjected to high current loading conditions. The damage parameter consists of accumulated plastic strain and divergence of material flux density, which considers the contributions of both failure mechanisms and characterizes the observed complex failure modes. This work compensates the limitation of the reviewed lifetime models, which mainly discuss TMF or EM individually and cannot represent the field-relevant failure mode. Future studies can investigate the implementation of the lifetime model to shunts under operation mission profiles. Based on the understanding of the complex failure mechanisms of the solder joints in this work, future studies can further extend the model to combined loading conditions. The methodology can also be transferred to other component types, which often operate under high current loads and provide the lifetime prediction for products and technologies driven by electrification and miniaturization.

8 References

- [1] T. Scannell, „Autonomous vehicle technology is driving the need for increased speed and bandwidth in electronic connectors,“ 2017. [Online]. Available: <https://www.connectorsupplier.com/>. [accessed 2021].
- [2] Bosch, „Electric Power Steering (EPS),“ 2019. [Online]. Available: <https://www.bosch.com/de/>. [accessed 2021].
- [3] T.-K. Lee, T. Bieler, C.-U. Kim and H. Ma, Fundamentals of lead-free solder interconnect technology: From microstructures to reliability, Boston: Springer, 2015.
- [4] S. Hamasha, A. Qasaimeh, Y. Jaradat and P. Borgesen, „Correlation Between Solder Joint Fatigue Life and Accumulated Work in Isothermal Cycling,“ *IEEE Transactions on Components, Packaging and Manufacturing Technology*, Vol. 5, pp. 1292-1299, Sept. 2015.
- [5] S. Choi, K. N. Subramanian, J. P. Lucas and T. R. Bieler, „Thermomechanical fatigue behavior of Sn-Ag solder joints,“ *Journal of Electronic Materials*, Vol. 29, pp. 1249-1257, Oct. 2000.
- [6] J. G. Lee, A. Telang, K. N. Subramanian and T. R. Bieler, „Modeling thermomechanical fatigue behavior of Sn-Ag solder joints,“ *Journal of Electronic Materials*, Vol. 31, pp. 1152-1159, Nov. 2002.
- [7] H. Rhee, J. P. Lucas and K. N. Subramanian, „Micromechanical characterization of thermomechanically fatigued lead-free solder joints,“ *Journal of Materials Science: Materials in Electronics*, Vol. 13, pp. 477-484, Aug. 2002.
- [8] T. R. Bieler, H. Jiang, L. P. Lehman, T. Kirkpatrick, E. J. Cotts and B. Nandagopal, „Influence of Sn Grain Size and Orientation on the Thermomechanical Response and Reliability of Pb-free Solder Joints,“ *IEEE Transactions on Components and Packaging Technologies*, Vol. 31, pp. 370-381, Jun. 2006.
- [9] X. Li and Z. Wang, „Thermo-fatigue life evaluation of SnAgCu solder joints in flip chip assemblies,“ *Journal of Materials Processing Technology*, Vol. 183, pp. 6-12, Mar. 2007.
- [10] J. J. Sundelin, S. T. Nurmi and T. K. Lepistö, „Recrystallization behaviour of SnAgCu solder joints,“ *Materials Science and Engineering: A*, Vol. 474, pp. 201-207, Feb. 2008.
- [11] J. G. Lee and K. N. Subramanian, „Effect of dwell times on thermomechanical fatigue behavior of Sn-Ag-based solder joints,“ *Journal of Electronic Materials*, Vol. 32, pp. 523-530, Jun. 2003.
- [12] K. N. Subramanian, „A parametric approach for assessment of thermomechanical fatigue performance of Sn-based solder joints,“ *Journal of Electronic Materials*, Vol. 34, pp. 1313-1317, Oct. 2005.
- [13] T. T. Mattila and J. K. Kivilahti, „The Role of Recrystallization in the Failure of SnAgCu Solder Interconnections Under Thermomechanical Loading,“ *IEEE Transactions on Components and Packaging Technologies*, Vol. 33, pp. 629-635, Sep. 2010.
- [14] D. W. Henderson, J. J. Woods, T. A. Gosselin, J. Bartelo, D. E. King, T. M. Korhonen, M. A. Korhonen, L. P. Lehman, E. J. Cotts, S. K. Kang, P. Lauro, D.-Y. Shih, C. Goldsmith and K. J. Puttlitz, „The microstructure of Sn in near-eutectic Sn-Ag-Cu alloy solder joints and its role in thermomechanical fatigue,“ *Journal of Materials Research*, Vol. 19, pp. 1608-1612, 2004.

- [15] A. U. Telang, T. R. Bieler, A. Zamiri and F. Pourboghrat, „Incremental recrystallization/grain growth driven by elastic strain energy release in a thermomechanically fatigued lead-free solder joint,“ *Acta Materialia*, Vol. 55, pp. 2265-2277, Apr. 2007.
- [16] P. Borgesen, L. Wentlent, S. Hamasha, S. Khasawneh, S. Shirazi, D. Schmitz, T. Alghoul, C. Greene and L. Yin, „A Mechanistic Thermal Fatigue Model for SnAgCu Solder Joints,“ *Journal of Electronic Materials*, Vol. 47, pp. 2526-2544, May 2018.
- [17] L. Yin, L. Wentlent, L. Yang, B. Arfaei, A. Oasaimh and P. Borgesen, „Recrystallization and Precipitate Coarsening in Pb-Free Solder Joints During Thermomechanical Fatigue,“ *Journal of Electronic Materials*, Vol. 41, pp. 241-252, Feb. 2012.
- [18] Y. Yao, L. M. Keer and M. E. Fine, „Modeling the failure of intermetallic/solder interfaces,“ *Intermetallics*, Vol. 18, pp. 1603-1611, Aug. 2010.
- [19] G. Zeng, S. Xue, L. Zhang, L. Gao, W. Dai and J. Luo, „A review on the interfacial intermetallic compounds between Sn-Ag-Cu based solders and substrates,“ *Journal of Materials Science: Materials in Electronics*, Vol. 21, pp. 421-440, May 2010.
- [20] K. E. Yazzie, H. X. Xie, J. J. Williams and N. Chawla, „On the relationship between solder-controlled and intermetallic compound (IMC)-controlled fracture in Sn-based solder joints,“ *Scripta Materialia*, Vol. 66, pp. 586-589, Apr. 2012.
- [21] F. X. Che and J. H. L. Pang, „Characterization of IMC layer and its effect on thermomechanical fatigue life of Sn-3.8Ag-0.7Cu solder joints,“ *Journal of Alloys and Compounds*, Vol. 541, pp. 6-13, Nov. 2012.
- [22] J. H. L. Pang, T. H. Low, B. S. Xiong, X. Luhua and C. C. Neo, „Thermal cycling aging effects on Sn-Ag-Cu solder joint microstructure, IMC and strength,“ *Thin Solid Films*, Vol. 462-463, pp. 370-375, Sep. 2004.
- [23] N. Chawla, „Thermomechanical behaviour of environmentally benign Pb-free solders,“ *International Materials Reviews*, Vol. 54, pp. 368-384, Nov. 2009.
- [24] T. An and F. Qin, „Dynamic fracturing of the intermetallic compound layer in solder joints under impact drop loading,“ *Acta mechanica Solida Sinica*, Vol. 34, pp. 117-124, Apr. 2013.
- [25] D. A. Shnawah, M. F. M. Sabri and I. A. Badruddin, „A review on thermal cycling and drop impact reliability of SAC solder joint in portable electronic products,“ *Microelectronics Reliability*, Vol. 52, pp. 90-99, Jan. 2012.
- [26] J. Mehrmashhadi, Y. Tang, X. Zhao, Z. Xu, J. J. Pan, Q. V. Le and F. Bobaru, „The Effect of Solder Joint Microstructure on the Drop Test Failure--A Peridynamic Analysis,“ *IEEE Transactions on Components, Packaging and Manufacturing Technology*, Vol. 9, pp. 58-71, Jan. 2019.
- [27] T. T. Mattila and J. K. Kivilahti, „Failure mechanisms of lead-free chip scale package interconnections under fast mechanical loading,“ *Journal of Electronic Materials*, Vol. 34, pp. 969-976, Jul. 2005.
- [28] M. Alajoki, L. Nguyen and J. Kivilahti, „Drop test reliability of wafer level chip scale packages,“ in *Proceedings Electronic Components and Technology*, pp.637-644, 2005.

- [29] T. T. Nguyen and S. Park, „Characterization of elasto-plastic behavior of actual SAC solder joints for drop test modeling,“ *Microelectronics Reliability*, Vol. 51, pp. 1385-1392, Aug. 2011.
- [30] F. Qin, T. An and N. Chen, „Strain Rate Effects and Rate-Dependent Constitutive Models of Lead-Based and Lead-Free Solders,“ *Journal of Applied Mechanics*, Vol. 77, pp. 1008, Jan. 2010.
- [31] E. H. Wong, C. Selvanayagam, S. K. W. Seah, W. Driel, J. F. J. M. Caers, X. J. Zhao, N. Owens, L. C. Tan, D. Frear, M. Leoni, Y.-S. Lai and C.-L. Yeh, „Stress-Strain Characteristics of Tin-Based Solder Alloys for Drop-Impact Modeling,“ *Journal of Electronic Materials*, Vol. 37, pp. 829-836, Mar. 2008.
- [32] P. Darbandi, T. R. Bieler, F. Pourboghrat and T.-k. Lee, „The Effect of Cooling Rate on Grain Orientation and Misorientation Microstructure of SAC105 Solder Joints Before and After Impact Drop Tests,“ *Journal of Electronic Materials*, Vol. 43, pp. 2521-2529, Jul. 2014.
- [33] W. Liu and N.-C. Lee, „The effects of additives to SnAgCu alloys on microstructure and drop impact reliability of solder joints,“ *Journal of The Minerals, Metals & Materials Society*, Vol. 59, pp. 26-31, Jul. 2007.
- [34] D. Suh, D. W. Kim, P. Liu, H. Kim, J. A. Weninger, C. M. Kumar, A. Prasad, B. W. Grimsley and H. B. Tejada, „Effects of Ag content on fracture resistance of Sn-Ag-Cu lead-free solders under high-strain rate conditions,“ *Materials Science and Engineering: A*, Vol. 460-461, pp. 595-603, Jul. 2007.
- [35] F. Liu and G. Meng, „Random vibration reliability of BGA lead-free solder joint,“ *Microelectronics Reliability*, Vol. 54, pp. 226-232, Jan. 2014.
- [36] D. Yu, A. Al-Yafawi, T. T. Nguyen, S. Park and S. Chung, „High-cycle fatigue life prediction for Pb-free BGA under random vibration loading,“ *Microelectronics Reliability*, Vol. 51, pp. 649-656, Mar. 2011.
- [37] Y. S. Chen, C. S. Wang and Y. J. Yang, „Combining vibration test with finite element analysis for the fatigue life estimation of PBGA components,“ *Microelectronics Reliability*, Vol. 48, pp. 638-644, Apr. 2008.
- [38] K. Meier, M. Roellig, A. Schiessl and K. Wolter, „Life time prediction for lead-free solder joints under vibration loads,“ in *12th Intl. Conf. on Thermal, Mechanical & Multi-Physics Simulation and Experiments in Microelectronics and Microsystems*, pp. 1/8-8/8, 2011.
- [39] J. D. Wu, S. H. Ho, P. J. Zheng, C. C. Liao and S. C. Hung, „An experimental study of failure and fatigue life of a stacked CSP subjected to cyclic bending,“ in *Proceedings 51st Electronic Components and Technology Conference (ECTC)*, pp. 1081-1086, 2001.
- [40] D. T. Rooney, N. Todd Castello, M. Cibulsky, D. Abbott and D. Xie, „Materials characterization of the effect of mechanical bending on area array package interconnects,“ *Microelectronics Reliability*, Vol. 44, pp. 275-285, Feb. 2004.
- [41] I. Kim and S. Lee, „Reliability and Failure Analysis of Lead-Free Solder Joints for PBGA Package Under a Cyclic Bending Load,“ *IEEE Transactions on Components and Packaging Technologies*, Vol. 31, pp. 478-484, Jun. 2008.

- [42] L. L. Mercado, B. Phillips, S. Sahasrabudhe, J. P. Sedillo, D. Bray, E. Monroe, K. J. Lee and G. Lo, „Use-condition-based cyclic bend test development for handheld components,“ in *Proceedings 54th ECTC*, pp. 1279-1287, 2004.
- [43] K. Harada, S. Baba, Q. Wu, H. Matsushima, T. Matsunaga, Y. Ucgai and M. Kimura, „Analysis of solder joint fracture under mechanical bending test,“ in *Proceedings 53rd ECTC*, pp. 1731-1737, 2003.
- [44] B. Sabuncuoglu, F. Vanhee, G. Willems, B. Vandeveldel, D. Vandepitte and I. D. Wolf, „Finite element modeling of solder joint fatigue in four-point bending test,“ in *Proceedings 13th International Thermal, Mechanical and Multi-Physics Simulation and Experiments in Microelectronics and Microsystems*, pp. 1/7-7/7, 2012.
- [45] T. An, F. Qin and J. Li, „Mechanical behavior of solder joints under dynamic four-point impact bending,“ *Microelectronics Reliability*, Vol. 51, pp. 1011-1019, May 2011.
- [46] B. Sabuncuoglu, F. Vanhee, G. Willems, B. Vandeveldel and D. Vandepitte, „Evaluation of Fatigue Behavior of Lead-Free Solder Joints in Four-Point Bending Test by Finite-Element Modeling,“ *IEEE Transactions on Components, Packaging and Manufacturing Technology*, Vol. 7, pp. 1957-1964, Dec. 2017.
- [47] M. Nowotnick, A. Novikov, D. Seehase and C. Kronwald, „Comparison of Active and Passive Temperature Cycling,“ in *Proceedings SMTA International Conference*, pp. 99-104, 2016.
- [48] L. Xu, J. H. L. Pang and F. Che, „Impact of Thermal Cycling on Sn-Ag-Cu Solder Joints and Board-Level Drop Reliability,“ *Journal of Electronic Materials*, Vol. 37, pp. 880-886, Jun. 2008.
- [49] D. B. Barker, A. Dasgupta and M. G. Pecht, „PWB solder joint life calculations under thermal and vibrational loading,“ in *Proceedings Annual Reliability and Maintainability Symposium*, pp. 451-459, 1991.
- [50] J. H. L. Pang, F. L. Wong, K. T. Heng, Y. S. Chua and C. E. Long, „Combined vibration and thermal cycling fatigue analysis for SAC305 lead free solder assemblies,“ in *IEEE 63rd Electronic Components and Technology Conference*, pp. 1300-1307, 2013.
- [51] H. A. Chan, *Accelerated Stress Testing Handbook: Guide for Achieving Quality Products*, Wiley-IEEE Press, 2001.
- [52] D. Ghaderi, M. Pourmahdavi, V. Samavatian, O. Mir and M. Samavatian, „Combination of thermal cycling and vibration loading effects on the fatigue life of solder joints in a power module,“ *Proceedings of the Institution of Mechanical Engineers, Part L: Journal of Materials: Design and Applications*, Vol. 233, pp. 1753-1763, 2019.
- [53] H. Qi, M. Osterman and M. Pecht, „Modeling of Combined Temperature Cycling and Vibration Loading on PBGA Solder Joints Using an Incremental Damage Superposition Approach,“ *IEEE Transactions on Advanced Packaging*, Vol. 31, pp. 463-472, Aug. 2008.
- [54] T. Eckert, M. Krüger, W. H. Müller, N. F. Nissen and H. Reichl, „Investigation of the solder joint fatigue life in combined vibration and thermal cycling tests,“ in *Proceedings 60th Electronic Components and Technology Conference*, pp. 1209-1216, 2010.
- [55] F. Chai, „Solder Interconnect Life Prediction under Complex Temperature Cycling with Varying Mean and Amplitude,“ Dotoral dissertation, University of Maryland, 2013.

- [56] F. Chai, M. Osterman and M. Pecht, „Strain-Range-Based Solder Life Predictions Under Temperature Cycling With Varying Amplitude and Mean,“ *IEEE Transactions on Device and Materials Reliability*, Vol. 14, pp. 351-357, Mar. 2014.
- [57] Y. Chen, W. Men, Z. Yuan, R. Kang and A. Mosleh, „Nonlinear Damage Accumulation Rule for Solder Life Prediction Under Combined Temperature Profile With Varying Amplitude,“ *IEEE Transactions on Components, Packaging and Manufacturing Technology*, Vol. 9, pp. 39-50, Jan. 2019.
- [58] Y. Lai, T. H. Wang and C. Lee, „Thermal-Mechanical Coupling Analysis for Coupled Power- and Thermal-Cycling Reliability of Board-Level Electronic Packages,“ *IEEE Transactions on Device and Materials Reliability*, Vol. 8, pp. 122-128, Mar. 2008.
- [59] H.-C. Ma, J.-D. Guo, J.-Q. Chen, D. Wu, Z.-Q. Liu, Q.-S. Zhu, L. Zhang and H.-Y. Guo, „The reliability of copper pillar under the coupling of thermal cycling and electric current stressing,“ *Journal of Materials Science: Materials in Electronics*, Vol. 27, pp. 9748-9754, Sep. 2016.
- [60] Y. Zuo, L. Ma, S. Liu, T. Wang, F. Guo and X. Wang, „The coupling effects of thermal cycling and high current density on Sn58Bi solder joints,“ *Journal of Materials Science*, Vol. 48, pp. 2318-2325, Mar. 2013.
- [61] L. Ma, Y. Zuo, S. Liu, F. Guo and X. Wang, „The failure models of Sn-based solder joints under coupling effects of electromigration and thermal cycling,“ *Journal of Applied Physics*, Vol. 113, Jan. 2013.
- [62] Y. Zuo, T. R. Bieler, Q. Zhou, L. Ma and F. Guo, „Electromigration and Thermomechanical Fatigue Behavior of Sn_{0.3}Ag_{0.7}Cu Solder Joints,“ *Journal of Electronic Materials*, Vol. 47, pp. 1881-1895, Mar. 2018.
- [63] T. Laurila, T. Mattila, V. Vuorinen, J. Karppinen, J. Li, M. Sippola and J. K. Kivilahti, „Evolution of microstructure and failure mechanism of lead-free solder interconnections in power cycling and thermal shock tests,“ *Microelectronics Reliability*, Vol. 47, pp. 1135-1144, Jul. 2007.
- [64] J. Mei, R. Haug, O. Lanier, T. Grözinger and A. Zimmermann, „Effect of Joule heating on the reliability of solder joints under power cycling conditions,“ *Microelectronics Reliability*, Vol. 88-90, pp. 684-690, Sep. 2018.
- [65] I. Dutta, „A constitutive model for creep of lead-free solders undergoing strain-enhanced microstructural coarsening: A first report,“ *Journal of Electronic Materials*, Vol. 32, pp. 201-207, Jan. 2003.
- [66] S. K. Kang, P. Lauro, D. Y. Shih, D. W. Henderson and K. J. Puttlitz, „Microstructure and mechanical properties of lead-free solders and solder joints used in microelectronic applications,“ *IBM Journal of Research and Development*, Vol. 49, pp. 607-620, Jul. 2005.
- [67] R. Teimouri, S. Amini and M. Guagliano, „Analytical modeling ultrasonic burnishing process: Evaluation of residual stress field distribution and strip deflection,“ *Materials Science and Engineering: A*, Vol. 747, pp. 208-224, Feb. 2019.
- [68] J. Rudolph, T. Gilman, B. Weitze, A. Willuweit and A. Kalnins, „Using Nonlinear Kinematic Hardening Material Models for Elastic-Plastic Ratcheting Analysis,“ Vol. 138, Oct. 2016.

- [69] C. O. Frederick and P. J. Armstrong, „A mathematical representation of the multiaxial Bauschinger effect,“ *Materials at High Temperatures*, Vol. 24, pp. 1-26, Jan. 2007.
- [70] J. L. Chaboche, „Constitutive equations for cyclic plasticity and cyclic viscoplasticity,“ *International Journal of Plasticity*, Vol. 5, pp. 247-302, Jan. 1989.
- [71] J. L. Chaboche, „Time-independent constitutive theories for cyclic plasticity,“ *International Journal of Plasticity*, Vol. 2, pp. 149-188, Jan. 1986.
- [72] A. K. Asraff, S. Sheela, A. Paul, A. Mathew and S. Savithri, „Cyclic Stress Analysis of a Rocket Engine Thrust Chamber Using Chaboche, Voce and Creep Constitutive Models,“ *Transactions of the Indian Institute of Metals*, Vol. 69, pp. 495-500, Mar. 2016.
- [73] M. Laurent, R. Estevez, D. Fabrègue and E. Ajax, „Thermomechanical fatigue life prediction of 316L compact heat exchanger,“ *Engineering Failure Analysis*, Vol. 68, pp. 138-149, Oct. 2016.
- [74] A. Kabakchiev, B. Métais, R. Ratchev, M. Guyenot, P. Buhl, M. Hossfeld, X. Schuler, R. Metasch and M. Roellig, „Description of the thermo-mechanical properties of a Sn-based solder alloy by a unified viscoplastic material model for Finite Element calculations,“ in *Proceedings 15th International Conference on Thermal, Mechanical and Mult-Physics Simulation and Experiments in Microelectronics and Microsystems (EuroSimE)*, 2014.
- [75] R. Metasch, M. Roellig, A. Kabakchiev, B. Metais, R. Ratchev, K. Meier and K. .. Wolter, „Experimental investigation of the visco-plastic mechanical properties of a Sn-based solder alloy for material modelling in Finite Element calculations of automotive electronics,“ in *Proceedings 15th EuroSimE*, 2014.
- [76] B. Métais, A. Kabakchiev, Y. Maniar, M. Guyenot, R. Metasch, M. Roellig, P. Rettenmeier, P. Buhl and S. Weihe, „A viscoplastic-fatigue-creep damage model for tin-based solder alloy,“ in *Proceedings 16th EuroSimE*, 2015.
- [77] R. Metasch, R. Schwerz, M. Roellig, A. Kabakchiev, B. Metais, R. Ratchev and K. .. Wolter, „Experimental investigation on microstructural influence towards visco-plastic mechanical properties of Sn-based solder alloy for material modelling in finite element simulations,“ in *Proceedings 16th EuroSimE*, 2015.
- [78] M. Amagai, M. Watanabe, M. Omiya, K. Kishimoto and T. Shibuya, „Mechanical characterization of Sn-Ag-based lead-free solders,“ *Microelectronics Reliability*, Vol. 42, pp. 951-966, Jun. 2002.
- [79] M. Webmeister, „Phase Diagrams & Computational Thermodynamics,“ 2019. [Online]. Available: <https://www.metallurgy.nist.gov/phase/solder/solder.html>. [accessed 2021].
- [80] H. Tsukamoto, Z. Dong, H. Huang, T. Nishimura and K. Nogita, „Nanoindentation characterization of intermetallic compounds formed between Sn-Cu (-Ni) ball grid arrays and Cu substrates,“ *Materials Science and Engineering: B*, Vol. 164, pp. 44-50, Aug. 2009.
- [81] J. Gong, C. Liu, P. P. Conway and V. V. Silberschmidt, „Evolution of CuSn intermetallics between molten SnAgCu solder and Cu substrate,“ *Acta Materialia*, Vol. 56, pp. 4291-4297, Sep. 2008.
- [82] P. Yao, P. Liu and J. Liu, „Effects of multiple reflows on intermetallic morphology and shear strength of SnAgCu-xNi composite solder joints on electrolytic Ni/Au metallized substrate,“ *Journal of Alloys and Compounds*, Vol. 462, pp. 73-79, Aug. 2008.

- [83] B. I. Noh, J. M. Koo, J. W. Kim, D. G. Kim, J. D. Nam, J. Joo and S. B. Jung, „Effects of number of reflows on the mechanical and electrical properties of BGA package,“ *Intermetallics*, Vol. 14, pp. 1375-1378, Oct. 2006.
- [84] J.-W. Yoon, Y.-H. Lee, D.-G. Kim, H.-B. Kang, S.-J. Suh, C.-W. Yang, C.-B. Lee, J.-M. Jung, C.-S. Yoo and S.-B. Jung, „Intermetallic compound layer growth at the interface between Sn-Cu-Ni solder and Cu substrate,“ *Journal of Alloys and Compounds*, Vol. 381, pp. 151-157, Nov. 2004.
- [85] J. H. L. Pang, L. Xu, X. Q. Shi, W. Zhou and S. L. Ngoh, „Intermetallic growth studies on Sn-Ag-Cu lead-free solder joints,“ *Journal of Electronic Materials*, Vol. 33, pp. 1219-1226, Oct. 2004.
- [86] J.-B. Libot, J. Alexis, O. Dalverny, L. Arnaud, P. Milesi and F. Dulondel, „Microstructural evolutions of Sn-3.0Ag-0.5Cu solder joints during thermal cycling,“ *Microelectronics Reliability*, Vol. 83, pp. 64-76, Apr. 2018.
- [87] U. Sahaym, B. Talebanpour, S. Seekins, I. Dutta, P. Kumar and P. Borgesen, „Recrystallization and Ag₃ Sn Particle Redistribution During Thermomechanical Treatment of Bulk Sn-Ag-Cu Solder Alloys,“ *IEEE Transactions on Components, Packaging and Manufacturing Technology*, Vol. 3, pp. 1868-1875, Nov. 2013.
- [88] H. Chen, J. Han, J. Li and M. Li, „Inhomogeneous deformation and microstructure evolution of Sn-Ag-based solder interconnects during thermal cycling and shear testing,“ *Microelectronics Reliability*, Vol. 52, pp. 1112-1120, Jun. 2012.
- [89] X. Xu, G. Chen and M. Cheng, „Study on local recrystallization and damage mode of Lead-free BGA solder joint,“ in *Proceedings 15th International Conference on Electronic Packaging Technology (ICEPT)*, pp. 356-359, 2014.
- [90] T. R. Bieler, B. Zhou, L. Blair, A. Zamiri, P. Darbandi, F. Pourboghra, T.-K. Lee and K.-C. Liu, „The Role of Elastic and Plastic Anisotropy of Sn on Recrystallization and Damage Evolution During Thermal Cycling in SAC305 Solder Joints,“ *Journal of Electronic Materials*, Vol. 41, pp. 283-301, Feb. 2012.
- [91] K. N. Subramanian, „Role of anisotropic behaviour of Sn on thermomechanical fatigue and fracture of Sn-based solder joints under thermal excursions,“ *Fatigue & Fracture of Engineering Materials & Structures*, Vol. 30, pp. 420-431, Nov. 2006.
- [92] T. R. Bieler, B. Zhou, L. Blair, A. Zamiri, P. Darbandi, F. Pourboghra, T. Lee and K. Liu, „The role of elastic and plastic anisotropy of Sn on microstructure and damage evolution in lead-free solder joints,“ in *Proceedings International Reliability Physics Symposium*, 2011.
- [93] G. A. Rinne, „Electromigration in SnPb and Pb-free solder bumps,“ in *Proceedings. 54th ECTC*, pp. 974-978, 2004.
- [94] M. Tamaro, „Investigation of the temperature dependence in Black's equation using microscopic electromigration modeling,“ *Journal of Applied Physics*, Vol. 86, Sep. 1999.
- [95] Y.-W. Chang, S. W. Liang and C. Chen, „Study of void formation due to electromigration in flip-chip solder joints using Kelvin bump probes,“ *Applied Physics Letters*, Vol. 89, pp. 32103-32103, Jul. 2006.

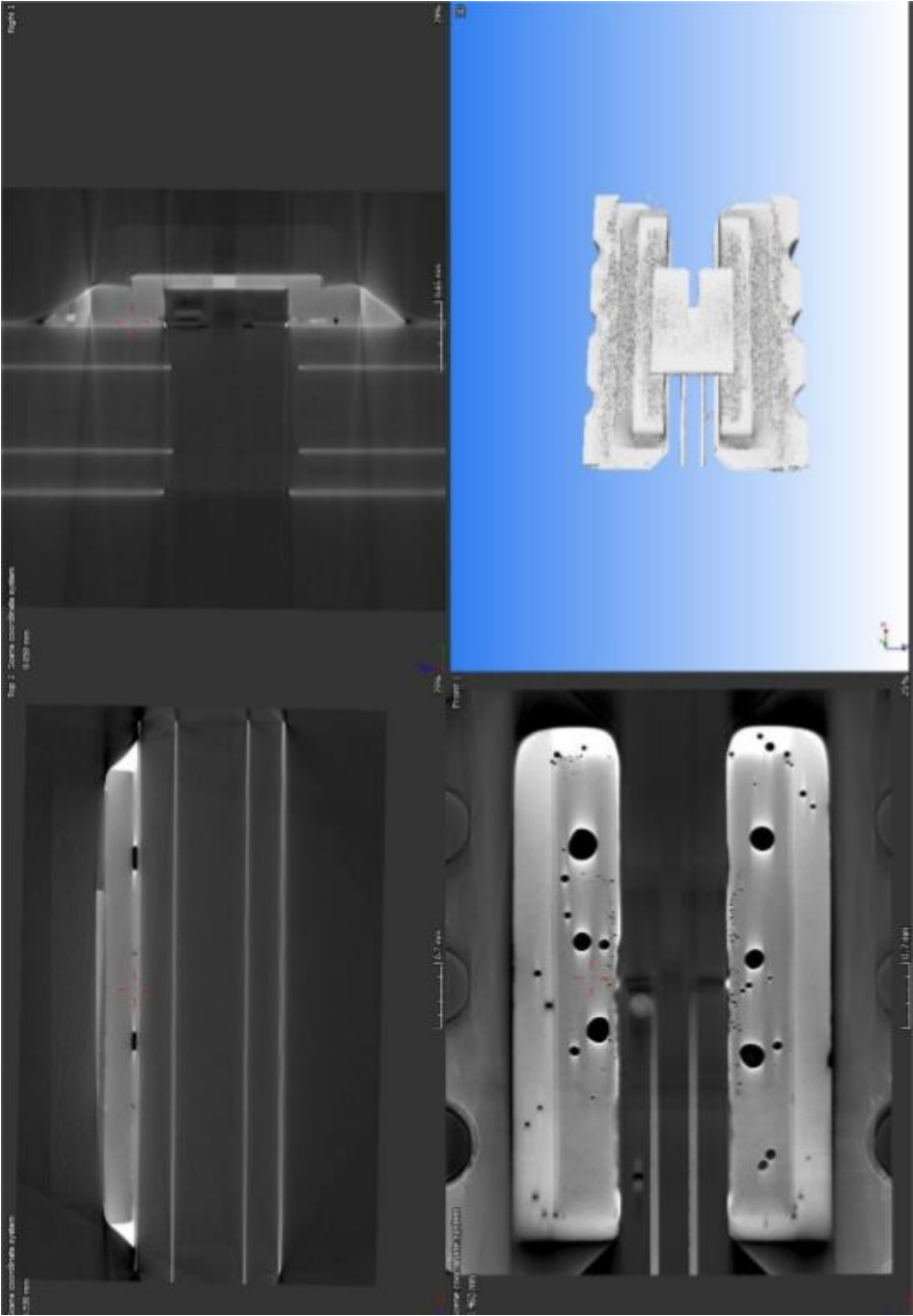
- [96] L. Zhang, S. Ou, J. Huang, K. N. Tu, S. Gee and L. Nguyen, „Effect of current crowding on void propagation at the interface between intermetallic compound and solder in flip chip solder joints,“ *Applied Physics Letters*, Vol. 88, pp. 12106-12106, Feb. 2006.
- [97] W. J. Choi, E. C. C. Yeh and K. N. Tu, „Mean-time-to-failure study of flip chip solder joints on Cu/Ni(V)/Al thin-film under-bump-metallization,“ *Journal of Applied Physics*, Vol. 94, pp. 5665-5671, May 2020.
- [98] W. J. Choi, E. C. C. Yeh, K. N. Tu, P. Elenius and H. Balkan, „Electromigration of flip chip solder bump on Cu/Ni(V)/Al thin film under bump metallization,“ in *Proceedings 52nd ECTC*, 2002.
- [99] M. Lu, D.-Y. Shih, P. Lauro, C. Goldsmith and D. W. Henderson, „Effect of Sn grain orientation on electromigration degradation mechanism in high Sn-based Pb-free solders,“ *Appl. Phys. Lett.*, Vol. 92, pp. 211909, Apr. 2020.
- [100] Y.-W. Chang, Y. Cheng, F. Xu, L. Helfen, T. Tian, M. Di Michiel, C. Chen, K.-N. Tu and T. Baumbach, „Study of electromigration-induced formation of discrete voids in flip-chip solder joints by in-situ 3D laminography observation and finite-element modeling,“ *Acta Materialia*, Vol. 117, pp. 100-110, Sep. 2016.
- [101] Y.-W. Chang, Y. Cheng, L. Helfen, F. Xu, T. Tian, M. Scheel, M. Di Michiel, C. Chen, K.-N. Tu and T. Baumbach, „Electromigration Mechanism of Failure in Flip-Chip Solder Joints Based on Discrete Void Formation,“ *Scientific Reports*, Vol. 7, pp. 17950, Dec. 2017.
- [102] D. Dalleau and K. Weide-Zaage, „3-D time-depending electro- and thermomigration simulation of metallization structures,“ in *Proceedings Advanced Metallization Conference (AMC)*, 2000.
- [103] D. Dalleau and K. Weide-Zaage, „Three-Dimensional Voids Simulation in chip Metallization Structures: a Contribution to Reliability Evaluation,“ *Microelectronics Reliability*, Vol. 41, pp. 1625-1630, Sep. 2001.
- [104] H. Gan and K. N. Tu, „Polarity effect of electromigration on kinetics of intermetallic compound formation in Pb-free solder V-groove samples,“ *Journal of Applied Physics*, Vol. 97, pp. 63514-63514, Mar. 2005.
- [105] S.-H. Chae, X. Zhang, K.-H. Lu, H.-L. Chao, P. S. Ho, M. Ding, P. Su, T. Uehling, L. N. Ramanathan and K. N. Subramanian, „Electromigration statistics and damage evolution for Pb-free solder joints with Cu and Ni UBM in plastic flip-chip packages,“ *Journal of Materials Science: Materials in Electronics*, Vol. 18, pp. 247-258, Mar. 2007.
- [106] L. D. Chen, M. L. Huang and S. M. Zhou, „Effect of electromigration on intermetallic compound formation in line-type Cu/Sn/Cu interconnect,“ *Journal of Alloys and Compounds*, Vol. 504, pp. 535-541, Aug. 2010.
- [107] C. Y. Liu, L. Ke, Y. C. Chuang and S. J. Wang, „Study of electromigration-induced Cu consumption in the flip-chip Sn/Cu solder bumps,“ *Journal of Applied Physics*, Vol. 100, pp. 83702-83702, Oct. 2006.
- [108] S.-K. Seo, S. K. Kang, M. G. Cho, D.-Y. Shih and H. M. Lee, „The Crystal Orientation of β -Sn Grains in Sn-Ag and Sn-Cu Solders Affected by Their Interfacial Reactions with Cu and Ni(P) Under Bump Metallurgy,“ *Journal of Electronic Materials*, Vol. 38, pp. 2461, Aug. 2009.

- [109] H. Sun and M. Huang, „Dominant effect of Sn grain orientation on electromigration-induced failure mechanism of Sn-3.0Ag-0.5Cu flip chip solder interconnects,“ in *Proceedings 18th ICEPT*, 2017.
- [110] J.-Q. Chen, J.-D. Guo, K.-L. Liu and J.-K. Shang, „Dependence of electromigration damage on Sn grain orientation in Sn-Ag-Cu solder joints,“ *Journal of Applied Physics*, Vol. 114, pp. 153509, Apr. 2020.
- [111] W. W. Lee, L. T. Nguyen and G. S. Selvaduray, „Solder joint fatigue models: review and applicability to chip scale packages,“ *Microelectronics Reliability*, Vol. 40, pp. 231-244, Feb. 2000.
- [112] J. R. Black, „Electromigration--A brief survey and some recent results,“ *IEEE Transactions on Electron Devices*, Vol. 16, pp. 338-347, Apr. 1969.
- [113] S. Brandenvurg and S. Yeh, „Electromigration Studies of Flip Chip Bump Solder Joints,“ in *Proceedings Surface Mount International Conference & Exhibition*, 1998.
- [114] J. Huang, S. Gee, L. Nguyen and K.-n. Tu, „The Effect of Electromigration on Eutectic SnPb and Pb-free Solders in Wafer Level-Chip Scale Packages,“ 2005.
- [115] Y. Bulur, R. J. Fishbune, M. Vaughn, J. Fitzpatrick and E. D. Blackshear, „Electromigration study on the interconnects of high density power modules,“ in *Proceedings 27th Annual IEEE Applied Power Electronics Conference and Exposition (APEC)*, pp. 2290-2297, 2012.
- [116] L. Nicholls, R. Darveaux, A. Syed, S. Z. Y. Loo, T. Y. Tee, T. A. Wassick and B. K. Batchelor, „Comparative electromigration performance of Pb Free flip chip joints with varying board surface condition,“ in *Proceedings 59th ECTC*, pp. 914-921, 2009.
- [117] M. Ding, G. Wang, B. Chao, P. S. Ho, P. Su, T. Uehling and D. Wontor, „A study of electromigration failure in Pb-free solder joints,“ in *Proceedings 43rd IEEE International Reliability Physics Symposium*, 2005.
- [118] R. Labie, T. Webers, C. Winters, V. Cherman, K. Croes, B. Vandeveldel and F. Dosseul, „Electromigration failure mechanisms for different flip chip bump configurations,“ in *Proceedings International Reliability Physics Symposium*, 2011.
- [119] J. Lee, Y. Lee, Y. Park, S. Yang, M. Suh, Q. Chung and K. Byun, „Joule Heating Effect on the Electromigration Lifetimes and Failure Mechanisms of Sn-3.5Ag Solder Bump,“ in *Proceedings 57th ECTC*, pp. 1436-1441, 2007.
- [120] K. Son, H. Ryu, G. Kim, J. Lee and Y. Park, „Electromigration polarity effect of Cu/Ni/Sn-Ag microbumps for three-dimensional integrated circuits,“ in *19th Electronics Packaging Technology Conference (EPTC)*, pp. 1-3, 2017.
- [121] G. U. Chukwu, „Thermoelectric study of Peltier effect using Cu-Fe, Pb-Fe and Cu-Constantan couples,“ *International Journal of Innovative Scientific & Engineering Technologies Research*, Vol. 4, pp. 1-12, Oct. 2016.
- [122] P. Wild, T. Grözinger, D. Lorenz and A. Zimmermann, „Void Formation and Their Effect on Reliability of Lead-Free Solder Joints on MID and PCB Substrates,“ *IEEE Transactions on Reliability*, Vol. 66, pp. 1229-1237, Dec. 2017.
- [123] Y. Zhang, „Electromigration Failure Prediction and Reliability Evaluation of Solder Bumps for FCBGA package,“ *Engineering Transactions*, Vol. 63, pp. 215-232, 2015.

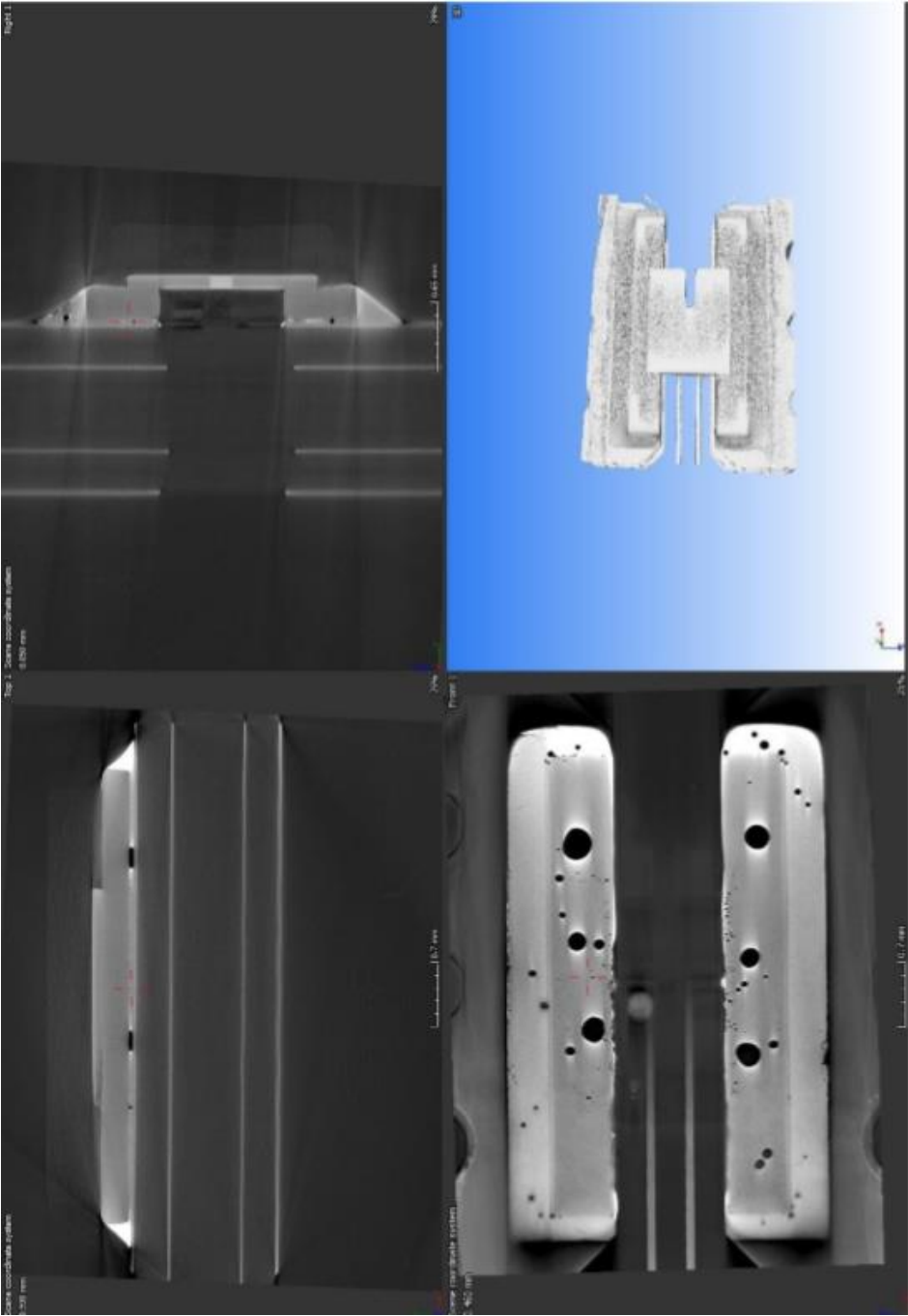
- [124] J. Mei, R. Haug, S. Hinderberger, T. Grözinger and A. Zimmermann, „Void formation in solder joints under power cycling conditions and its effect on reliability,“ *Microelectronics Reliability*, Vol. 100-101, pp. 113350, Sep. 2019.
- [125] Z. W. Fu, B. Zhou, R. H. Yao, Y. R. Liu and X. P. Li, „Electromigration Effect on Kinetics of Cu-Sn Intermetallic Compound Growth in Lead-Free Solder Joint,“ *IEEE Transactions on Device and Materials Reliability*, Vol. 17, pp. 773-779, Dec. 2017.
- [126] M. Huicai, J. Guo, J. Chen, D. Wu, Z.-Q. Liu, Z. J. Shang, L. Zhang and H.-Y. Guo, „Reliability and failure mechanism of copper pillar joints under current stressing,“ *Journal of Materials Science: Materials in Electronics*, Vol. 26, pp. 7690-7697, Jul. 2015.
- [127] C. J. M. Lasance, „The Seebeck Coefficient,“ 2006. [Online]. Available: <https://www.electronics-cooling.com/>. [accessed 2021].
- [128] P. S. Ho and T. Kwok, „Electromigration in metals,“ *Reports on Progress in Physics*, Vol. 52, pp. 301-348, Mar. 1989.
- [129] B. Chao, S.-H. Chae, X. Zhang, K.-H. Lu, J. Im and P. S. Ho, „Investigation of diffusion and electromigration parameters for Cu-Sn intermetallic compounds in Pb-free solders using simulated annealing,“ *Acta Materialia*, Vol. 55, pp. 2805-2814, May 2007.
- [130] B. H.-L. Chao, X. Zhang, S.-H. Chae and P. S. Ho, „Recent advances on kinetic analysis of electromigration enhanced intermetallic growth and damage formation in Pb-free solder joints,“ *Microelectronics Reliability*, Vol. 49, pp. 253-263, Mar. 2009.
- [131] B. Chao, S.-H. Chae, X. Zhang, K.-H. Lu, M. Ding, J. Im and P. S. Ho, „Electromigration enhanced intermetallic growth and void formation in Pb-free solder joints,“ *Journal of Applied Physics*, Vol. 100, pp. 084909, Apr. 2006.

Appendix

CT-scan of shunt A (3mΩ) after reflow



CT-scan of shunt A (3mΩ) after 10000 PCs



CT-scan of shunt A (3mΩ) after 20000 PCs

